

BURNER STABILITIES
OF JET DIFFUSION FLAMES

by
James Phillip Seaba

An Abstract

Of a thesis submitted in partial fulfillment of the requirements
for the Doctor of Philosophy degree in Mechanical Engineering
in the Graduate College of The University of Iowa

December 1990

Thesis supervisor: Associate Professor Lea-Der Chen

19981202 035

[DTIC QUALITY INSPECTED 5]

REPORT DOCUMENTATION PAGE

AFRL-SR-BL-TR-98-

Public reporting burden for this collection of information is estimated to average 1 hour per response, including the time for reviewing the data needed, and completing and reviewing the collection of information. Send comments regarding this burden estimate or any other aspect of this collection of information, including suggestions for reducing this burden, to Washington Headquarters Services, Directorate for Information Operations and Reports, 1204, Arlington, VA 22202-4302, and to the Office of Management and Budget, Paperwork Reduction Project (0704-0188), Washington, DC 20503.

0742
thoring
tion of
, Suite

1. AGENCY USE ONLY (Leave Blank)	2. REPORT DATE December, 1990	3. REPORT TYPE AND DATES COVERED Final	
4. TITLE AND SUBTITLE Burner Stabilities of Jet Diffusion Flames		5. FUNDING NUMBERS	
6. AUTHORS James Phillip Seaba		5. FUNDING NUMBERS	
7. PERFORMING ORGANIZATION NAME(S) AND ADDRESS(ES) University of Iowa		8. PERFORMING ORGANIZATION REPORT NUMBER	
9. SPONSORING/MONITORING AGENCY NAME(S) AND ADDRESS(ES) AFOSR/NI 4040 Fairfax Dr, Suite 500 Arlington, VA 22203-1613		10. SPONSORING/MONITORING AGENCY REPORT NUMBER	
11. SUPPLEMENTARY NOTES			
12a. DISTRIBUTION AVAILABILITY STATEMENT Approved for Public Release		12b. DISTRIBUTION CODE	
13. ABSTRACT (Maximum 200 words) See Attachment			
14. SUBJECT TERMS		15. NUMBER OF PAGES	
		16. PRICE CODE	
17. SECURITY CLASSIFICATION OF REPORT Unclassified	18. SECURITY CLASSIFICATION OF THIS PAGE Unclassified	19. SECURITY CLASSIFICATION OF ABSTRACT Unclassified	20. LIMITATION OF ABSTRACT UL

**BURNER STABILITIES
OF JET DIFFUSION FLAMES**

by

James Phillip Seaba

An Abstract

Of a thesis submitted in partial fulfillment of the requirements
for the Doctor of Philosophy degree in Mechanical Engineering
in the Graduate College of The University of Iowa

December 1990

Thesis supervisor: Associate Professor Lea-Der Chen

ABSTRACT

The near field lift-off phenomena associated with jet diffusion flames were investigated. Lift-off is defined as the instant when the luminous flame zone detaches from the burner exit, stabilizing itself downstream. The lift-off of the jet diffusion flames were studied using a fuel jet centered in a large coflowing air annulus. Fuels used consisted of methane and propane. The fuels are diluted with nitrogen, argon, and helium. Annulus, diluted fuel, and external nozzle geometry effects are studied for the jet diffusion flame. The jet diffusion flame is sensitive to the annulus velocity, the lift-off velocity decreasing with increasing annular velocity. Lift-off velocity decreases as dilution concentrations of the fuel jet increase. The external geometry effects influence the lift-off velocity, especially at higher annular flow rates.

Two theories have explained the lift-off of jet diffusion flames. The locally premixed theory which assumes that the fuel and oxidant are fully premixed prior to combustion. The lift-off of the flame zone occurs due to the convective velocity of the premixed reactants exceeding the local flame speed. The second theory, the laminar flamelet model, states that the diffusion of reactants into the flame zone exceeds the chemical reaction rate, causing the flame to extinguish at the flame base, lifting the flame from the nozzle to a position downstream. The two models were evaluated by the different lift-off velocities produced by annulus and diluent effects.

Laser Doppler anemometry (LDA) was used to characterize the flow field at and near the base of the jet diffusion flame. The local straining rate across the flame was approximated by the gradient of the mean radial velocity in the radial direction for the pure

and diluted methane conditions. The straining rate was in qualitative agreement with that reported in the literature for counter-flow methane diffusion flames near extinction. The mean axial velocity measurements taken underneath the flame zone related to the flame speed within the context of the premixed flame theory showed little correlation with the lift-off of the methane jet diffusion flame. The present study shows that quenching of local flamelets due to high straining rates is an important mechanism responsible for the lift-off of methane jet diffusion flames.

Abstract approved:

Lea Dutcher

Thesis supervisor

Associate Professor, Mech Eng.

Title and department

September 10, 1990

Date

**BURNER STABILITIES
OF JET DIFFUSION FLAMES**

by
James Phillip Seaba

A thesis submitted in partial fulfillment of the requirements
for the Doctor of Philosophy degree in Mechanical Engineering
in the Graduate College of The University of Iowa

December 1990

Thesis supervisor: Associate Professor Lea-Der Chen

Graduate College
The University of Iowa
Iowa City, Iowa

CERTIFICATE OF APPROVAL

PH.D. THESIS

This is to certify that the Ph.D. thesis of
James Phillip Seaba

has been approved by the Examining Committee
for the thesis requirement for the Doctor of
Philosophy degree in Mechanical Engineering at
the December 1990 graduation.

Thesis committee: Lea Du Chen
Thesis supervisor
Theodore F. Smith
Member
P. Barry Butler
Member
W. M. Rogueme
Member
J. C. Lutz
Member
Cliff C. Tandy
Member

ACKNOWLEDGEMENTS

The author would like to express his appreciation to his advisor, Professor L.-D. Chen for his support and guidance throughout the course of my research efforts.

The comments by the committee members, Professors P.B. Butler, V.C. Patel, T.F. Smith, and D.C. Tardy and Dr. W.M. Roquemore were appreciated.

I wish to thank the Air Force Systems Command and the Air Force Office of Scientific Research doctoral fellowship program for sponsorship of this research through Universal Energy Systems, through Contract No. F49620-86-C-0127/SB5861-0436. Appreciation is extended to the Air Force Aero Propulsion and Power Laboratory at Wright Research and Development Center for use of their facilities and financial support for equipment through National Science Foundation Grant CTS-8922003. Dr. W.M. Roquemore provided helpful insights in the physics of the experiment, special thanks are extended to Dr. L.P. Goss, B. Sarka, and D.D. Trump, of System Research Laboratories for their technical assistance. The assistance of C. Obringer and J. Jaeger is also acknowledged.

I wish to thank my wife, Nancy, for her love and support as well as my entire family, namely my parents, Jim and Mary Jo. The Mechanical Engineering Department was inspirational and the help of Connie Lange and Nancy Yutzy is deeply appreciated.

TABLE OF CONTENTS

	Page
LIST OF FIGURES	vi
LIST OF TABLES	viii
NOMENCLATURE	ix
 CHAPTER	
I. INTRODUCTION	1
1.1 General Statement of the Problem	1
1.2 Literature Survey	5
1.2.1 Definitions of Burner Stabilities of Jet Diffusion Flames ...	5
1.2.2 Effects on the Lift-off Process	5
1.2.2.1 Initial Conditions	9
1.2.2.1.1 Geometry Effects	9
1.2.2.1.2 Thermochemical Effects	11
1.2.2.1.3 Fluid Mechanical Effects	12
1.2.2.2 Boundary Conditions	12
1.2.2.2.1 Geometry Effects	12
1.2.2.2.2 Thermochemical Effects	13
1.2.2.2.3 Fluid Mechanical Effects	13
1.3 Objectives of the Study	14
II. EXPERIMENTAL SETUPS AND PROCEDURES	15
2.1 Introduction.....	15
2.2 Experimental Facilities	15
2.2.1 WRDC Facilities	15
2.2.2 UI	19
2.3 Instrumentation	23

2.3.1	WRDC Instrumentation	23
2.3.2	UI Instrumentation	24
2.4	Experimental Conditions.....	26
2.5	Experimental Methods	28
2.5.1	WRDC	28
2.5.2	UI	32
III.	THEORETICAL CONSIDERATIONS	36
3.1	Introduction	36
3.2	Existing Theories	36
3.2.1	Premixed Flame Model	36
3.2.2	Laminar Flamelet Model	38
IV.	DISCUSSION AND RESULTS	41
4.1	Stability Curves	41
4.2	Location of the Flame Zone	49
4.3	LDA Measurements	53
4.3.1	LDA Experimental Conditions	53
4.3.2	Jet and Annulus Conditions	54
4.3.2.1	Cold Flow	54
4.3.2.2	Attached and Lifted Methane Jet Diffusion Flames	59
4.3.3	WRDC and UI Comparison	62
4.3.4	Annular Effects	65
4.3.5	Diluent Effects	75
V.	SUMMARY AND CONCLUSIONS	84
	REFERENCES	87
APPENDIX A	MEASURING VOLUMES	91
APPENDIX B	EQUIPMENT LIST FOR LDA AT WRDC.....	93
APPENDIX C	AVERAGED TIME QUANTITY DERIVATIONS.....	95
APPENDIX D	CALCULATIONS FOR THREE POSITION ORIENTATION VELOCITY MEASUREMENTS	98

APPENDIX E	ERROR ANALYSIS	107
APPENDIX F	LDA DATA	113
APPENDIX G	STABILITY CURVE DATA	130

LIST OF FIGURES

	Page
Fig. 1.1 Location of Flame Base Relative to Exit Velocity	2
Fig. 1.2 Typical Geometry Configurations	10
Fig. 2.1 WRDC Experimental Setup	16
Fig. 2.2 Nozzle Geometries	18
Fig. 2.3 UI Experimental Setup	20
Fig. 2.4 Schematic of the Combustor Design at The University of Iowa	21
Fig. 2.5 WRDC LDA System	25
Fig. 2.6 UI LDA and Data Acquisition System	27
Fig. 2.7 Vector Orientation	30
Fig. 2.8 Rotating Disk for LDA Calibration	34
Fig. 3.1 Diffusion Flame Premixed Schematic	37
Fig. 3.2 Counter-Flow and Jet Diffusion Flames	40
Fig. 4.1 Annulus Effects on Lift-off of Jet Diffusion Flames Using Tapered Nozzle.	42
Fig. 4.2 Annulus Effects	44
Fig. 4.3 Fuel and External Geometry Effects	45
Fig. 4.4 Diluent Effects	47
Fig. 4.5 Flame Zone	50
Fig. 4.6 LDA Test Conditions	53
Fig. 4.7 Mean Axial Velocity Distribution in an Argon Jet at $x/d = 0.4$	55
Fig. 4.8 Mean Radial Velocity Distribution in an Argon Jet at $x/d = 0.4$	56

Fig. 4.9	Turbulence Intensity Profiles in an Argon Jet at $x/d = 0.4$	57
Fig. 4.10	Radial Profile in an Argon Jet at Two Axial Locations	58
Fig. 4.11	Axial Profile in Lifted and Attached Methane Jet Diffusion Flames at $x/d = 0.4$	60
Fig. 4.12	Radial Velocity Profile in Attached and Lifted Methane Jet Diffusion Flames at $x/d = 0.4$	61
Fig. 4.13	RMS Profile in Lifted and Attached Methane Jet Diffusion Flames at $x/d = 0.4$	63
Fig. 4.14	Turbulence Intensity Profile in Attached and Lifted Methane Jet Diffusion Flames at $x/d = 0.4$	64
Fig. 4.15	Mean Axial Velocity Profile in WRDC and UI Attached Methane Jet Diffusion Flames	66
Fig. 4.16	Mean Radial Velocity Profile in WRDC and UI Attached Methane Jet Diffusion Flames	67
Fig. 4.17	Axial Velocity Fluctuation Profile in WRDC and UI Attached Methane Jet Diffusion Flames	68
Fig. 4.18	Radial Velocity Fluctuation Profile in WRDC and UI Attached Methane Jet Diffusion Flames	69
Fig. 4.19	Mean Velocity Profiles of Annular Conditions	71
Fig. 4.20	Radial Velocity Profiles of Annular Conditions	73
Fig. 4.21	Mean Velocity Profiles in Methane/Argon Jet Diffusion Flames	76
Fig. 4.22	Velocity Fluctuation Profiles in Methane/Argon Jet Diffusion Flames	77
Fig. 4.23	Mean Velocity Profiles in Methane/Helium Jet Diffusion Flames	78
Fig. 4.24	Velocity Fluctuation Profiles in Methane/Helium Jet Diffusion Flames	79
Fig. 4.25	Straining Rates in Diluted Methane Jet Diffusion Flames	81
Fig. 4.26	Comparison of Extinction Straining Rate for Methane Counter-Flow Diffusion Flames with Lift-Off Straining Rate for Methane Jet Diffusion Flames (I&T, 1981, Denotes Ishizuka and Tsuji, 1981)	83

LIST OF TABLES

	Page
Table 1.1 Summary of Jet Diffusion Flame Experiments	6
Table 2.1 Diffusion Flame Test Conditions	28
Table 4.1 Flame Location of Methane and Methane Diluted Jet Diffusion Flames	51
Table 4.2 Diluent Conditions for LDA Measurements	51
Table 4.3 Straining Rates at Annular Conditions A, B, and C	74
Table 4.4 Straining Rates at Diluted Conditions	82

NOMENCLATURE

A	pre-exponential sector in Arrhenius expression
C	concentration
d	diameter
d_e^{-2}	waist diameter of the laser beam
d_f	fringe spacing
d_j	diameter of jet
d_m	minor axis of the measuring volume
d_o	diameter of annulus
D	molecular diffusivity
E	activation energy
f_m	measured frequency
f_s	frequency shift
I	turbulence intensity
l_m	major axis of measuring volume
M	number of species
N	number of samples
N_b	number of cycles per burst
N_f	number of fringes in the control volume
R	inner radius of burner exit
r	radial distance from centerline of burner exit
R_u	universal gas constant

S_u	laminar flame speed
t	time
T	local temperature
U	axial velocity measurement
\bar{U}	mean axial velocity
U_{rms}	root-mean-squared axial velocity
V	radial velocity measurement
\bar{V}	mean radial velocity
V_a	air velocity
V_f	fuel velocity
V_j	jet velocity
V_o	annulus velocity
V_{rms}	root-mean-squared radial velocity
x	axial distance from burner exit
Y	mass function
Z	mixture function

Symbols

θ	angle between measurement and axial, or radial coordinate
ξ	population mean velocity
η	coordinate normal to flame zone
σ	population standard deviation
ω	reaction rate
ρ	density
Δ	increment of quantity

χ	scalar dissipation
ν	stoichiometric coefficient
λ	wavelength

Subscripts

c	centerline value
i	specie
j	instantaneous quantity
m	mean value of sample
s	sample standard deviation

Superscripts

+	velocity measurement coordinate
-	velocity measurement coordinate

CHAPTER I

INTRODUCTION

1.1 General Statement of the Problem

The mechanism causing a jet diffusion flame to lift from a burner is partially responsible for the instabilities in jet engines. Other related problems of flame lifting include the blow-off of burning natural gas at oil refineries and storage facilities, and stabilization of fuel injectors in coal burning power plants. The processes and quantities that determine lift-off are not clearly understood.

There are two different types of jet flames, premixed and diffusion. Jet premixed flames are defined as the situation where the fuel and oxidizer are mixed intimately prior to the burner exit. Jet diffusion flames, however, require the fuel and oxidant to mix after the fuel exits the burner tube. This investigation will focus entirely on jet diffusion flames.

Lift-off is defined as the instant when the flame detaches from the nozzle in a discontinuous manner, positioning the flame downstream or to extinction (blow-off) as defined by Wohl et al. (1949). The lift-off process is shown in Fig. 1.1, where the height represents the distance between the base of the flame and the nozzle exit. The average jet velocity consists of fuel, or fuel and diluents. The lift-off velocity (V_{crit}) of the fuel jet is recorded at different conditions produced by changing the annular flow rate or introducing inerts into the fuel jet. The lift-off velocity (V_{crit}) is recorded by maintaining the annular velocity constant and increasing the jet velocity until V_{crit} is achieved. The curves produced from these effects are defined as stability curves.

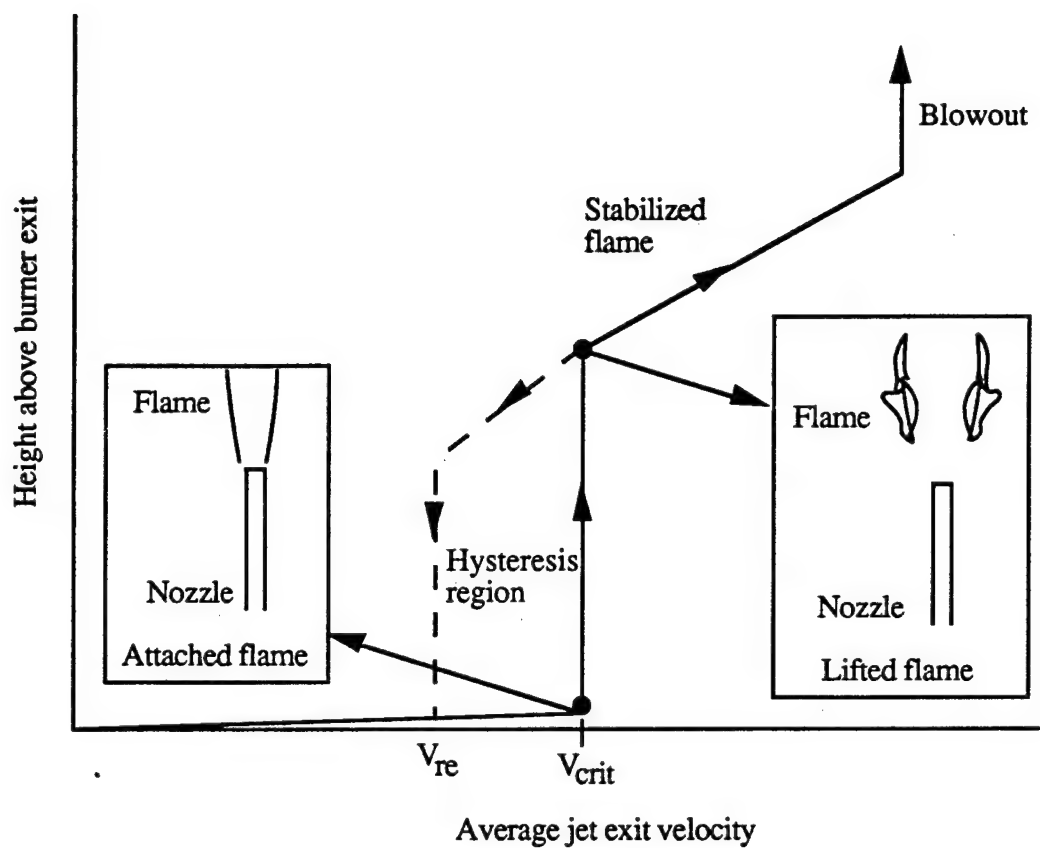


Figure 1.1 Location of Flame Base Relative to Exit Velocity

The attached flame regime near lift-off is where the exit velocity is slightly less than V_{crit} . The color of the luminous flame zone is blue at the flame base, the luminous flame surface is smooth and located slightly above the burner exit. The structure of the luminous flame is steady and axisymmetric in appearance. After lift-off and near V_{crit} , the luminous flame zone jumps downstream to an average axial location two diameters above the burner exit ($x/d = 2$). The appearance of the lifted flame is quite different than the attached flame. The luminous flame is blue but, unsteady with a turbulent-like flame surface. The flame base location oscillates up and down as the flame contorts. The appearance of the flame zone at the attached and lifted conditions near V_{crit} are illustrated in Fig. 1.1.

Once the flame is stabilized downstream after V_{crit} , increasing the jet velocity will increase the average flame base height above the burner exit. This will continue to increase with increasing fuel jet velocity until the flame extinguishes itself (approximately $x/d = 60$), defined as blowout.

After lift-off (V_{crit}) the fuel jet exit velocity may be decreased ($<V_{crit}$) which decreases the flame height as shown by the dashed line in Fig. 1.1. The flame will reattach to the burner lip (V_{re}) at a lower jet exit velocity than V_{crit} . The difference between the reattachment jet exit velocity and V_{crit} is defined as the hysteresis region of a jet diffusion flame.

Presently, there are two different theories which determine the velocity at which a jet diffusion flame will lift-off. The premixed flame model is the most straightforward, where the convective velocity of the reactant mixture at the flame base exceeds the chemical reaction rate or the local turbulent flame speed (Vanquickenborne and van Tiggelen, 1966). The turbulent flame speed is a function of the laminar flame speed and local turbulence quantities (for example, fluctuation in velocity or concentration). The laminar flame speed is defined as the velocity normal to the flame zone at ambient temperature. It is empirically

determined for a variety of fuels and fuel diluents which are fully premixed prior to combustion. The effects of local turbulence quantities at the flame have been investigated experimentally for premixed fuels. An increase in local turbulence quantities increases the flame speed relative to the laminar flame speed, the quantitative influence of the turbulence quantities on the flame speed in a free jet is not available.

The laminar flamelet model assumes that local extinction of the flame at the flame base is responsible for the lift-off of the flame from the nozzle exit (Peters and Williams, 1983). Extinction of the flame is due to the rate of diffusion of reactants into the flame zone exceeding the chemical reaction rate. As the rate of diffusion increases the local scalar dissipation increases and therefore the straining rate is increased (Gibson, 1968). The straining rate of jet diffusion flames is approximated by the mean radial velocity gradient in the radial direction (dV/dr) at the flame zone (Williams, 1975).

Annulus and diluents affect the lift-off velocity providing different conditions in which to characterize the velocity field near the jet exit using laser Doppler anemometry (LDA). Since the quantitative results at a single lift-off condition is not predictable by current theories, a comparison of different lift-off velocity conditions using different annular velocities and diluents can determine which of the current theories is most appropriate. The local convective velocity of the unburnt gas mixture and the straining rate across the flame zone are determined by LDA measurements at different dilutions and annular velocities at the flame base, near the lift-off condition. These results are compared to the theoretical straining rates near extinction and the local flame speeds of methane mixtures.

Since quantities such as scalar dissipation and turbulent flame speed are not clearly defined by easily measurable quantities, current lift-off theories are unproven. It is the purpose of this investigation to determine which, if any, of the theories pertain to the jet

diffusion flames studied. This information will provide an insight on the mechanisms causing the lift-off of jet diffusion flames.

This thesis consists of five chapters. Chapter I summarizes the literature survey. Experimental considerations are described in Chapter II, and Chapter III provides the current theoretical understanding. Chapter IV presents the results of measurements and comparison with current theories. Conclusion and recommendations for future work are summarized in Chapter V.

1.2 Literature Survey

1.2.1 Definitions of Burner Stabilities of Jet Diffusion Flames

Lift-off is defined as the instant when the flame detaches from the nozzle in a discontinuous manner, positioning the flame downstream or to extinction (blow-off) as defined by Wohl et al. (1949), e.g. see Fig. 1.1. Once the flame is stabilized downstream, the distance between the flame and the burner exit is defined as the stabilization height. Increasing the jet velocity increases the stabilization height until the flame becomes extinct (blow-out). Decreasing the jet velocity decreases the stabilization height until the flame reattaches to the burner exit (reattachment).

1.2.2 Effects on the Lift-off Process

Diffusion flames have been studied extensively concerning lift-off, stabilization height, blowout, and reattachment. The conditions studied may be divided into initial conditions (burner exit) and boundary conditions (annulus or ambient). The initial and boundary conditions are divided into three groups, geometry, thermochemical, and

Table 1.1. Summary of Jet Diffusion Flame Experiments

<u>I. INITIAL CONDITIONS</u>		<u>L^a</u>	<u>SH^b</u>	<u>BO^c</u>	<u>R^d</u>
<u>Geometry</u>	<u>PRESENT STUDIES</u>				
<u>Diameter</u> (mm)	38 to 102 (ME)			Y	
	2 to 10 (DP)	Y	Y	Y	
	1.08 to 10.1 (K2)		Y		
	4 to 20 (ELL)	Y	Y	Y	Y
	0.2 to 12 (K1)			Y	
	0.55 to 16 (AS)	Y	Y	Y	Y
	5.53, 8.74, 12.36; contoured (GSHRA)	Y	Y		Y
	0.59 to 5.98, (TMI, TMIT, TSV)	Y			
	1.7, 4.2, 8.2 (VTS)	Y			
	2 to 80 (SH)		Y	Y	
<u>Lip thickness</u> (mm)	0.074 to 1.064; OD/ID=1 to 1.5 (VTS)	Y			
	OD/ID=1 to 10 (AS)	Y	Y	Y	Y
	0.2, 1.2, 2.4mm (TSV)	Y		Y	
<u>Thermochemical</u>					
<u>Fuel Type</u>	CH ₄ , C ₃ H ₈ , H ₂ , Butanes			Y	
	C ₂ H ₄ , C ₂ H ₂ (K1)				
	CH ₄ , C ₃ H ₈ , H ₂ , C ₂ H ₆ (K2)	Y			
	CH ₄ , C ₃ H ₈ , H ₂ , H ₂ +Nat'l Gas (AS)	Y	Y	Y	Y
	H ₂ (TK, VTS, TMIF, TMI)	Y			
	CH ₄ , C ₃ H ₈ (GSHRA)	Y			Y
	C ₃ H ₈ (SH, G)	Y	Y	Y	
	CH ₄ (SH, DP)	Y	Y	Y	
	H ₂ +N ₂ , Ar, He (TMIF, TMI)	Y			
	CH ₄ , C ₃ H ₈ + CO ₂ (K1)			Y	
<u>Fuel + Inert</u>	CH ₄ , C ₃ H ₈ +CO ₂ , N ₂ (KWH)			Y	
	CH ₄ , C ₃ H ₈ +CO ₂ , N ₂ (GSHRA)	Y			Y
	C ₃ H ₈ +CO ₂ , N ₂ (G)	Y	Y	Y	
	CH ₄ + N ₂ (DP, VT)	Y	Y	Y	
	Nat'l Gas (H, ELL)	Y	Y	Y	Y
	City Gas-H ₂ +N ₂ +CH ₄ +Others (TK)	Y			
	CH ₄ and C ₃ H ₈ (K1)			Y	
<u>Fuel + Air</u>					
<u>Temp. at exit (K)</u>	300-1000 (TK)	Y			

Table 1.1. (continued)

<u>PRESENT STUDIES</u>		<u>L^a</u>	<u>SH^b</u>	<u>BO^c</u>	<u>R^d</u>
<u>Fluid Mechanical</u>					
Velocity (m/s)	4 to 2000				
Velocity Profile	Tube vs Contoured (ZPC)	Y			Y
	Tube vs Contoured (ELL)	Y		Y	Y
	Tube vs Contoured (H)	Y	Y	Y	Y
	Different length tubes (SSG)	Y			Y
Turbulence Intensity					
Velocity Scale	(TMIF,TSV)	Y			
Length Scale	None				
<u>II. BOUNDARY CONDITIONS</u>					
<u>Geometry</u>					
Diameter (mm)	(TMIF)	Y			
<u>Thermochemical</u>					
O ₂ + Inert	O ₂ (20.9% v)+N ₂ ,Ar,He (TMIF,TMI)	Y			
	N ₂ (DP)	Y	Y	Y	
Air + Inert	CO ₂ ,N ₂ (G)	Y	Y	Y	
Air +Fuel	CH ₄ ,H ₂ ,C ₃ H ₈ ,C ₂ H ₄ (KWH)			Y	
Temp. at exit (K)	300 to 1000 (TK)	Y			
<u>Fluid Mechanic</u>					
Velocity (m/s)	0.37,0.58,0.80: 1 to 20% of jet (DD)	Y	Y	Y	Y
	5 to 50: 1 to 30% of jet (TK)	Y			
	5 to 280: 0.1 to 1000% of jet (VTS)	Y			
	0 to 7: 0 to 30% of jet (TSV)	Y			
Velocity Profile	(TMIF,TSV)				
Turbulence Intensity					
Velocity Scale	(TMIF,TSV)	Y			
Length Scale	None				

Table 1. (Continued)

<u>Initial(s)</u>	<u>Author(s)</u>
AS	Annushkin and Sverdlov (1979)
DD	Dahm and Dibble (1988)
DP	Donnerhack and Peters (1984)
ELL	Eickhoff, Lenze, and Leuckel (1984)
G	Gollahalli (1977)
GSHRA	Gollahalli, Savas, Huang, and Rodriques Azara (1986)
H	Horch (1978)
K1, K2	Kalghatgi (1981 (K1), 1984 (K2))
KWH	Karim, Wierzba, and Hanna (1984)
ME	McCaffrey and Evans (1986)
SH	Sonju and Hustad (1984)
SSG	Shekarchi, Savas, and Gollahalli (1988)
TK	Takeno and Kotani (1975)
TMI	Takahashi, Mizomoto, and Ikai (1980)
TMIF	Takahashi, Mizomoto, Ikai, and Futaki (1984)
TMIT	Takahashi, Mizomoto, Ikai, and Tsuruyama (1990a)
TSV	Takahashi, Schmoll, and Vangsness (1990b)
VT	Vanquickenborne and van Tiggelen (1965)
VTs	Vranos, Taback, and Shipman (1968)
ZPC	Zsak, Perlee, and Chigier (1984)

^aL = Lift-off^bSH = Stabilization Height^cBO = Blow-off^dR = Reattachment

fluid mechanical effects as summarized in Table 1.1. The acronyms in the parenthesis refer to the sources listed at the end of the Table. Y refers to yes, indicating that the phenomena was studied in that particular experiment. Details of the experiments concerning lift-off are presented in the initial and boundary conditions sections (1.2.2.1 and 1.2.2.2).

1.2.2.1 Initial Conditions

1.2.2.1.1 Geometry Effects

Geometry effects pertain to the influence of burner exit size (d_j) and thickness of the burner wall (t_j) at the exit. The geometry of the burner (tube and contoured) also influences the lift-off velocity. Figure 1.2 shows a typical tube and contoured burner tube (V_j) arrangement, both with annular velocities (V_o).

Vranos et al. (1968) studied hydrogen flames with annular air. The jet consisted of a tube centered in the annulus with exit diameters ranging from 1.8 mm to 8.2 mm. The annulus diameters were 27.6 mm and 48.8 mm at the exit. The burner lip thicknesses ranged between 0.07 mm to 1.06 mm. The purpose of this experiment was to document the effects on the stability process concerning blowout or blow-off. It was observed that the burner tube diameters had little effect on the lift-off (blow-off) velocity, at an average annular velocity of 8 m/s.

Annushkin and Sverdlov (1979) concluded that the lift-off velocity was a nonlinear function of the diameter for a contracted nozzle. The exit diameter of the study included nozzles ranging from 0.55 to 16 mm. Fuels tested were methane, propane, hydrogen, and municipal gas. The lift-off velocity increased with decreasing diameters for the nozzle diameters tested. The wall thickness of the nozzles was not constant for each diameter and varied an order of magnitude, from 0.5 mm to 5 mm. Since the wall thickness was not

constant, diameter effects on the lift-off process were not isolated from the wall thickness.

This experiment primarily studied the stabilization height relative to jet exit velocities.

Eickhoff et al. (1984) investigated burner stability using nozzle diameters ranging from 4 mm to 20 mm. Natural gas (85% methane) was the fuel utilized. Both tube and contoured nozzles were used, providing a fully developed and flat velocity profiles, respectively. It was observed that the lift-off velocity was independent of diameter for the contoured nozzle. The lift-off velocity of tube burners (fully developed velocity profile), however, shows some dependence on the diameter for diameters less than 6 mm. The lift-off velocity increases nonlinearly when the tube diameter is decreased below 6 mm. The same observation was reported by Donnerhack and Peters (1984).

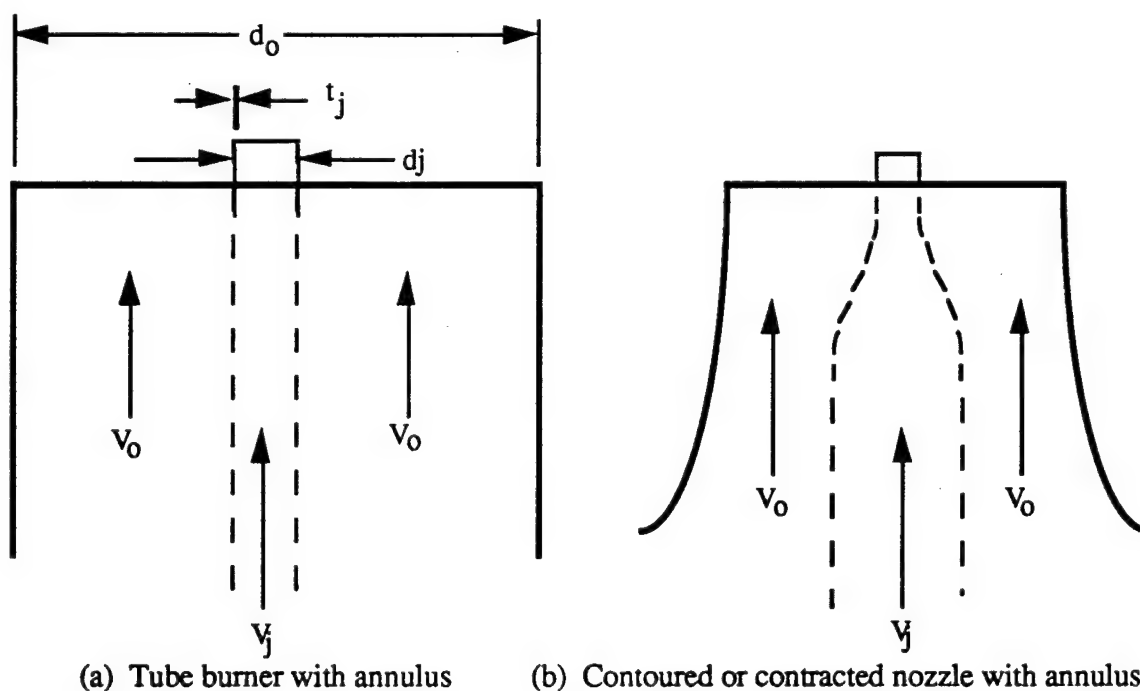


Figure 1.2 Typical Geometry Configurations

Takahashi et al. (1980, 1984, 1990a, 1990b) did an extensive investigation on the lift-off of jet diffusion flames. The burner tube exit diameters range from 0.59 to 5.98 mm and the lip thicknesses from 0.04 to 2.4 mm. The experimental arrangement consisted of a tube centered in an annulus of air. The fuels used were hydrogen and methane. At low annular velocities (<1 m/s) the diameter effects agreed with previous investigators, i.e. Eickhoff et al. (1984), and Donnerhack and Peters (1984). For methane flames, a lip thicknesses less than the flames minimum quenching distance (approximately 2 mm) shows no effect on the lift-off velocity (Takahashi, et al., 1990b). When the lip thickness is larger than 2 mm, a higher lift-off velocity is observed. This is attributed to a recirculation zone forming near the tube exit, resulting in flame stabilization similar to that of a bluff body.

1.2.2.1.2 Thermochemical Effects

The thermochemical effects at the burner exit include different fuels and fuel-inert mixtures (dilutions), and preheating the fuel prior to the burner exit. Three fuels have been studied, i.e., hydrogen, methane, and propane. Hydrogen has the highest lift-off velocity (approximately 600 m/s), followed by methane (approximately 30 m/s), and Propane (approximately 20 m/s) for burner exit diameters between 1 and 20 mm. The diluents used consist of inert gases such as argon, nitrogen, carbon dioxide, and helium. The dilutions decrease the lift-off velocity as the concentrations of inerts increase relative to the fuel (Takahashi, et al., 1984, and Gollahalli, et al., 1986). Takeno and Koteni (1975) tested pure and diluted hydrogen jet diffusion flames in a coflowing annular environment. The fuel and fuel dilutions were preheated prior to the burner exit. It was observed that the lift-off velocity increased with increasing temperatures of the preheated fuel and diluent mixtures.

1.2.2.1.3 Fluid Mechanical Effects

The effect of the velocity profile and turbulence quantities of a combustng jet are summarized. The lift-off velocity is independent of the burner diameters with a flat velocity profile at the exit. The lift-off velocity, however, is a function of the fully developed profile for exit diameters less than 6 mm (Horch, 1978, Zsak et al., 1984, Eickhoff et al., 1984, and Shekarchi et al., 1988). Information on turbulence effects at the burner exit is limited. Takahashi et al. (1984, 1990b) obtained velocity data using laser Doppler anemometry (LDA) near the burner exit, for near lift conditions of hydrogen and diluted hydrogen jet diffusion flames. The diluents were argon, nitrogen, and helium. LDA data was taken for a methane jet diffusion flame with swirl introduced in the annulus. No conclusion was reached with respect to the velocity fluctuations (rms) at the flame zone and its effect on the lift-off process.

1.2.2.2 Boundary Conditions

1.2.2.2.1 Geometry Effects

Takahashi et al. (1990a) investigated the size effects of the annulus (d_0) on the lift-off of hydrogen jet diffusion flames as illustrated in Fig. 1.2. The annuli tested consisted of a contraction nozzle (100 or 150 mm in exit diameter with contraction ratios 9 and 4, respectively). The annuli are designed for a uniform flow field. The average annular velocities ranged from 0 to 40 m/s. At low annular velocities (< 5 m/s) the different geometry had no effect on the lift-off velocity. The larger annulus created a more stable environment for the jet at average velocities greater than 5 m/s. In other words, the lift-off velocity increased with the larger annulus.

1.2.2.2.2 Thermochemical Effects

The addition of inert gas (nitrogen, helium, argon, and carbon dioxide) to the oxygen or air environment of the annulus has been investigated. Gollahalli (1977) diluted air with additional amounts of nitrogen or carbon dioxide to determine the stability effects on a propane jet diffusion flame. The additional diluents caused the flame to lift at a lower velocity. Carbon dioxide was observed to be a more unstable additive compared to nitrogen, lifting at lower jet exit velocities.

Takahashi et al. (1980, 1984) diluted both the oxygen annulus and hydrogen jet diffusion flame with argon, helium, and nitrogen. As the annulus dilution increased (by decreasing the oxygen supply), the flame moved radially outward and the flame angle increased relative to the axial direction. The jet lift-off velocity decreased with increasing annulus dilutions.

1.2.2.2.3 Fluid Mechanical Effects

The average velocity of the annulus has a significant effect on the lift-off velocity. Dahm and Dibble (1988) studied the stability of methane and propane jet diffusion flames at three different annular conditions; 0.37, 0.58, and 0.80 m/s. It was observed that increasing the annular velocity from 0.37 to 0.80 m/s would decrease the lift-off velocity by 20%.

Takahashi et al. (1990a, 1990b) most recently documented the velocity effects on hydrogen and methane jet diffusion flames. The average annular velocity was 0 to 40 m/s and 0 to 5 m/s for the hydrogen and methane jet diffusion flames, respectively. The increase in annular velocity decreases the lift-off velocity of the jet diffusion flames which agrees qualitatively with Dahm and Dibble (1988). Takahashi et al. (1990a, 1990b) also determined the velocity field and turbulence intensities by LDA. It was conjectured that the

velocity gradient at the nozzle exit formed by the boundary layer in the annulus may be a better correlating variable than the mean velocity for analyzing the lift-off process. The effects of the coflow on the entrainment velocity at the burner exit is viewed as the key in determining a quantitative flame stability model. The turbulence quantities obtained were inconclusive in determining their role on the lift-off process.

1.3 Objectives of the Study

From the literature review, it becomes clear that, although there exist many previous studies on lifted jet diffusion flames, the mechanism(s) responsible for the lift-off is still not clear. The purpose of this research is to characterize the velocity field near the exit of a methane jet diffusion flame located in the center of a large annulus and to shed some light on the lift-off process. The jet velocity was set near the instability point (V_{crit}), prior to lift-off. Two major parameters were studied to determine their effects on the lift-off process. Dilution, and annulus effects were analyzed. Three different inert gases were used, helium, nitrogen, and argon. The flow field at different annulus conditions were determined by one and two channel LDA systems, and the dilution conditions were recorded with a one channel LDA system.

The specific objectives of this research were:

- (1) To investigate effects on lift-off due to dilution, and annulus conditions which are represented by stability curves,
- (2) to document velocities of the near field region of a combusting jet, and
- (3) to evaluate current lift-off theories.

CHAPTER II

EXPERIMENTAL SETUPS AND PROCEDURES

2.1 Introduction

This chapter describes the experimental arrangements and techniques for velocity measurements, determination of stability conditions and flame locations. Two test facilities were utilized, the Aero Propulsion and Power Laboratory, Wright Research and Development Center (WRDC) located at Wright Patterson Air Force Base, Ohio, and that at the Department of Mechanical Engineering, The University of Iowa (UI), Iowa City, Iowa. The velocity measurements include both the axial and radial components of the mean and fluctuation velocities. Stability curves were obtained using different annular flow rates, fuel dilutions, and nozzle geometries. The hot (flame) zone was determined at the UI for the dilution conditions used in the laser Doppler anemometry (LDA) work. A thin filament (SiC fiber) was used to determine the hot zone in the flame near lift-off. The test facility at each location are described in the next section, followed by the instrumentation, test conditions, and experimental methods utilized in the study.

2.2 Experimental Facilities

2.2.1 WRDC Facilities

The test apparatus consists of a combustor, gas tanks, a dry air delivery system, and an exhaust hood vented to the atmosphere. The combustor houses the jet burner, and provides a dry air annular flow surrounding the burner. Two types of burners, a contoured and a tapered nozzle, are used. The contoured and tapered nozzles were 4.67

and 5.01 mm in diameter, respectively. Three different inert gases are utilized, nitrogen, helium, and argon. The fuels used are methane and propane. The experimental set-up is illustrated in Fig. 2.1 with the burner positioned vertically upward.

The combustor assembly was mounted on a three-dimensional traversing mechanism. The traversing mechanism was controlled by stepping motors with ± 0.025 mm resolution in all directions. The stepping motors were driven by a controller (Sony Modiac) interfaced with a minicomputer (MODCOMP Classic).

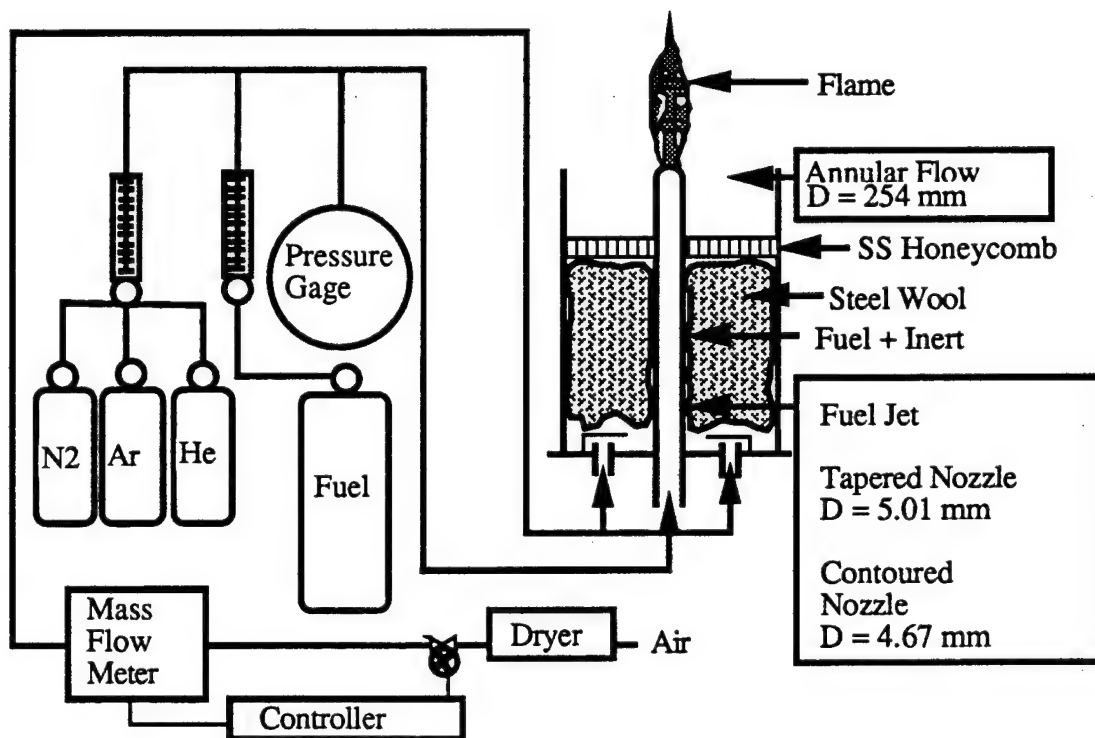


Figure 2.1 WRDC Experimental Setup

The burner nozzle tip was extended above the exit plane of the annulus allowing for LDA laser beam passage. The annular flow assembly is designed with baffle plates located in the settling chamber which is packed with steel wool between the air inlet and the honeycomb section, Fig. 2.1. The stainless steel honeycomb is 6 mm thick and has 2 mm cells. The honeycomb was placed perpendicular to the axial direction, in the annular flow assembly upstream of the burner exit plane. The burner was situated under a ventilated hood with window screens hanging from the hood, around the burner. The hood was ventilated by a $0.9433 \text{ m}^3/\text{s}$ (2000 CFM) fan system, with a 460 mm (18 in.) diameter duct vented to the atmosphere.

Rotameters (Matheson, tubes 602 through 605), were used to regulate the fuel and inert gas flow rates. The accuracy of the rotameters were $\pm 3\%$ of the flow rate. A pressure gage was placed downstream of the rotameters to monitor the pressure drop from the rotameters to the burner exit. The pressure drop during the experiment was less than 0.1 psig. The pressure gage also served as an indicator in case of blockage or choked condition occurring in the flow line. The annular flow was regulated by a mass flow meter and controller (Technology Inc.) in conjunction with an automated inline pneumatic valve. The air was dried to a dew point temperature of -40°C .

The tapered nozzle has a maximum outer diameter of 25.4 mm and tapers to 5.01 mm at the exit. A total contraction length of 100 mm is required for the 5.01 mm diameter tapered nozzle, forming a 2.9 degree angle from the axial direction. The contoured nozzle has a maximum outer diameter of 25.4 mm, and contracts over a 20 mm length to a 4.67 mm exit diameter at the burner tip. Both nozzles have a lip thickness of 0.3 mm. The nozzle geometry is shown in Fig. 2.2.

The LDA system provided two-channel measurements (axial and radial directions).

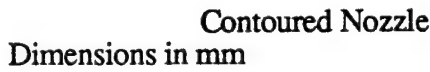


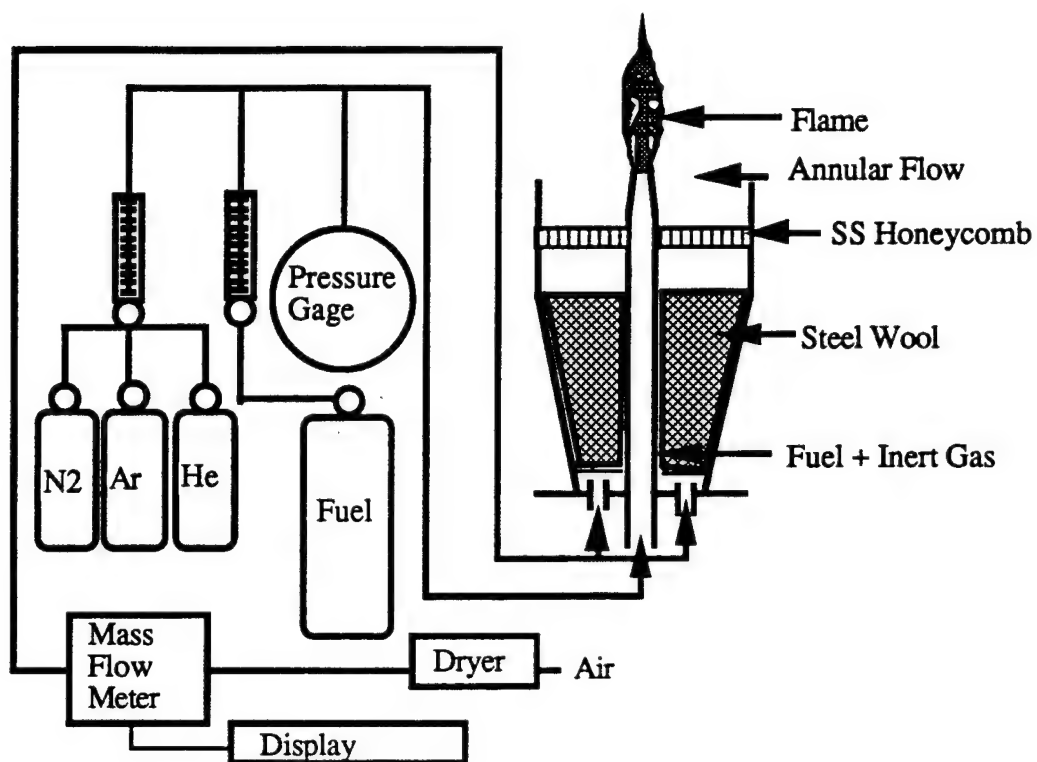
Figure 2.2 Nozzle Geometries

Since a LDA system was employed, seeding particles were required. Micron-sized Al_2O_3 powder was used to seed the jet and annulus. The LDA signals were processed with burst counters (TSI signal processors). The Doppler bursts were compared in a 20 ms window to assure the correlated bursts of each channel. The signal processor sent the data to a minicomputer (MODCOMP Classic) for data reduction and storage. The same computer system was used to control the traversing system.

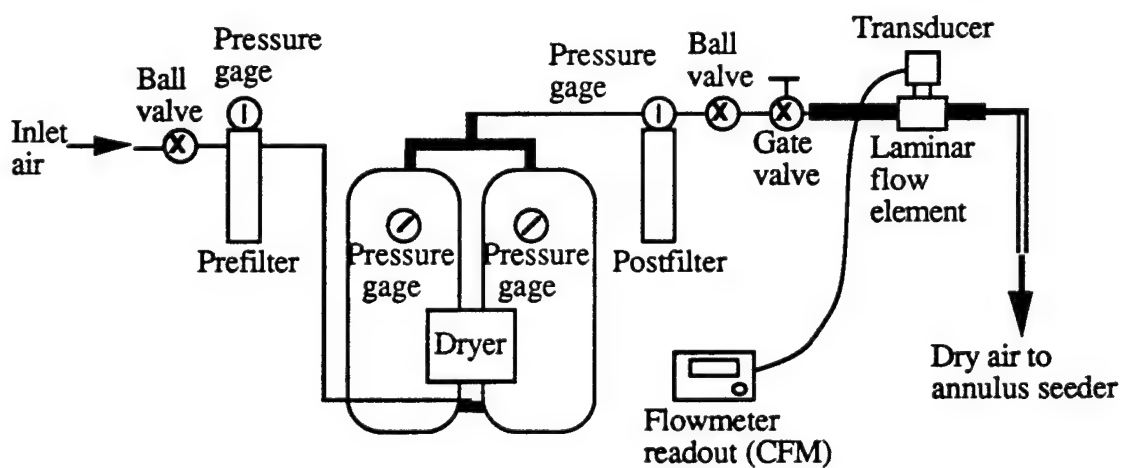
2.2.2 UI Facility

The experimental apparatus at UI consists of a combustor, gas tanks, dry air system, and an exhaust system. The experimental schematic is shown in Fig. 2.3 (a). The combustor was mounted vertically upward on a two-dimensional traversing mechanism. The combustor consists of an annulus and fuel jet nozzle centered in the annulus. The schematic of the combustor is shown in Fig. 2.4. The annulus is 0.2477 m (9.75 inches) in diameter, has a divergent section 30 degrees from the vertical, made of a nylon block. The air enters the annulus from four inlets at the bottom plate of the divergent section. The divergent section has a baffle plate at each air inlet and the diffuser is packed with steel wool. A 0.2540 m (10 inches) diameter pexiglass tube is attached to the exit of the divergent section, to form the annular flow. The pexiglass tube has an inner diameter of 0.248 m (9.75 inches) and a length of 0.3048 m (12 inches). Stainless steel honeycomb (furnished by WRDC) is placed inside the pexiglass tube for flow straightening. It should be mentioned that the diameter of the annulus of the UI combustor is the same as that at WRDC.

The fuel jet nozzles used at the UI facilities are provided by WRDC, having the geometries shown in Fig. 2.2. The fuel jet nozzle is positioned at the center of the annulus



(a) Schematic of Test Section



(b) Air System

Figure 2.3 UI Experimental Setup

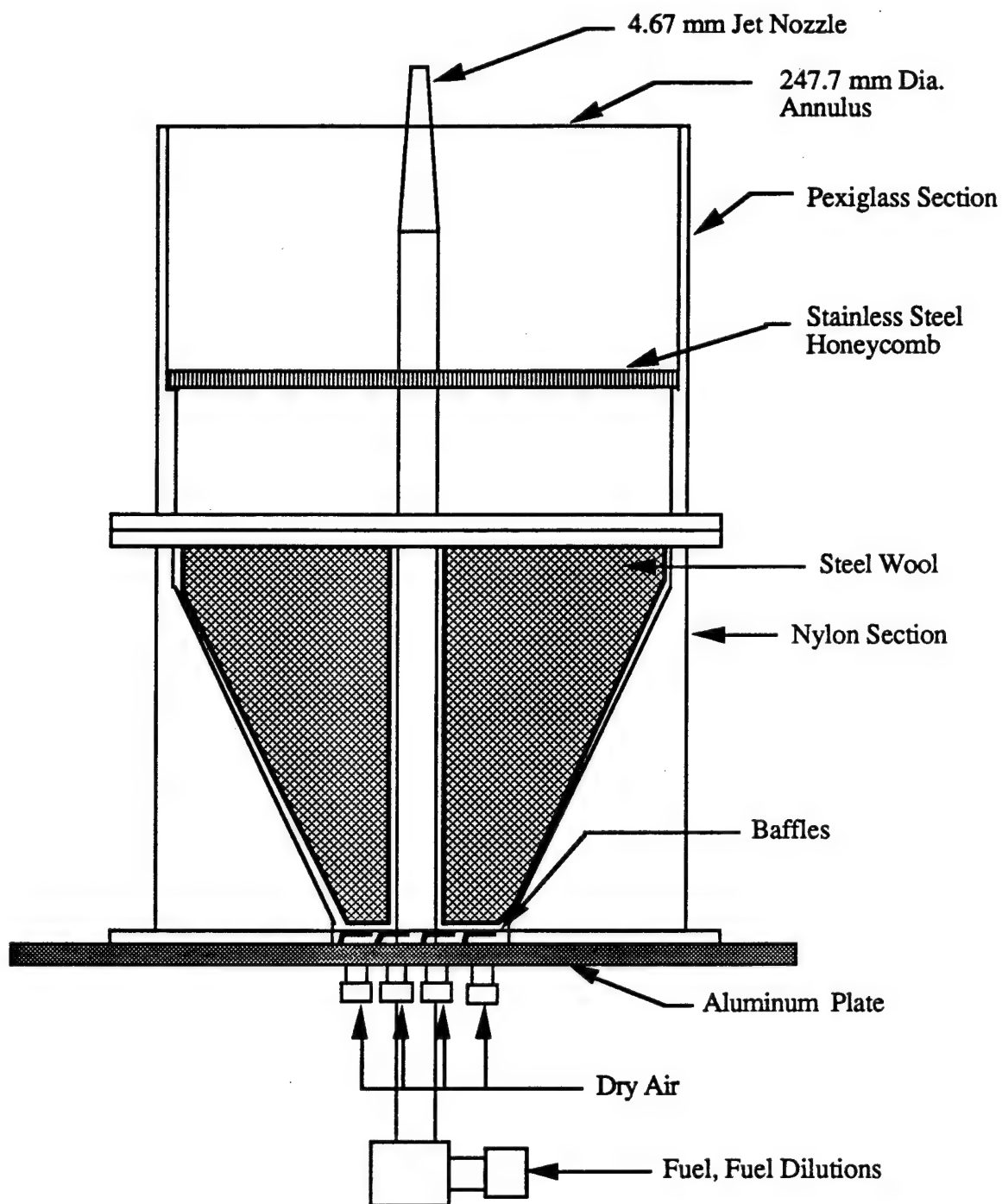


Figure 2.4 Schematic of the Combustor Design at The University of Iowa

with the jet exit 25 mm above the annular exit plane. Rotameters (Matheson tubes 602 to 605) are used to regulate the jet flow rate. The same rotameters were used in the experiments conducted at WRDC as described in section 2.2.1.

The air supply system is illustrated in Fig. 2.3 (b). A desiccant dryer (Sullair 190) was installed upstream of the test section. The air is dried to -40°C dewpoint with a $0.0905\text{ m}^3/\text{sec}$ (190 CFM) flow rate capacity. The compressed air was maintained at 0.72 MPa gage pressure (90 psig) during the experiment. A prefilter and postfilter (MPF35 and MPH 28, respectively) were installed in the dryer system to remove oils and contaminants larger than $5\text{ }\mu\text{m}$.

The air flow rate was regulated by a gate valve. The flow rate was monitored by a mass flowmeter (Teledyne Hastings-Raydist Model HFM-200). The mass flowmeter consisted of a laminar flow element 76.2 mm (3 inch) in diameter with a 0.6096 m (2 ft) long section prior to the flow element. The transducer sends the flow rate signal to a digital readout module (model PR-4A5) which displays the flow rate in standard ft^3/min (SCFM). The flow range is calibrated for 0 to $0.0236\text{ m}^3/\text{s}$ (0 to 50 SCFM). The resolution of the module readout is $\pm 0.05\text{ SCFM}$. The air system pressure was monitored by the pressure gages on the dryer.

The exhaust system consists of a large hood, connected to a 0.3556 m (14 in) round duct attached to a blower. The hood is $1.22\text{ m} \times 1.22\text{ m} \times 1.22\text{ m}$ (4 ft x 4 ft x 4 ft) with the duct centered at the top of the hood. Aluminum honeycomb with 5 mm grid spacings and 12 mm thick was placed at the duct entrance. Fine mesh copper screen (1 mm grid spacings) was placed in the duct between two pieces of the honeycomb. This is required to minimize the swirling effects induced by the exhaust system. The exit plane of the burner is approximately 2 meters from the exhaust duct. A blower (Dayton model 3C494, with a full capacity of $1.415\text{ m}^3/\text{s}$ or 3000 SCFM) was placed 3 m downstream of the hood with a

reduced capacity of $0.9433 \text{ m}^3/\text{s}$ (2000 CFM) in the present setup. Fine mesh screen was attached around the hood, surrounding the test section.

The LDA system requires seeding particles in the flow. Aluminum oxide (Al_2O_3) particles were used to seed the flow. The particles had a median diameter of $0.34 \mu\text{m}$ as determined by Park (1987). The density of the particle was found to be $3960 \text{ kg}/\text{m}^3$. A mechanical vibrator was used to increase and stabilize particle seeding levels. The vibrating seeder and combustor were grounded to reduce electrostatic effects.

A two-dimensional traversing mechanism was designed and constructed for translating the combustor with respect to a fixed LDA optical axis. The traversing mechanism consists of stainless steel rods and linear bearing assemblies using unislides (model A2518DM) which are used to determine the position. The accuracy of the radial direction (z-direction) is $\pm 0.025 \text{ mm}$. The unislide responsible for centering the burner with respect to the major axis of the LDA measuring volume (y-direction) has an accuracy of $\pm 0.5 \text{ mm}$.

2.3 Instrumentation

2.3.1 WRDC Instrumentation

The laser Doppler anemometry (LDA) system at WRDC was operated in a 30 degree off-axis, forward-scattering mode. Two components of velocity were measured simultaneously, the components were separated from the measurement volume by employing the polarization technique. The velocity components measured were at ± 45 degrees from the axial and radial coordinates. The laser was operated in the single line mode, the wavelength was set at 514.5 nm (green light) and the power was fixed at 1.2 W . The laser beam was split into three beams of equal intensity. The beams were 50 mm apart and formed two sets of fringes at the measuring volume. The measuring volume was ellipsoidal in shape, with 0.21 mm and 4.3 mm for minor and major axes, respectively.

The arrangement had a fringe spacing of $5.27\ \mu\text{m}$ which is employed in calculating the velocities. Detailed dimensions of the measuring volume are presented in Appendix A.

The main components of the LDA system are numbered in Fig. 2.5 and include a 5 W Argon-ion laser (Spectrum Physics Model 2020-05), two Bragg cells (3,3A), Bragg cell power supply (4), two beam splitters (2), two beam polarizers and beam steering lenses (6), an aperture plate (7), and a 76.2 mm (3 inch) diameter lens with a focal length of 400 mm (8). The receiving optics consists of a concave mirror with focal length of 400 mm (9), a focusing lens (10) which focuses the scattered light to a prism (11) which separates the light by polarity to a fiber optical tip (12). The specifics of the numbered components are listed in Appendix B.

2.3.2 UI Instrumentation

The LDA system was operated in a forward dual-beam scattering mode in conjunction with a burst counter signal processor. The main components of the LDA system included an Argon ion laser (Spectrum Physics Model 165), a Bragg cell frequency shifter (TSI Model 9182), a photomultiplier (TSI Model 9162), and a receiving assembly (TSI Model 9140). The laser was operated at a single-line mode, the wavelength was set at 514.5 nm (green light) and power output was fixed at 400 mW. A color filter (514.5 nm, TSI Model 9158) was used to improve the signal quality.

The laser beam was split into two equal intensity beams with a 50 mm beam spacing using a beam splitter (TSI Model 9115-1). The two beams were focused with lenses having a focal length of 250 mm and crossed each other at the half-angle 5.52 degrees. The resultant measuring volumes are 0.13 mm and 1.37 mm for minor and major axes, respectively. The arrangement had a fringe spacing of $2.68\ \mu\text{m}$, which was employed in

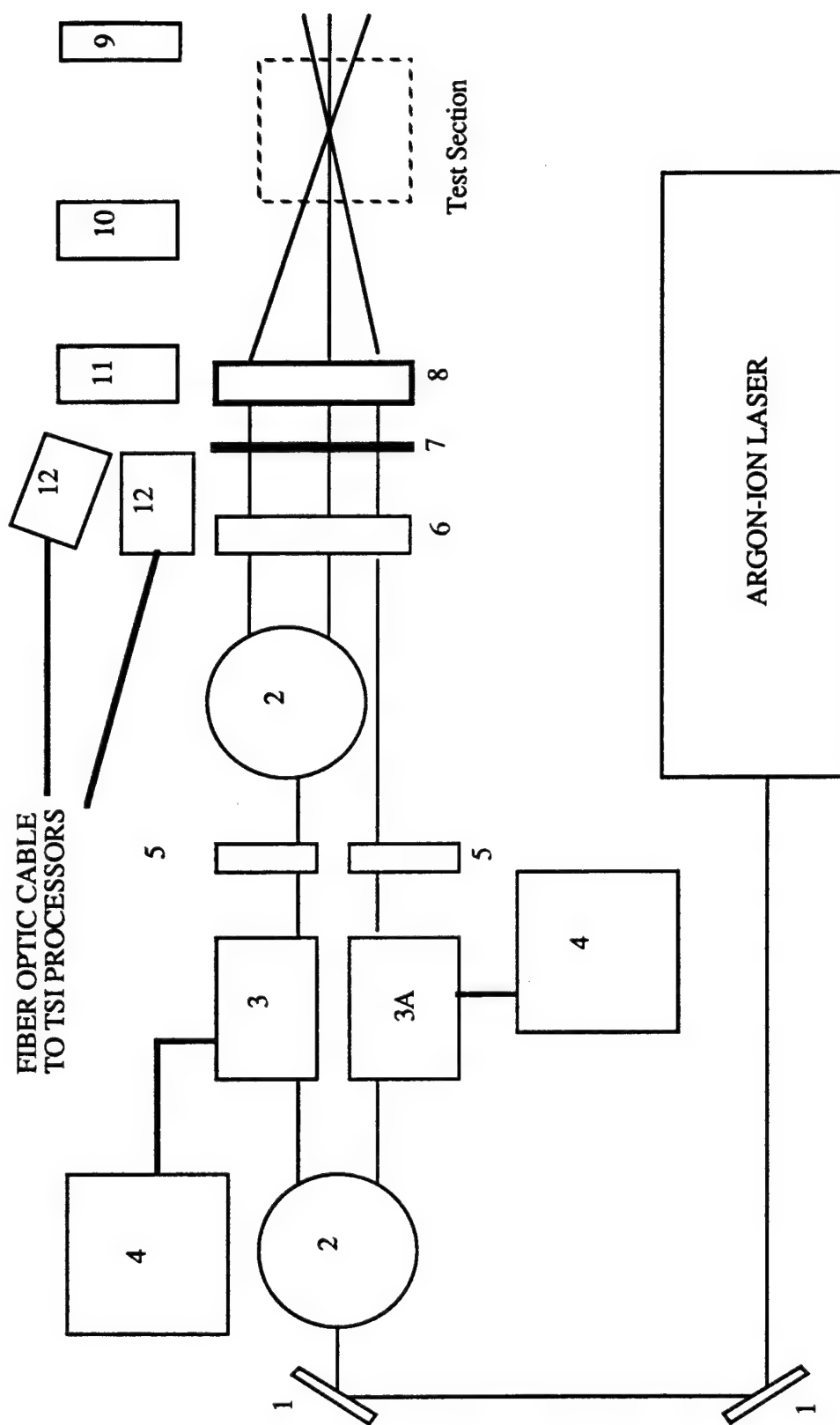


Figure 2.5 WRDC LDA System

calculating velocities. Detailed dimensions of the measuring volume are included in Appendix A.

The LDA signal was processed by a burst counter (TSI Model 1984). The timer (TSI Model 1985) and counter were operated in the N-cycle mode at 32 cycles per burst, but only one measurement per burst was recorded. The burst counter processed data are sent to a microcomputer (Macintosh IIfx) based data acquisition system, employing a digital input, output board (National Instruments Model NI DIO32F), and commercial software (Labview by National Instruments) as shown in the schematic of the data acquisition system in Fig. 2.6.

2.4 Experimental Conditions

Experiments were first conducted to determine the lift-off (or burner stability) conditions of methane and propane jet diffusion flames as a function of the annular velocity and fuel dilution. Two different burners, a contoured and a tapered nozzle were examined. The exit diameter of the tapered and contoured nozzles at WRDC were 5.01 and 4.67 mm, respectively. The tapered nozzle used at the UI has a 4.67 mm exit diameter. Three inert gases were utilized: nitrogen, helium, and argon.

Recognizing the importance of the boundary condition on the lift-off of jet diffusion flames, LDA measurements were made near the burner exit plane of the nozzle at 0.9 mm and 1.8 mm above the exit plane at WRDC and UI, respectively. Conditional sampling was used, i.e. either the fuel jet or the annular air was seeded. The tapered nozzle was used for all velocity measurements using the LDA technique. The tapered nozzle was used instead of the contoured nozzle for LDA measurements. The nozzle was cleaned periodically as the Al_2O_3 particles collected on the nozzle which affects the lift-off process.

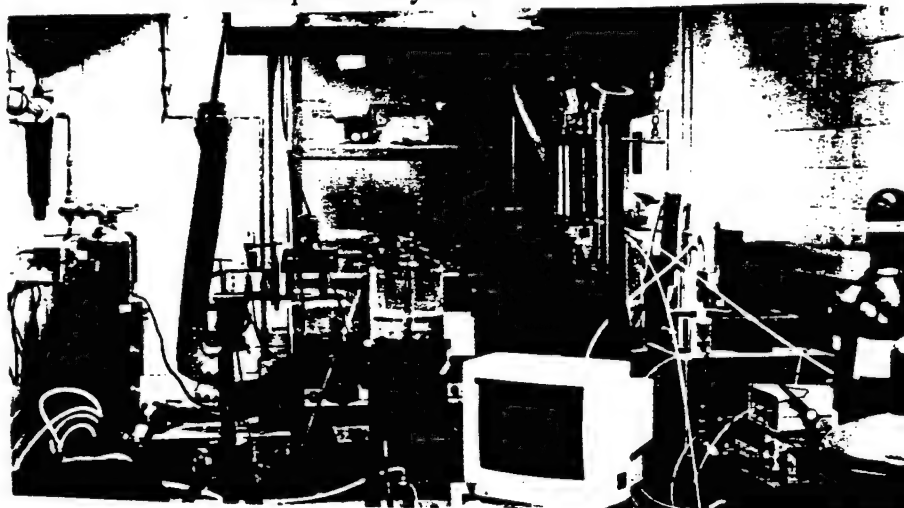
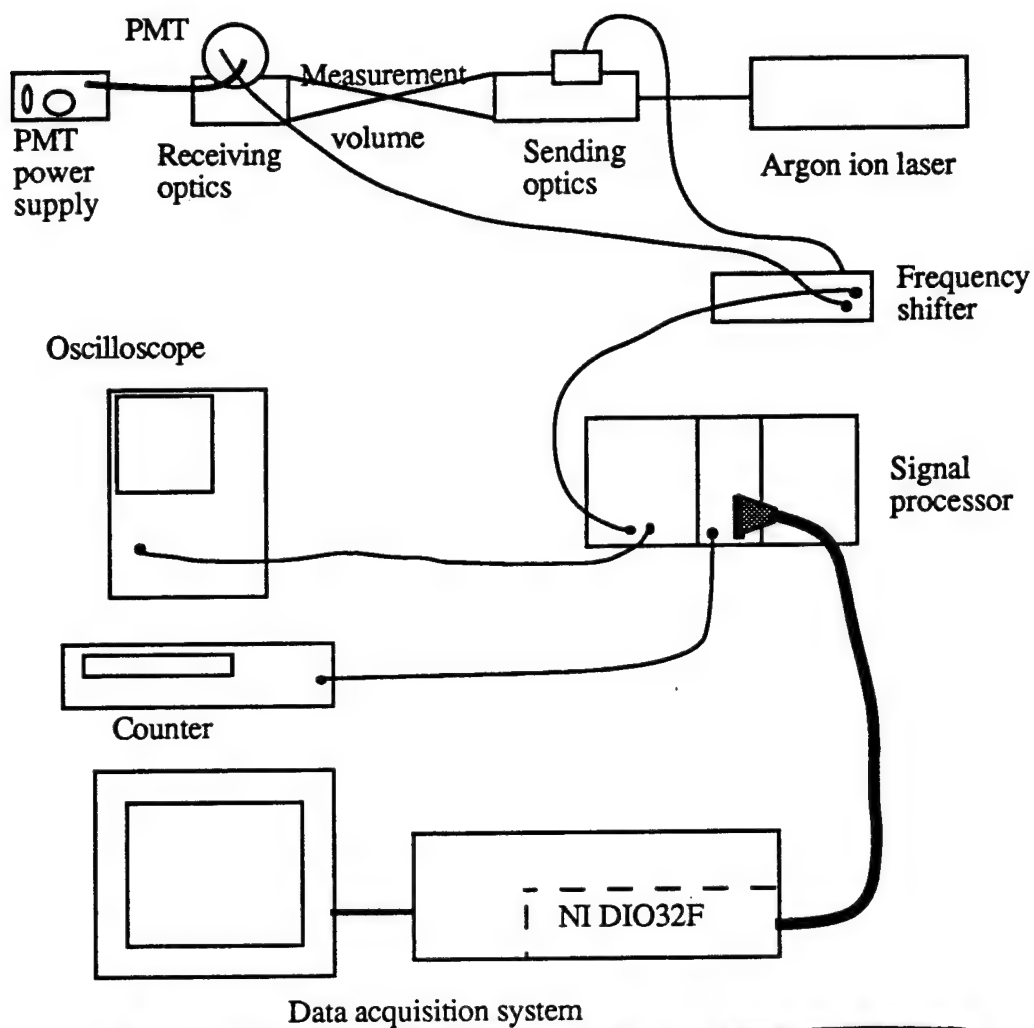


Figure 2.6 UI LDA and Data Acquisition System

LDA measurements were taken at three annular flow conditions as summarized in Table 2.1. For a pure methane flame, LDA measurements were taken at WRDC and UI for all three conditions. At Condition B, (representing $7.67 \times 10^{-3} \text{ m}^3/\text{s}$ and a 0.15 m/s average annular velocity) LDA measurements were taken at various methane dilutions at UI only. The Re number is based on the hydraulic diameter, air property at 25° C, and the volumetric mean velocity of the annulus.

Table 2.1. Diffusion Flame Test Conditions

	Annular Flow Rate, m^3/s	Annular Flow Velocity, m/s	Annular Flow Re
Condition A	3.83×10^{-3}	0.07	1592
Condition B	7.67×10^{-3}	0.15	3184
Condition C	15.33×10^{-3}	0.30	6368

2.5 Experimental Methods

2.5.1 WRDC

Stability curves were obtained for methane and propane jet diffusion flames using the tapered and contoured nozzles at three different annular flow rates (Conditions A through C of Table 2.1). From the experiments, stability conditions for LDA measurements were identified. The effects of LDA seeding on the lift-off process were also noted.

The lift-off condition was obtained by maintaining a constant fuel flow rate while increasing the inert gas flow. The lift-off velocity was determined visually by the detachment of the flame from the burner. The inert and fuel flow rates were recorded at

lift-off. The lift-off procedure was repeated several times at one fuel flow rate, until a consistent lift-off velocity was obtained.

The two-channel LDA system was checked by taking measurements at the exit of a contoured nozzle. The exit profile is flat, so the average velocity given by the rotameter reading represents a good approximation of the average LDA velocity. Several different flow rates were compared to the LDA measurements. Each measurement was within five percent of the average velocity.

The separation of each measurement channel was accomplished by the polarization technique. This requires the polarity of both crossing beams to be 90 degrees out of phase. The resulting signals from the Mie scattering of the particle were separated by polarity using a prism.

Two Bragg cells were used, operating at 40 and 35 MHz to produce a combined frequency shift at the measurement location of 5 MHz. Typical sample rates were 1 to 10 kHz. The jet regime maintained a high sample rate (10 kHz) while the lower annular velocities maintained a 1 kHz data rate. Data rates at the flame location were the lowest, at approximately 100 Hz. Typically, the data at the flame location were taken for a period of 1 to 6 minutes.

LDA measurements at the tapered nozzle and the annulus (Conditions A through C) exit were obtained at lifted and near lifted conditions. The increments in the radial position were set at 10 mm for the annulus region, and 1 mm and 0.1 mm for the flame zone. The measurements were taken 0.9 mm above the burner exit plane.

The two-channel LDA measurements were set at ± 45 degrees from the radial direction, e.g. see Fig. 2.7. The axial and radial velocities were determined from the measured velocities. Specifically, the axial (U) and radial (V) velocities are obtained from

$$U_j = U_j^+ \sin\theta + U_j^- \cos\theta \quad (2.1)$$

$$V_j = U_j^+ \cos\theta - U_j^- \sin\theta \quad (2.2)$$

where U_j^+ and U_j^- denote the measured velocities at +45 and -45 degrees, respectively. The vectors are defined in Fig. 2.7. The exact angle θ was determined by centering the radial velocity sign change at the geometric center of the nozzle. The results reported in this thesis use a compensated angle of 44.75 for the LDA data taken at WRDC.

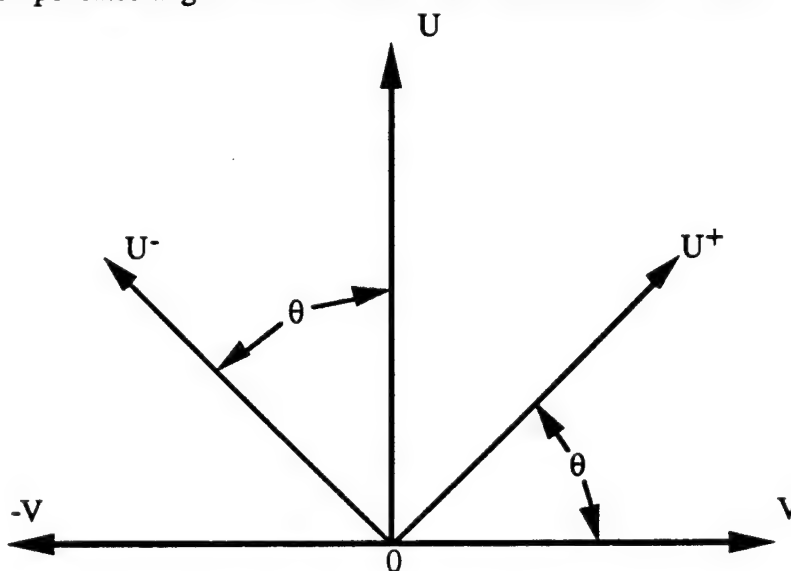


Fig. 2.7 Vector Orientation

Mean and rms (root mean squared) velocities were calculated based on the sample size of 3000 data points. The mean velocity was obtained by the relation:

$$\bar{U} = \frac{\sum_{j=1}^N \frac{U_j}{U_j + c}}{\sum_{j=1}^N \frac{1}{U_j + c}} \quad (2.3)$$

where \bar{U} is the mean velocity, N is the total number of samples taken, U_j is the instantaneous velocity, and c is a constant representing the product of the fringe spacing and frequency shift used in the experiment. The root-mean-squared (rms) velocity is calculated by:

$$U_{rms}^2 = \frac{\sum_{j=1}^N \frac{(U_j - \bar{U})^2}{U_j + c}}{\sum_{j=1}^N \frac{1}{U_j + c}} \quad (2.4)$$

Equations 2.3 and 2.4 compensate for high velocity bias. They represent the time averaged quantities derived from the discrete sampling. The derivation of these equations are in Appendix C.

The confidence limits of the mean and rms velocities are estimated following the analysis of Bates and Hughes (1977). The analysis assumes a Gaussian distribution for turbulent fluctuations. The confidence limits for the mean velocity are calculated from:

$$\bar{U} - Z_{\alpha} \frac{\sigma}{\sqrt{N}} \leq \xi \leq \bar{U} + Z_{\alpha} \frac{\sigma}{\sqrt{N}} \quad (2.5)$$

where \bar{U} is the mean velocity, ξ is the population mean velocity, σ is the population standard deviation, N is the sample size, and Z_{α} is 1.96 for the 95% confidence interval. Equation 2.5 is rearranged to yield an equation for a 95% confidence limit, meaning that measured mean velocity differs from the true mean velocity by less than 5%. The equation

$$N = 1600 \left(\frac{U_{rms}}{\bar{U}} \right)^2 \quad (2.6)$$

where U_{rms} is the measured rms velocity. At U_{rms}/\bar{U} (turbulence intensity) = 1, the calculated sample size is 1600. The present two-channel LDA measurements used a sample size of 3000, and the results reveal that the turbulence intensity is below one at all positions measured. With the sample size 3000, the mean velocity obtained in the present study has a confidence level better than 95%.

The velocity fluctuation confidence interval is

$$\sigma_s - \frac{Z_\alpha \sigma}{\sqrt{2N}} \leq \sigma \leq \sigma_s + \frac{Z_\alpha \sigma}{\sqrt{2N}} \quad (2.7)$$

where σ_s is the sample standard deviation. The sample size can be obtained from equation 2.7 for a 95% confidence interval

$$N = \frac{1.92}{E^2} \quad (2.8)$$

where E is defined as

$$E = \frac{\sigma - \sigma_s}{\sigma} \quad (2.9)$$

Substituting a 5% error in the equation, a sample size of 768 is required, a value less than the 3000 samples taken in this experiment.

2.5.2 UI

The tapered nozzle was used for the experiments conducted at the UI. First, stability curves were obtained for diluted methane and propane jet diffusion flames. The inert

diluents were the same as those used at WRDC, i.e. nitrogen, argon, and helium. Several annular flow rates were used in determining the lift-off velocity for pure fuel.

Condition B (of Table 2.1) was chosen as a representative condition in taking LDA measurements and determination of the flame zone. The flame zone location was determined at the near nozzle exit. A 15 μm diameter silicon carbide fiber was placed at the flame base. The fiber emits gray body radiation (Chen and Goss, 1989), illuminating the high temperature (flame) zone. A 35 mm camera (Pentax, Model K1000) was used to take photographs showing the flame location. A 200 mm zoom lens (Tamron, Model BBAR UC) with a 2x multiplexer (Tamron, Model 58A) was used to increase the resolution at the flame base. The camera was set at f22 (minimum), and 1/8 shutter speed with the zoom lens fully extended. The film used was ASA 400 black and white. The scaling of the flame photographs was provided by a photograph of a 1 mm grid attached to the nozzle exit. A micrometer was used to determine the scale of the pictures and measure the flame location relative to the nozzle exit.

The velocity measurements were taken at the flame base prior to lift-off which is 1.8 mm above the exit plane of the burner. The lift-off velocity of the diluted jet diffusion flames were obtained by setting the fuel flow rate constant and increasing the diluent flow rate. The LDA measurements were taken at slightly lower diluent flow rates (within 2%) to insure flame stability during seeding.

The LDA setup with a digital interface to a microcomputer (Macintosh IIX) for data acquisition required validation. The data acquisition was tested by a function generator (HP Model 3312A) over a 5 kHz to 13 MHz range. The function generator was also connected to a timer (HP Model 5326A). The output file of the data acquisition system registered the same frequency as the timer at the frequency tested. The TSI counter and frequency shifter were tested per TSI instruction manuals. A function generator was

connected to the counter and operated from 1 kHz to 10 MHz. The output of the counter was identical to that of the signal generator. The frequency shifter was checked with a counter (HP Model 5326A) at 100 kHz, 500 kHz, 1 MHz and 10 MHz, the frequency shifter was within 0.000001% at 10 MHz for 5 minutes.

The LDA system was checked using a rotating disk at a fixed rpm as shown in Fig. 2.8. The disk consisted of a long radial slot in which a 30 μm diameter thermocouple wire was placed across the slot at eight locations. This provided eight bursts per revolution of the rotating disk. The output shaft of the motor was controlled by a sensor and digital readout (Dart Controls, S/N K01203) with an accuracy of $\pm 0.05\%$.

A one-channel LDA system was used as shown in Fig. 2.6. An orientation of ± 45 degrees (U^+ , U^-) and the axial direction (U) were measured as shown in Fig. 2.7. The time average mean and fluctuating velocities were calculated as per equations 2.3 and 2.4. The frequency shift was set at 10 MHz at all measured velocity locations.

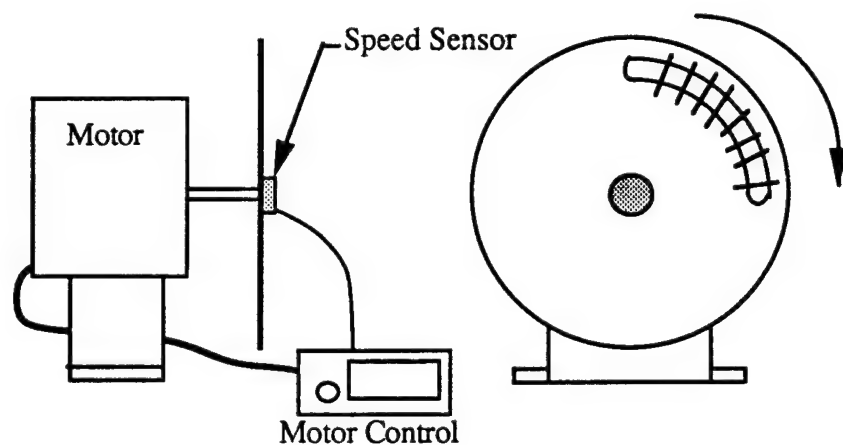


Figure 2.8 Rotating Disk for LDA Calibration

The average axial and radial components were calculated by

$$\bar{U} = \bar{U}^+ \sin\theta + \bar{U}^- \cos\theta \quad (2.10)$$

$$\bar{V} = \bar{U}^+ \cos\theta - \bar{U}^- \sin\theta \quad (2.11)$$

The average axial velocity (\bar{U}) is measured, equation 2.10 is used to compare the error between the calculated and measured values. The rms velocities include the measured axial rms, and the calculated radial rms velocities. The radial rms velocity term is calculated as follows:

$$V_{rms} = \sqrt{U_{rms}^{+2} + U_{rms}^{-2} - U_{rms}^2} \quad (2.12)$$

The Reynolds stress is calculated by equation 2.13.

$$\begin{aligned} \overline{U'V'} = & (U_{rms}^{+2} - U_{rms}^{-2}) \sin\theta \cos\theta \\ & + \frac{\cos^2\theta - \sin^2\theta}{2 \sin\theta \cos\theta} [U_{rms}^2 - U_{rms}^{+2} \sin^2\theta - U_{rms}^{-2} \cos^2\theta] \end{aligned} \quad (2.13)$$

The derivation of Equations 2.10 through 2.13 are presented in Appendix D.

The statistical analysis presented in Equations 2.5 through 2.9 is applicable, using different definitions of the mean and fluctuating velocities (equations 2.10 through 2.12). 5000 samples were taken in the jet and 3000 samples in the annulus at each orientation (axial, ± 45 degrees) which is well above the 5% confidence interval requirements for both mean and fluctuating components as shown by equations 2.6 and 2.8.

CHAPTER III

THEORETICAL CONSIDERATIONS

3.1 Introduction

The lift-off of jet diffusion flames is a local phenomenon occurring at the flame zone, near the burner exit. Two different theories are available explaining the lift-off phenomena, namely; the premixed flame model as proposed by Vanquickenborne and van Tiggelen (1966) and the extinction of laminar flamelets as conjectured by Peters and Williams (1983). The theories are not universally accepted. Current experimental data may be explained by either model as reviewed by Pitts (1988). This chapter explains the concepts of the premixed flame model and the laminar flamelet model.

3.2 Existing Theories

3.2.1 Premixed Flame Model

A schematic of the theory is shown in Figure 3.1. The premixed theory assumes that the fuel and air streams premix to the molecular level prior to reaching the flame zone. The premixed unburnt mixture velocity normal to the flame base at ambient temperature is defined as the laminar flame speed, S_u . Lift-off occurs when the local velocity of the unburnt mixture exceeds the local flame speed. Since the diffusion flames are in the turbulent regime at lift-off, the local flame speed is defined as the turbulent flame speed. The turbulent flame speed is a function of the laminar flame speed and local turbulence quantities such as root-mean-square (rms) velocities.

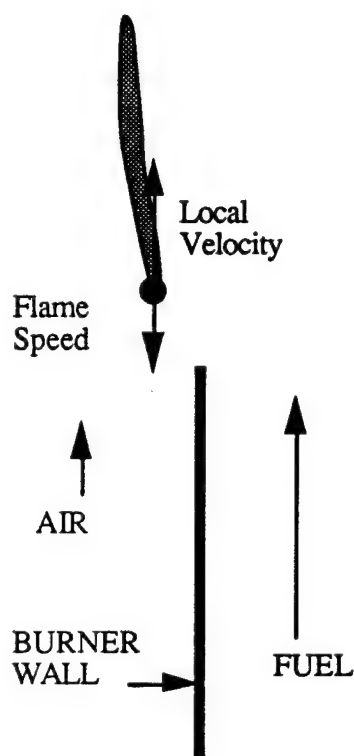


Figure 3.1. Diffusion Flame Premixed Schematic

To obtain the velocity of the unburnt mixture prior to the flame, LDA measurements were taken underneath the flame zone. The mean axial velocity represents the convective velocity of the reactant mixture, and the rms axial velocity component is used as an indicator of its effect on the turbulent flame speed. The different annular velocities (Conditions A to C) provide a range of lift-off velocities in which to compare the velocity profiles underneath the flame base.

A comparison at different lift-off velocities, enables one to analyze the premixed flame model. For example, at different annulus flow rates (Conditions A to C) the lift-off velocity varies over 30%. According to the premixed flame model, the local convective velocity of the reactant mixture (mean axial velocity) should be relatively constant at the

flame base. Diluents added to the fuel, lowers the flame speed and therefore the local convective velocity at the flame base should also decrease.

3.2.2 Laminar Flamelet Model

The laminar flamelet model assumes that the base of the flame (near burner exit) can be treated as a small laminar flamelet. The flamelet is extinguished due to local straining (dV/dr) of the flame. This is explained by the parameters affecting the reaction rate (ω). The reaction rate (ω) is defined as,

$$\omega = A \exp(-E/R_u T) \prod_{i=1}^M (C_i)^{v'_i} \quad (3.1)$$

where A represents the pre-exponential factor. E is the activation energy, R_u is the universal gas constant, T the local temperature, M is the number of species, C_i is the concentration of species i , and v'_i is the stoichiometric coefficient of species i .

Considering the specie and continuity equations and involving the conserved scalar approach, the reaction rate can be expressed as (Williams, 1985),

$$\omega = \rho D (\partial^2 Y / \partial Z^2) |\nabla Z|^2, \quad (3.2)$$

where ρ is the density of the reactants, D is the molecular diffusivity of the mixture, Y is defined as the mass fraction, and Z is the mixture fraction. Equation 3.2 is applicable when the rate of transport of the species to the reaction zone is lower than that of chemical reaction governed by Equation 3.1. As a result, the actual reaction rate is limited by the

transport of species dictated by Equation 3.2. $|\nabla Z|^2$ is the dominating term and can be related to the scalar dissipation, χ , as follows,

$$\chi = 2D |\nabla Z|^2. \quad (3.3)$$

Equations 3.2 and 3.3 relate the reaction rate to the scalar dissipation rate,

$$\omega = 1/2 \rho (\partial^2 Y / \partial Z^2) \chi. \quad (3.4)$$

The scalar dissipation term is the parameter most sensitive to initial conditions. The laminar flamelet concept places a coordinate system on the flame surface (Z_{st}), and one normal to the flame surface (η) as shown in Fig. 3.2. The flame is stretched due to the local scalar dissipation which is proportional to the mixture fraction gradient across the flame ($dZ/d\eta$). The straining rate ($dV/d\eta$) is proportional to the mixture fraction gradient assuming equal mass and momentum transport as discussed by Gibson (1968). The laminar flamelet model has been analyzed by previous investigators (Ishizuka and Tsuji, 1981) using a counter-flow diffusion flame experiment. The counter-flow diffusion flame experiment is schematically shown in Fig. 3.2(a). The laminar flamelet concept applied to the jet diffusion flame is shown in Fig. 3.2(b).

The difference between the counter-flow diffusion flame and the jet diffusion flame is the effect of flame curvature encountered in jet diffusion flames. The analysis presented by Williams (1975) states that the significance of flame stretch or the straining rate (dV/dr) is usually more important than curvature effects. Corrections for curvature are of the order of the flame thickness to the radius of curvature. This is usually smaller than the product of

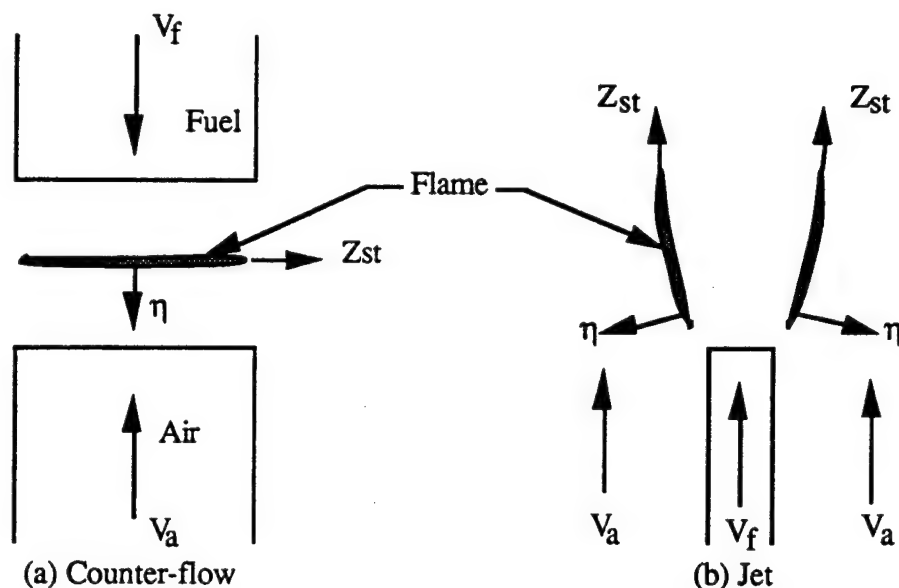


Figure 3.2 Counter-Flow and Jet Diffusion Flames

flame stretch with residence time which characterizes the influences of flame stretch. The product is of the order of the flame stretch (dV/dr).

The straining rate (dV/dr) at the flame base is increased with increasing jet exit velocity as shown by Fig. 3.2(b). Lift-off occurs when the straining rate or scalar dissipation exceeds the reaction rate given by Equation 3.1. Physically, the lift-off process occurs when the chemical reaction rate cannot keep up with the rate of diffusion of species to the reaction zone which results in local quenching of the flame.

This investigation measures dV/dr (straining rate) at the flame base. The annulus conditions provide different lift-off velocities. A comparison of the straining rates (dV/dr) at the lift-off conditions should be relatively constant since pure fuel is utilized in this case which does not affect the chemical reaction rate. Introducing diluents into the fuel side will reduce the chemical reaction rate, therefore, the straining rate will decrease at the lift-off velocity.

CHAPTER IV

DISCUSSION AND RESULTS

4.1 Stability Curves

The present study analyzes the effects of annular flow rates, diluent, fuel, and external nozzle geometry on the lift-off of jet diffusion flames. The condition when lift-off occurs relative to any combination of these effects defines a stability curve. Below the stability curve the flame is attached to the burner exit, above the curve represents a region in which the flame is blown off or is at some stabilization height downstream of the burner exit. The data for each curve presented is located in Appendix G.

Methane or propane fuels diluted with argon, helium, or nitrogen form the majority of the stability curves presented. External geometry effects are studied by using a tapered and contoured nozzle, as shown in Fig. 2.2. The annulus effects are studied in the velocity range 0 to 0.3 m/s. The jet fuel velocity at lift-off versus the annular air velocity for methane and propane jet diffusion flames using a tapered nozzle are shown in Fig. 4.1. The annular and jet exit velocities are the average exit velocities calculated from the mass flowmeter and rotameter flow rates. The annular and jet velocity profiles are flat as characterized by LDA measurements which will be discussed later (Section 4.3).

The stability curves of methane and propane jet diffusion flames shown in Fig. 4.1 reveal two regions, I and II. The maximum jet fuel velocity at lift-off occurs at an annular velocity range 0.05 to 0.07 m/s. The fuel jet velocity at lift-off decreases as the annular velocity increases beyond 0.07 m/s, up to 0.3 m/s which is the maximum annular velocity considered in the present work (Region II).

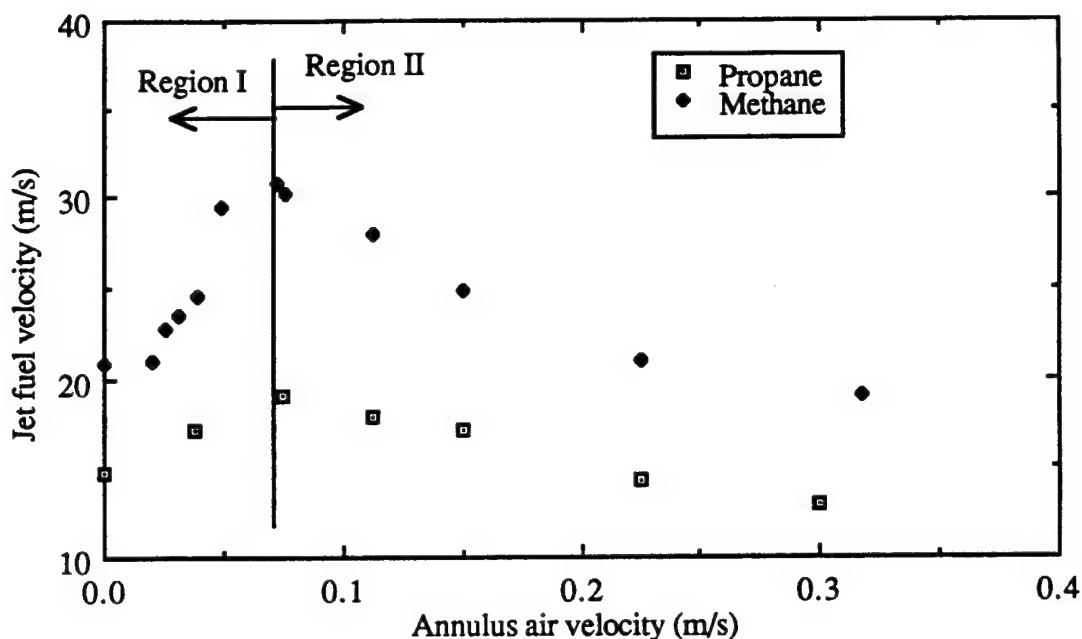


Figure 4.1 Annulus Effects on Lift-off of Jet Diffusion Flames Using Tapered Nozzle

Region II shows quantitative agreement with previous investigators, Dahm and Dibble (1988), and Takahashi et al. (1990a). Dahm and Dibble (1988) observed that increasing the annulus velocity from 0.37 m/s to 0.80 m/s decreases the lift-off velocity for methane and propane jet diffusion flames. Takahashi et al. (1990a) studied hydrogen jet diffusion flames in which the annulus air velocity varied from 0 m/s to 40 m/s. The lift-off jet velocity decreased as the annular velocity increased.

Region I of the stability curve shown in Fig. 4.1 is where the lift-off velocity increases with increasing annular flow. Takahashi et al. (1990c) observed the same trend for a methane jet diffusion flame. The propane jet diffusion flame has a lower lift-off velocity than the methane jet diffusion flame at comparable annular flow conditions. This observation is in agreement with Dahm and Dibble (1988).

Annular effects are studied in the velocity range of 0.075 m/s to 0.30 m/s to operate in region II which qualitatively agrees with previous investigations. Three annular conditions A, B, and C which represent 0.075, 0.15, and 0.3 m/s, respectively, are defined in Table 2.1. The annular velocity effects on the lift-off conditions are illustrated by Fig. 4.2. At pure methane conditions the lift-off velocities are substantially different, 31.4 m/s at Condition A versus 19.5 m/s at Condition C using the tapered nozzle. As dilution is added to the fuel, the lift-off velocity becomes less dependent on the annular flow rate. This trend was observed for all dilutions used. The methane-argon, methane-helium, and propane-argon mixtures (Figs. 4.2a, 4.2b, and 4.2c) using the tapered nozzle illustrate the annular dependence on the lift-off of jet diffusion flames. The lift-off using the contoured nozzle is less dependent on annular flow rates than the tapered nozzle as shown in Fig. 4.2(d). The contoured nozzle has a large contraction at the exit which may create a large recirculation zone from the annular air velocity. A recirculation zone would behave as a stabilization mechanism for the flame giving the contoured nozzle greater stability.

External geometry and fuel effects of a methane-argon and methane-helium dilutions are graphically represented in Fig. 4.3. Comparing the external geometry effects, Condition A shows that burner stability is not affected by the difference between the two nozzle geometries at all mixture compositions using argon and helium mixtures. The lift-off velocity decreases from 31.4 to 1.0 m/s over a fuel mass fraction range of 1.0 to 0.15 for both nozzle configurations. However, increasing the annulus velocity to Condition C revealed a significant difference in the stability of the flame between the two nozzles. At Condition C, the contoured nozzle was more stable than the tapered nozzle over the mixtures examined. For example, the methane-argon mixture has a lift-off velocity ranging from 28 to 1.0 m/s for the contoured nozzle and 19.5 to 1.0 m/s for the tapered nozzle over the fuel mass fraction range 1.0 to 0.15. The methane-argon and methane-helium mixtures

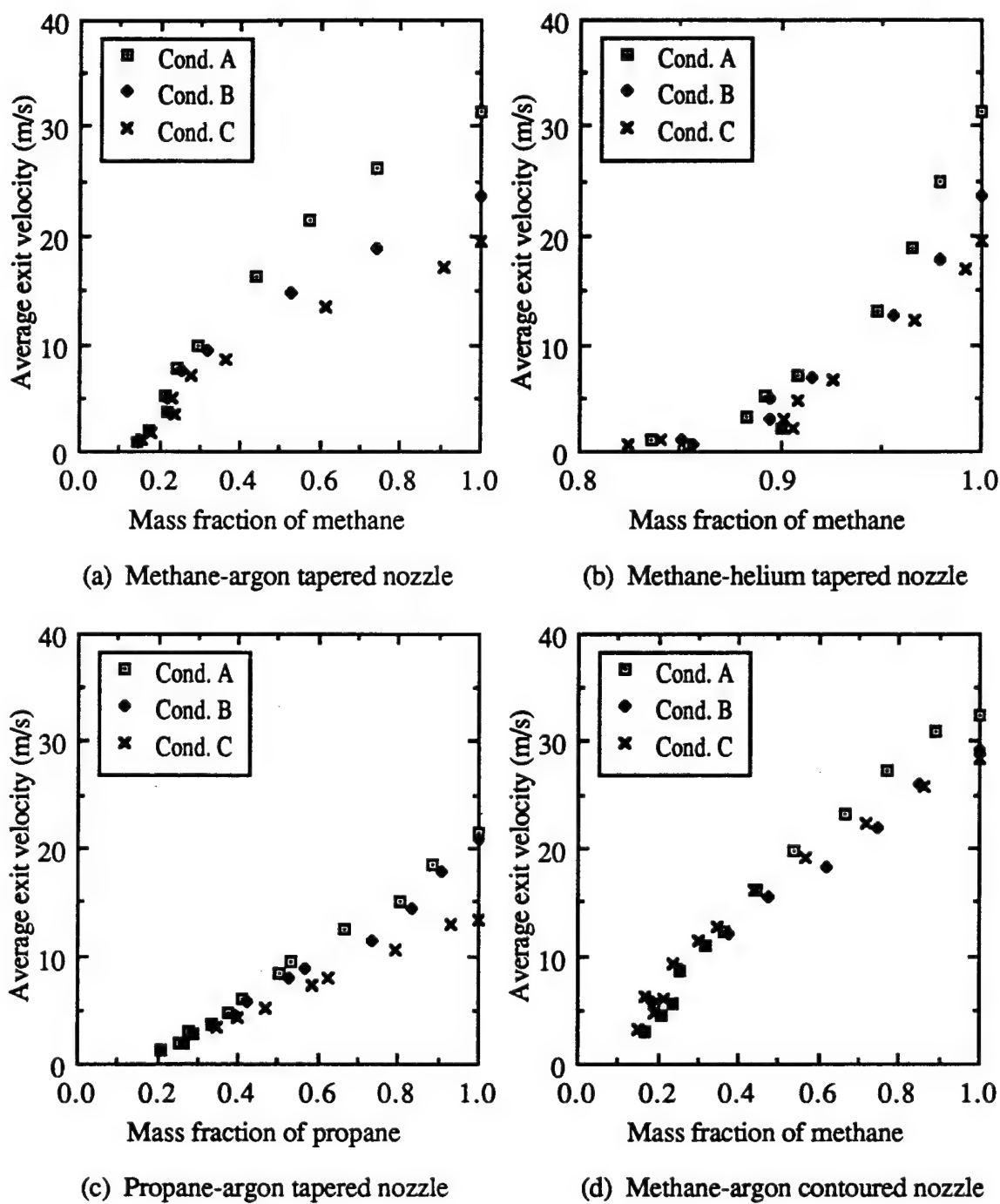


Figure 4.2 Annulus Effects

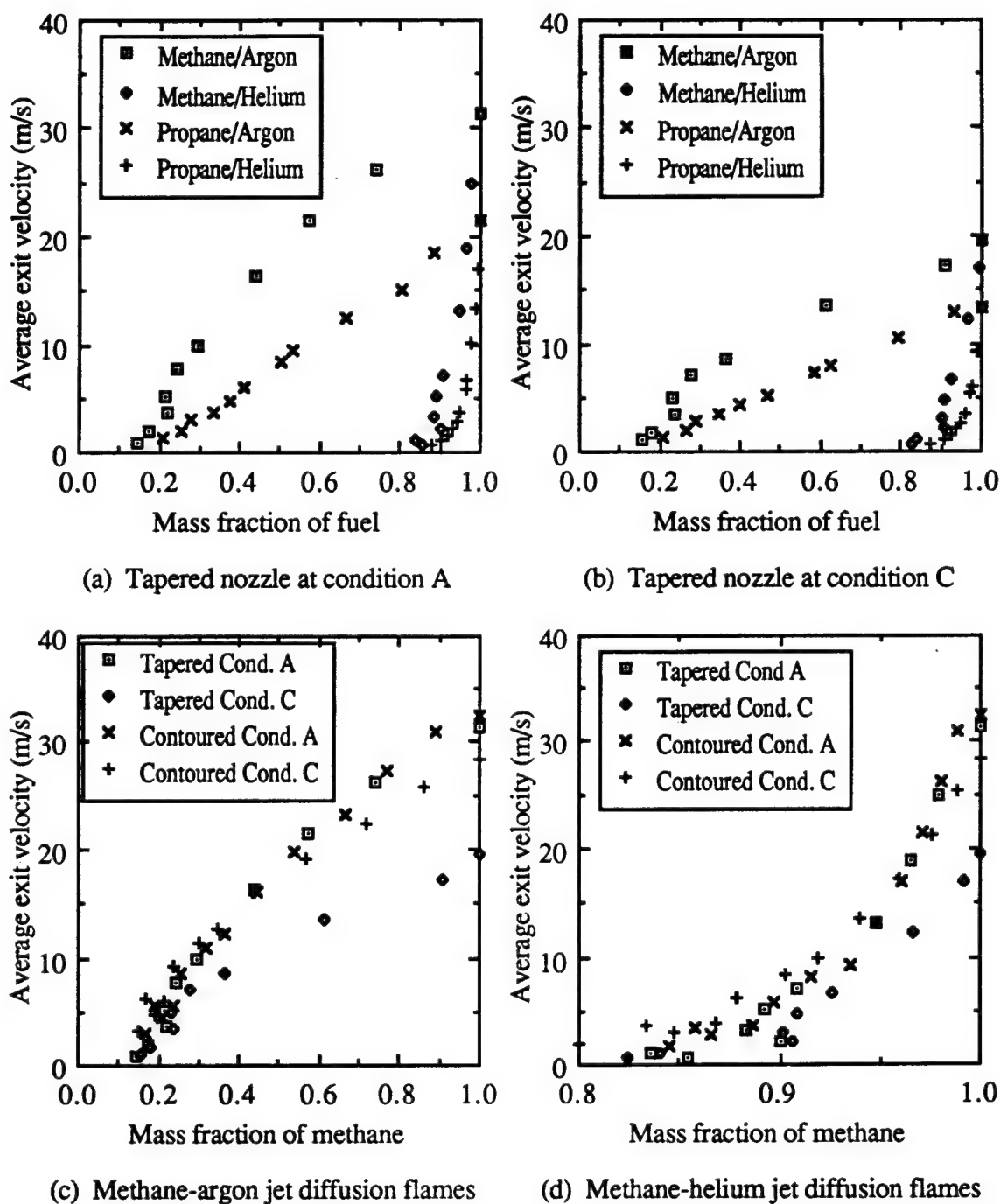


Figure 4.3 Fuel and External Geometry Effects

using the contoured nozzle reveals that at higher dilutions the increased annular velocity stabilizes the jet diffusion flame better than at lower annular flow rates as shown in Figs. 4.3(c), and 4.3(d).

Figures 4.3(a), and 4.3(b) display the difference between the two fuels used, propane and methane. The lift-off velocity as a function of mass fraction of the diluted fuel jet reveals that methane has a higher lift-off velocity, for example, 31.4 m/s for pure methane and 22 m/s for pure propane. The difference in lift-off velocities decreases when the fuel mass fraction decreases when diluted with helium or argon. These trends are indicative of all inerts used.

The dilution of the fuel with argon, nitrogen, and helium results in a lower lift-off velocity, with helium having the most drastic change in the lift-off velocity. The results are summarized in Fig. 4.4. At annular Condition A, the dilution limits of nitrogen and argon-methane mixtures are 0.15 and 0.28, respectively, and that of helium-methane mixture is about 0.85 as shown in Fig. 4.4(a). Below these limits stabilized jet diffusion flames were not established in the experiment. The lift-off velocities ranged from 1.0 to 31.4 m/s. This was observed for both methane and propane mixtures using tapered and contoured nozzles at the annular flow conditions A through C, shown in Figs. 4.4(b) to 4.4(d). These are representative cases of the effects of the three inerts on the methane and propane jet diffusion flames at the different annular conditions.

The dilution results reported here represent the first effort in quantifying stability curves for methane and propane jet diffusion flames (Seaba et al., 1990). A similar work on hydrogen jet diffusion flames was reported by Takahashi et al. (1984) for the same inert gases examined in the present study. A comparison of the present work with that of Takahashi et al. (1984) reveals that argon and nitrogen dilutions have similar trends, but not helium. Helium is the most stable additive among the three examined by Takahashi et

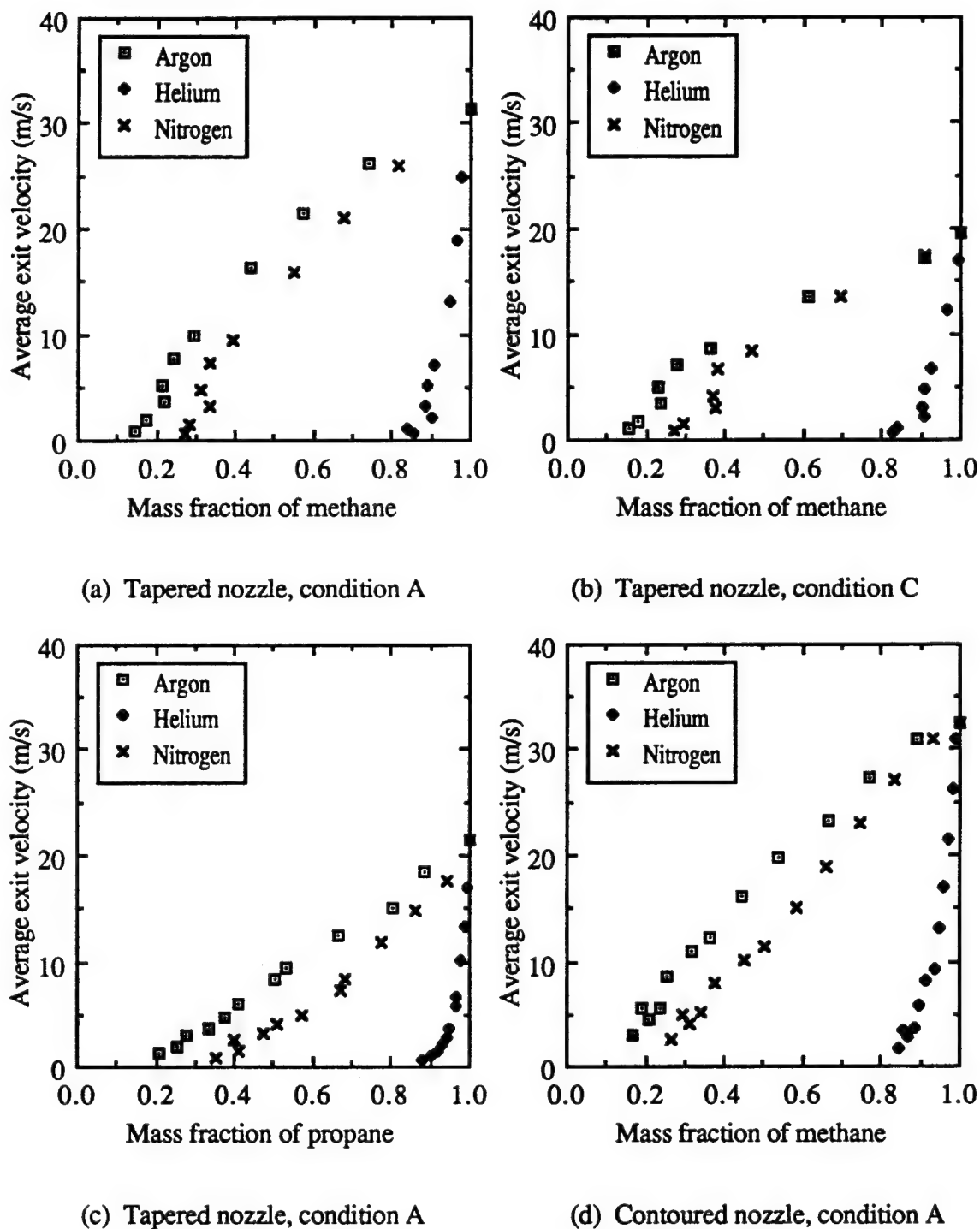


Fig. 4.4 Diluent Effects

al. (1984) for hydrogen jet diffusion flames; however, it is the least stable for methane and propane jet diffusion flames found in the present work.

Takahashi et al. (1984) explained the observations by stating that the laminar flame speed for the helium dilution is greater than that of argon and nitrogen. They measured the velocity at the flame base using LDA. It was concluded that the lift-off was due to the local mixture velocity exceeding the chemical reaction rate of the mixture, thus supporting the premixed flame theory. Laminar flame speeds of methane inert mixtures in a premixed state reveal that helium dilutions have the greatest flame speed, followed by argon and nitrogen (Clingman et al., 1953).

Assuming a premixed methane-inert or propane-inert air mixture at the flame base, the helium dilutions will have a greater laminar flame speed than argon or nitrogen mixtures (Clingman et al., 1953). The laminar flame speed is proportional to the turbulent flame speed (Abdel-Gayed et al., 1987), therefore the premixed flame model would predict the helium dilution to be the most stable inert for methane and propane jet diffusion flames. The present study determined that helium dilutions were the most unstable inert, contradicting the premixed flame model.

The work of Ishizuka and Tsuji (1981) on the extinction of methane-inert mixtures in a counter-flow cylindrical burner arrangement reveals that argon is the most stabilizing additive and helium the least of the inerts studied in their investigation. The extinction of the flame in the experiment studied by Ishizuka and Tsuji (1981) is attributed to high straining rate across the flame. The straining rate defined as the velocity gradient normal to the flame zone. The extinction of the diffusion flame by the high straining is supported by the laminar flamelet model of Peters and Williams (1983).

In the present study of lift-off of methane and propane jet diffusion flames it is important to obtain the axial and radial velocity profiles at the flame base near lift-off. The

velocity profiles obtained using LDA are discussed later (Section 4.3). The profiles will provide the quantitative information to calculate the straining rate at the flame. Also the axial velocity can be compared to the premixed flame model. The flame location is required to compare with the velocity profiles in order to calculate the straining rate at the flame location. The flame location results will be shown in Section 4.2.

4.2 Location of the Flame Zone

Existing theories on the lift-off of jet diffusion flames are concentrated on the quantities near or in the flame zone, thus the flame zone location is required. The flame zone is defined as the location where chemical reaction occurs, forming a high temperature region. The hot (flame) zone location was determined at the near nozzle exit for the diluent conditions used in LDA measurements. Table 4.1 lists the flame locations for the pure methane (Conditions 0, A, B, and C) and dilution conditions 1 and 2. The conditions are defined in Table 4.2. The hot (flame) zone is 1.5 mm wide in the radial direction at the flame base. The radial location of the flame refers to the center of the hot zone relative to the jet center, where the inner radius of the burner exit is 2.34 mm. The two bright spots above the nozzle represent the hot (flame) zone, the cutoff temperature for the SiC filament is 1300 K (Chen and Goss, 1989) as shown in Fig. 4.5. The light streak lines in the vertical direction from the nozzle exit represent the luminous flame zone. The stoichiometric mixture fraction is calculated by the mixture composition at the nozzle exit, the air composition has an oxygen to nitrogen ratio of 1 to 3.76, respectively. Figure 4.5 shows the pure methane flame at a lift-off velocity of 24 m/s at annular Condition B.

All conditions studied maintained a jet Reynolds number greater than 2000, based upon the exit diameter and fuel mixture viscosity. The argon and helium dilutions with the same condition number correspond to nearly the same Reynolds number. The Chapman-Enskog

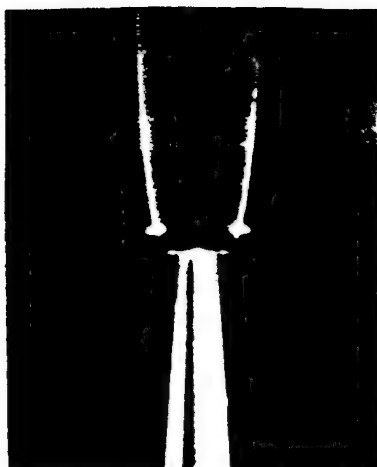


Figure 4.5 Flame Zone

relation was used to calculate the dynamic mixture viscosity at 298 K which was used to calculate the Reynolds number. The jet exit velocities of methane-argon Condition 1 and methane-helium Condition 2, and pure methane (Condition 0) and methane-helium Condition 1 are similar.

Table 4.1 Flame Location of Methane and Methane Diluted Jet Diffusion Flames

Fuel/Inert	Cond.	Flame height above burner exit (mm)	Radial distance of flame from jet center (mm) (r/R)		Mixture fraction
Methane	A	1.3	3.3	1.41	0.0551
Methane	B	1.2	3.4	1.47	0.0551
Methane	C	0.9	3.4	1.47	0.0551
Methane	0	1.0	3.4	1.47	0.0551
Methane/Argon	1	1.4	3.5	1.50	0.0651
Methane/Argon	2	1.6	3.6	1.54	0.0840
Methane/Helium	1	1.0	3.6	1.54	0.0555
Methane/Helium	2	1.2	3.7	1.58	0.0566

Table 4.2 Diluent Conditions for LDA Measurements

Fuel/Inert	Cond.	Mole fraction of fuel	Mass fraction of fuel	Re	Avg. Exit Vel (m/s)
Methane	0	1.00	1.00	4387	22.0
Methane/Argon	1	0.81	0.64	4313	15.7
Methane/Argon	2	0.53	0.31	2429	7.7
Methane/Helium	1	0.97	0.99	3982	20.2
Methane/Helium	2	0.89	0.97	2718	14.3

The flame prior to lift has a nonluminous gap between the nozzle exit and the flame base (1.0 to 1.6 mm), the gap was first observed by Wohl et al. (1949). More recently, Chen and Goss (1989) measured the gap between the flame base and the nozzle exit plane, prior to lift-off (5 mm diameter, 30 m/s jet velocity) to be approximately 1.5 mm for a methane jet diffusion flame at annulus Condition B using thin-filament pyrometry (TFP). The radial location of the flame zone (1.47 to 1.58 r/R , R is the burner exit inner radius) indicates that the flame is outside the shear layer (0.95 to 1.05 r/R), in the annular region of the burner. This observation agrees with Chen and Goss (1989) who determined the radial flame location at the flame base to be 1.57 r/R , for methane jet diffusion flames, employing the TFP technique.

The mixture fraction, which is defined as the effective mass fraction of the fuel in the mixture, listed in Table 4.1 indicates the stoichiometry of the fuel-inert-air mixture, pure fuel has a mixture fraction of 1, and oxidant-inert has a mixture fraction of 0. The stoichiometric mixture fraction has an implication on the location of the flame zone. For jet diffusion flames, as the mixture fraction increases, the radial position of the flame should decrease if other physical quantities are held constant. The mixture fraction of argon dilutions is greater than the helium dilutions, which agrees with the experimental results that indicate the argon diluted hot (flame) zone is located closer to the jet centerline than helium diluted jet diffusion flames. For the same diluent, the hot (flame) zone location is seen to move radially outward as the mixture fraction is increased at near lift-off conditions. This may be due to the added time for the fuel to diffuse radially outward due to a lower lift-off velocity.

4.3 LDA Measurements

4.3.1 LDA Experimental Conditions

LDA data were taken to characterize the flow field near the nozzle exit plane across the jet and annular regions. Annular velocities of 0.07, 0.15, and 0.30 m/s (Conditions A, B, and C, cf. Table 2.1) with pure methane, and methane diluted by argon or helium (Table 4.2) at annular velocity 0.15 m/s (Condition B) were studied. A tapered nozzle was the only burner tube used for LDA measurements. The jet and annulus were conditionally sampled, i.e. either the jet or the annular air is seeded, for all the data presented. The data was filtered to 2 standard deviations from the mean. A Gaussian distribution was observed at all measurement locations. The argon and helium dilutions selected are identified in Fig. 4.6.

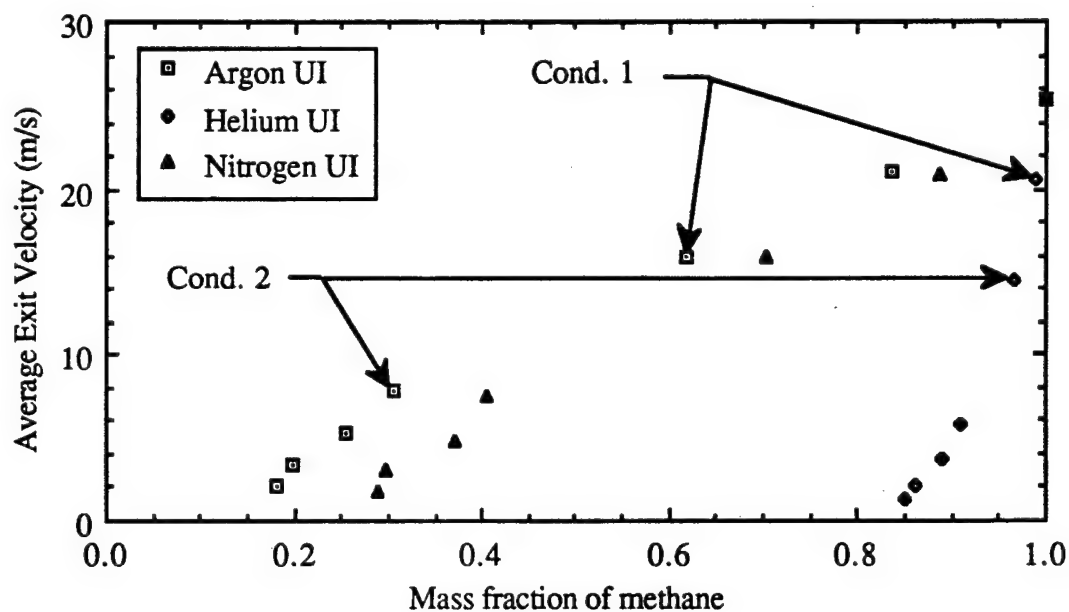


Figure 4.6 LDA Test Conditions

4.3.2 Jet and Annulus Conditions

4.3.2.1 Cold Flow

The velocity distributions in a cold jet are used to characterize the jet and annular regions and provide a base case to analyze the effects of the flame on the flow field. The mean and rms velocity distributions of an argon jet (at $x/d = 0.4$ from the burner exit) are shown in Figs. 4.7, 4.8, and 4.9. An argon jet at Condition B is presented with the mean and rms velocity profiles normalized by the maximum exit velocity (U_c). The maximum mean axial jet velocity of the argon jet was 19.8 m/s, corresponding to a Reynolds number of 6500. The radial distances from the jet center were normalized by the inner radius (R) of the nozzle exit. In the discussion herein, "Jet data" refers to the velocity measurements of the seeded jet, and "annulus data" refers to the velocity measurements of the seeded annulus.

The jet has a flat velocity profile with a jet half width of $0.98 r/R$. The half width is defined as the location where the local mean velocity is half the maximum mean velocity. The turbulence intensity (U_{rms}/U_c) of the jet at location $0 \leq r/R \leq 0.6$ is about 1%. The maximum axial rms velocity occurs at $0.98 r/R$. The shear layer in the near field of the jet is very thin compared to the exit diameter extending from $r/R = 0.8$ to $r/R = 1.0$. The shear layer is defined as U_{rms}/U_c greater than 3%.

The mean jet radial velocity is zero at the jet center and the fluid is moving radially inward to the jet center due to the tapered nozzle geometry. However, measurements at $x/d = 6$ and the radial range of $0 \leq r/R < 4$, show that the mean radial component is moving radially outward as shown by Fig. 4.10. The radial velocity has a maximum inward velocity at $r/R = 0.95$.

The annular region, defined as $r/R > 1$, maintains a flat mean axial velocity profile for $r/R > 5$, with low axial rms values of 0.02 m/s. The turbulence intensity U_{rms}/U_m , in the

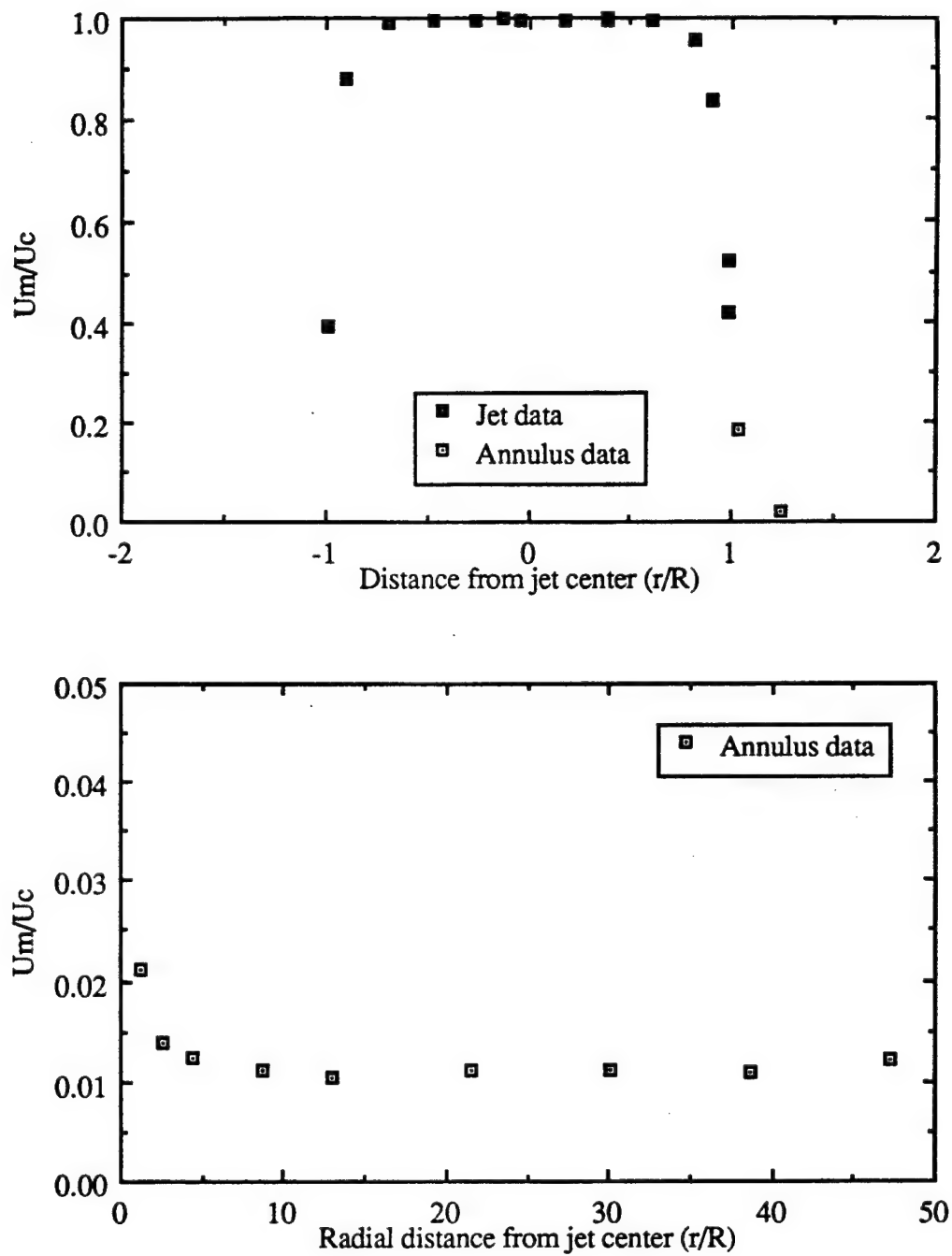


Figure 4.7 Mean Axial Velocity Distribution in an Argon Jet at $x/d = 0.4$

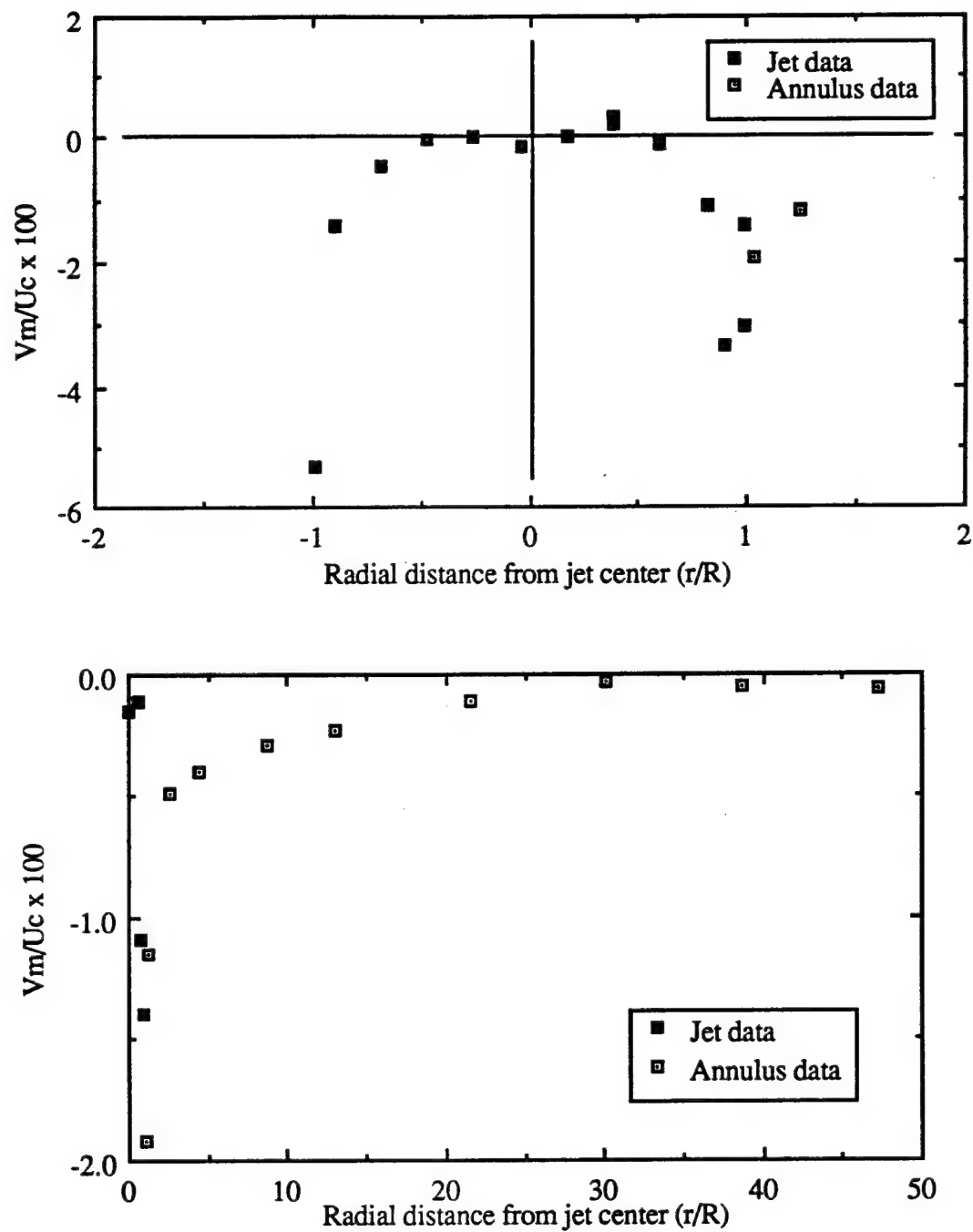


Figure 4.8 Mean Radial Velocity Distribution in an Argon Jet at $x/d = 0.4$

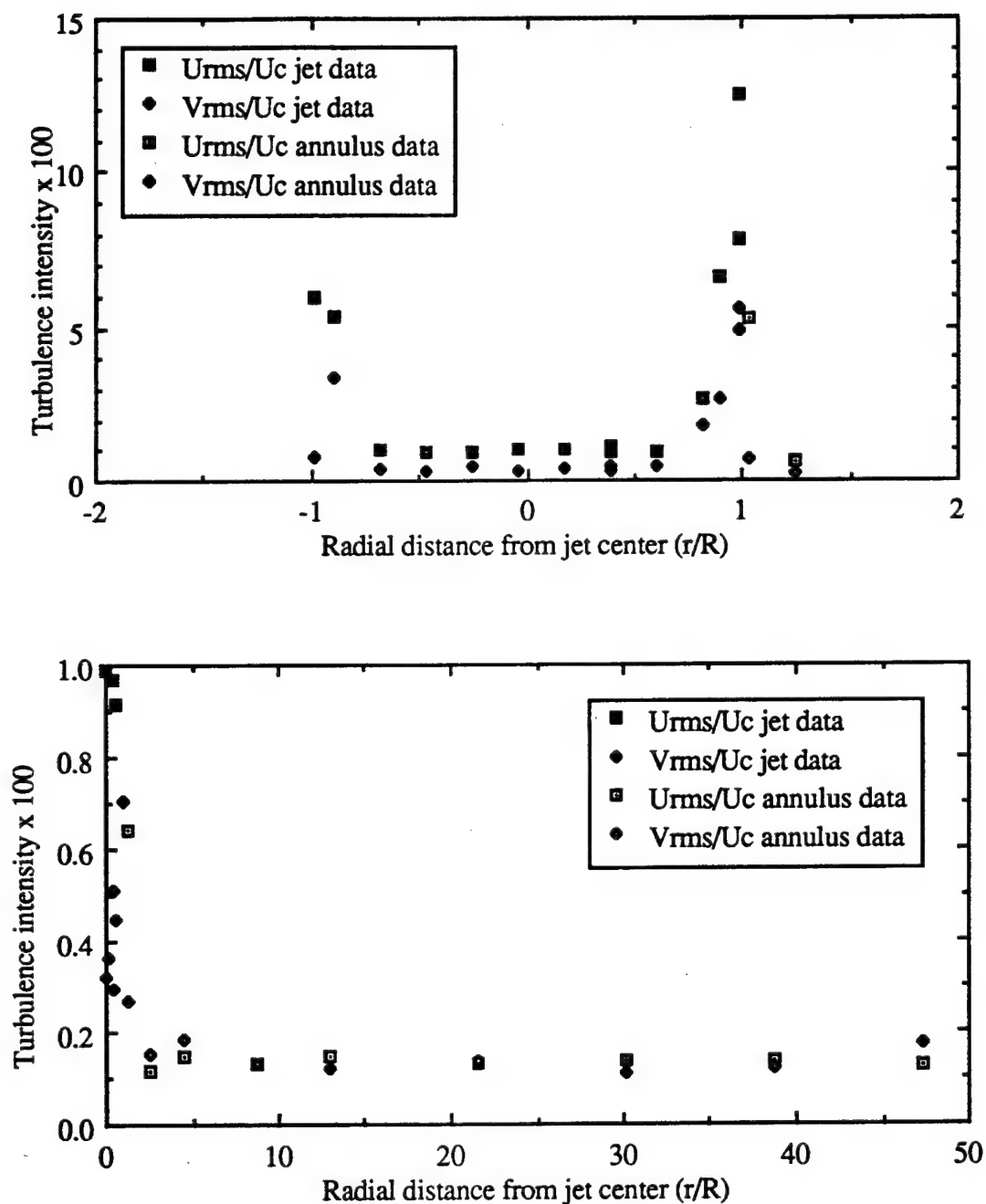


Figure 4.9 Turbulence Intensity Profiles in an Argon Jet at $x/d = 0.4$

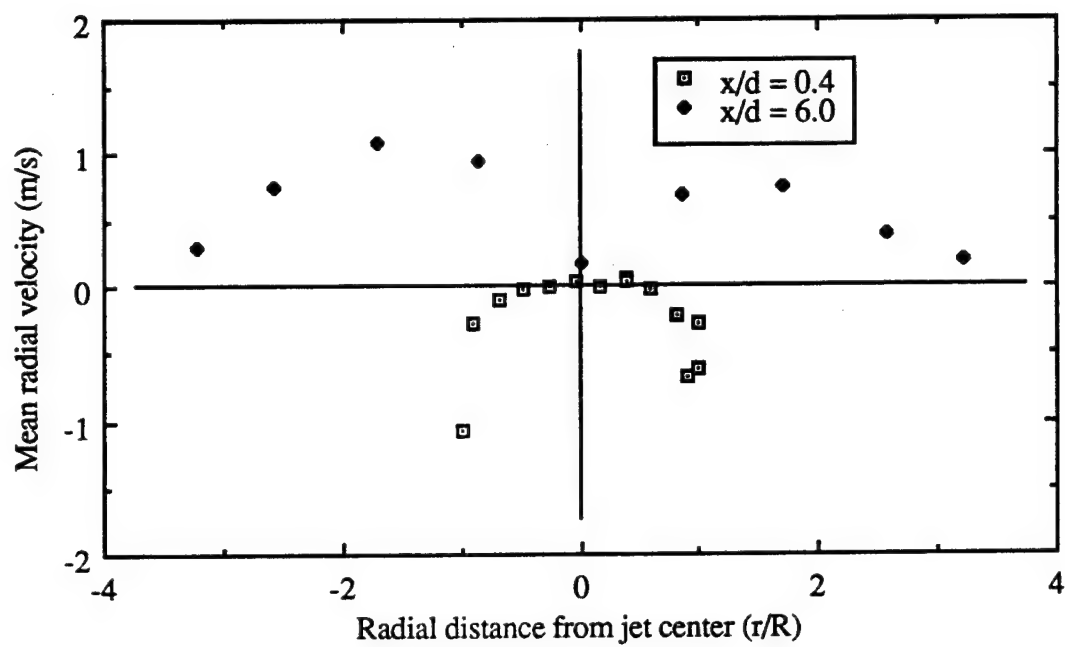


Figure 4.10 Radial Profile in an Argon Jet at Two Axial Locations

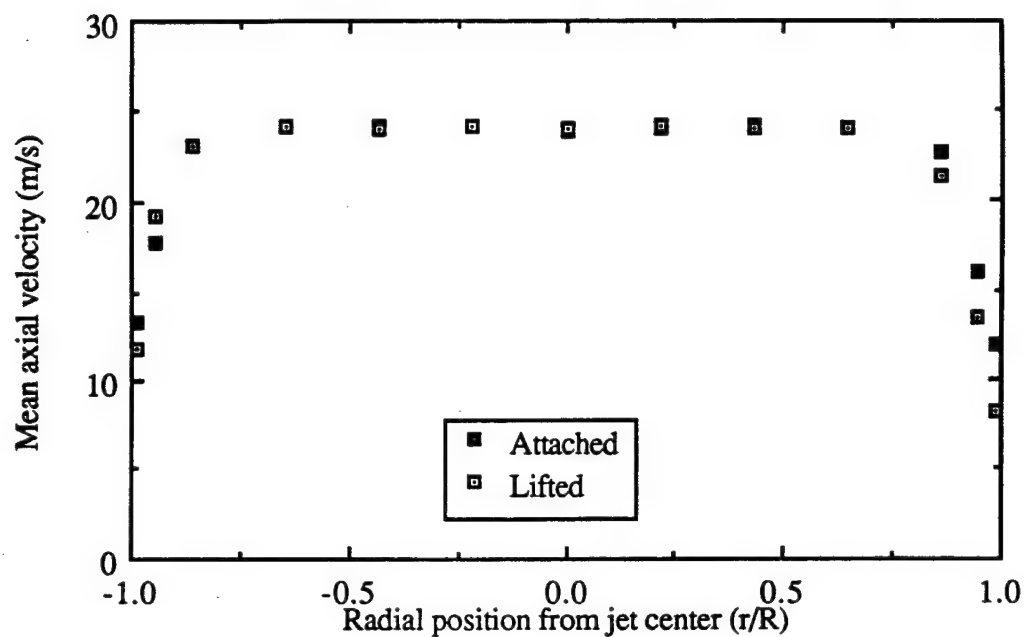
annular flow is about 10%. However, the magnitude of the rms velocity compared to the maximum jet velocity is about 0.2%. The mean and rms velocities of the annular air increase near the jet shear layer at $r/R = 1$. The annular mean and rms velocity data indicate that the maximum mean radial velocity is located in the shear layer at $r/R = 1$. The radial mean and rms velocity values are nearly zero in the region outside the shear layer.

The annulus and jet data stop at approximately $r/R = 1$, where the locations mark the convective transport of the jet and ambient fluids, respectively. The overlap regime, $0.98 \leq r/R \leq 1.0$, represents the radial location where the two streams are convectively mixing. Thus the data suggests that beyond the convective mixing, the transport of the fuel jet fluid is primarily due to diffusion of the fuel jet fluid to the reaction, or the flame zone.

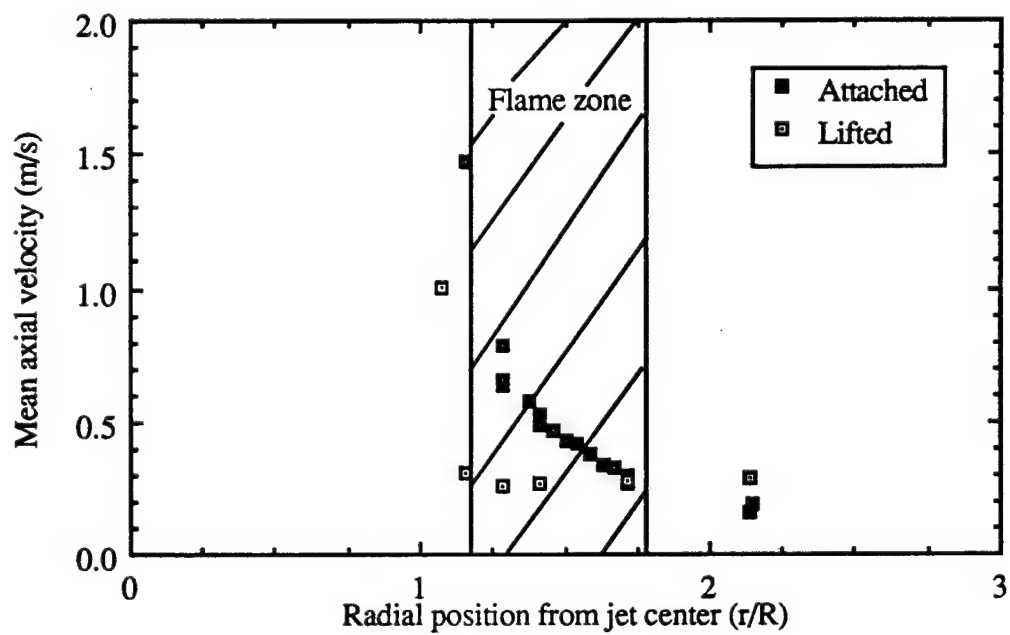
4.3.2.2 Attached and Lifted Methane Jet Diffusion Flames

The attached and lifted jet velocity profiles provide information on the effects of the flame on the near-field of the jet. The same jet and annular flow rates are set for both attached and lifted flame data. The methane jet exit velocity is 22.03 m/s corresponding to a Reynolds number of 4387. The velocity measurements are presented in dimensional form (m/s) in order to compare the magnitudes of the data. In this section jet data (seeded jet) are represented by part (a) and the annulus data (seeded annulus) by part (b).

There is little difference between the seeded jet mean axial velocity profiles of the lifted and attached jet diffusion flames as shown in Fig. 4.11. The jet data of part (a) is similar to the cold jet data previously discussed. The major difference between the attached and lifted conditions are shown by the annulus data (part b). The differences occur in the hot (flame) zone where r/R is between 1 and 2. The mean axial velocity profile assumes a larger velocity gradient for the lifted flame as compared to the attached flame, as shown in Fig. 4.11(b).

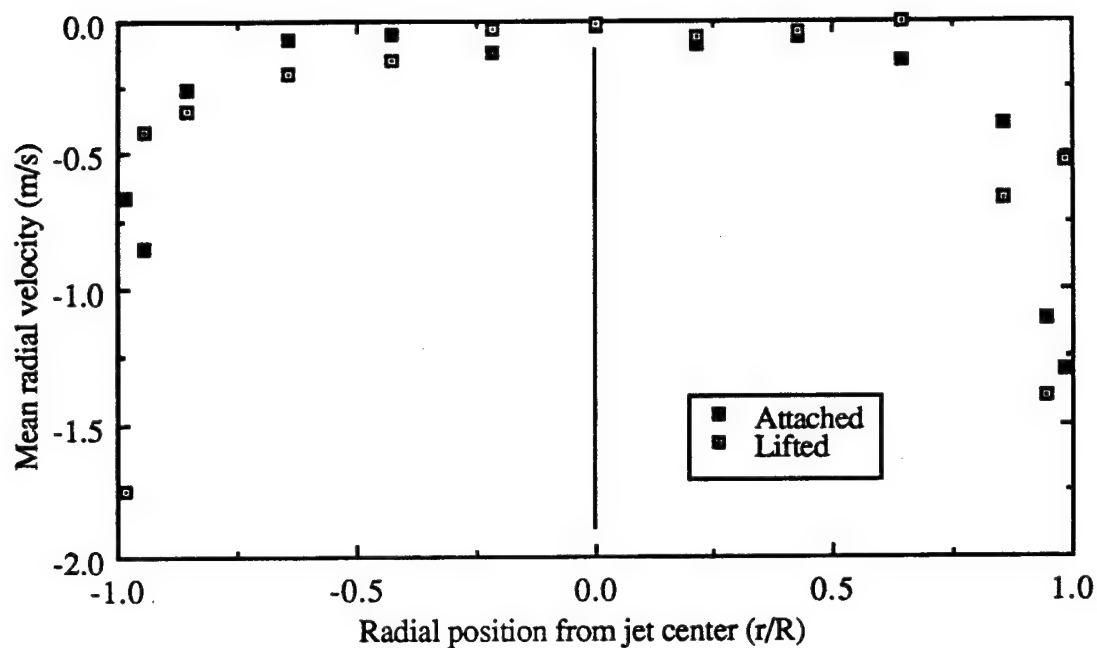


(a) Seeded jet fluid

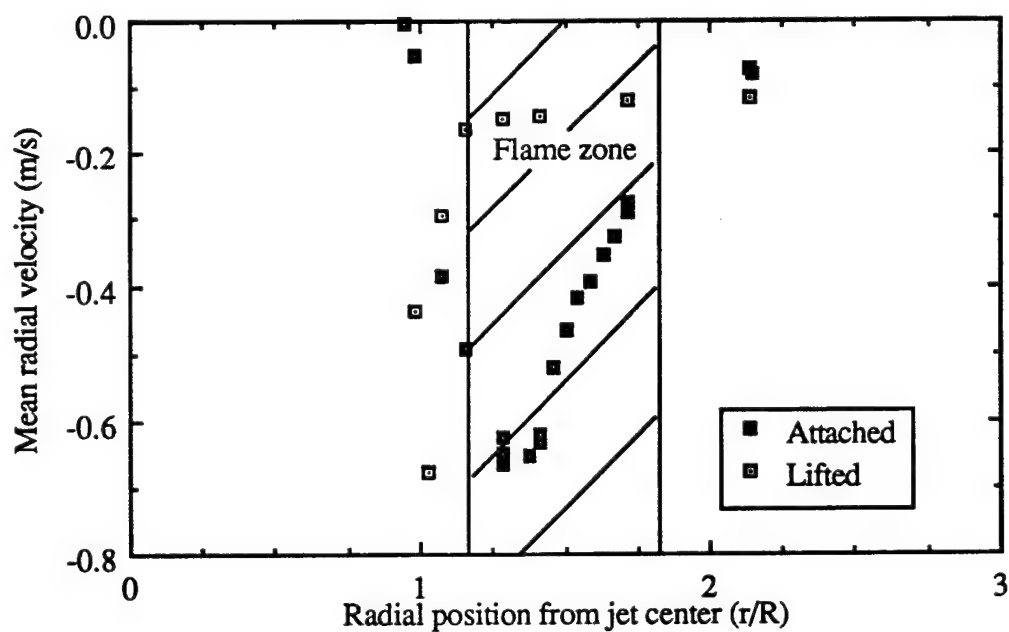


(b) Seeded annular air

Figure 4.11 Axial Profile in Lifted and Attached Methane Jet Diffusion Flames at $x/d = 0.4$



(a) Seeded jet fluid



(b) Seeded annular air

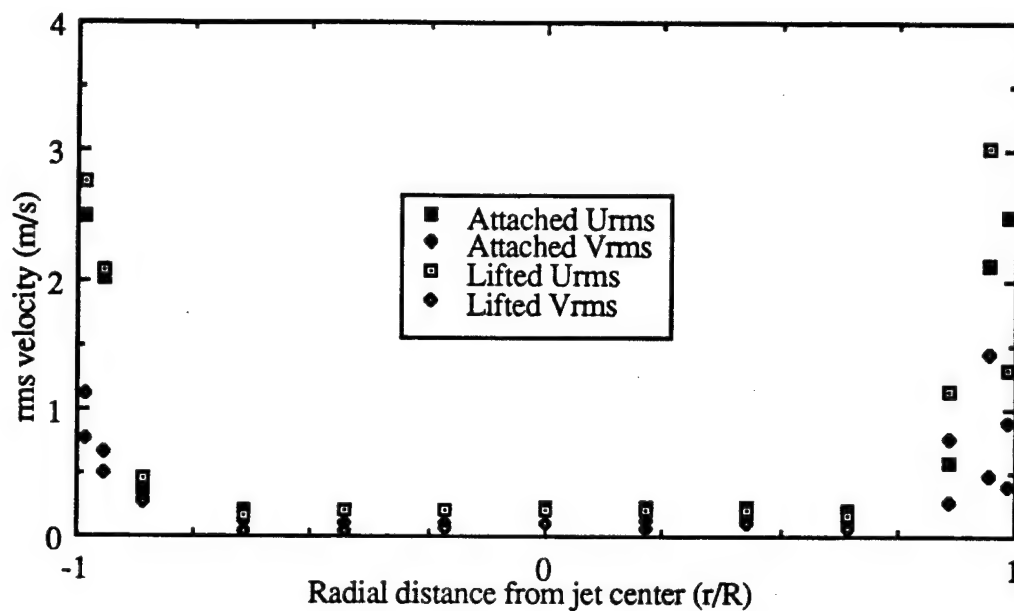
Figure 4.12 Radial Velocity Profile in Attached and Lifted Methane Jet Diffusion Flames at $x/d = 0.4$

Figure 4.12 displays the radial velocity profiles. The seeded jet mean radial velocity is zero at the jet center-line and maximum (0.7 m/s inward) at $r/R = 0.90$. The mean radial velocity profiles of lifted and attached jet diffusion flames are qualitatively similar in the jet regime. The most notable difference between the lifted and attached conditions is shown by the annular radial velocity profile. The lifted flame has the maximum inward radial velocity in the jet shear layer at $r/R = 1$, similar to that of the cold jet. However, the attached flame has the maximum inward radial velocity at $r/R = 1.25$. The hot (flame) zone is centered at approximately $r/R = 1.5$ with a thickness of 1.5 mm (or 0.6 R). Conversely, the maximum inward radial velocity occurs between the jet shear layer and the center of the flame zone. It is also observed that the radial component of the attached flame goes to zero near the shear layer, while the lifted flame goes toward its maximum of 0.7 m/s.

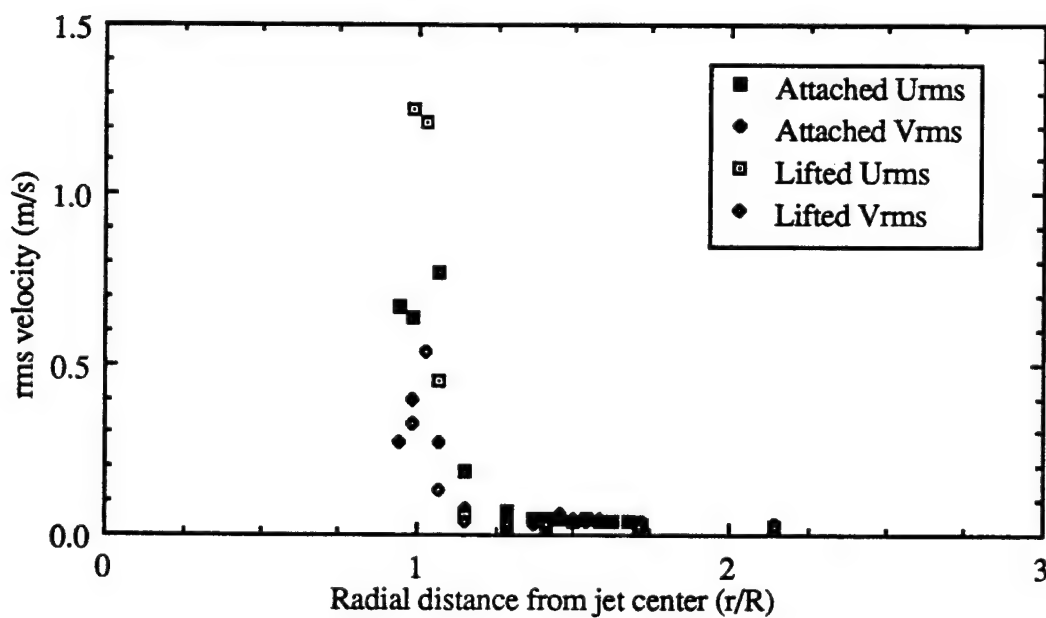
The rms velocity profiles of the jet and annulus are similar for the attached and lifted conditions. The magnitudes of the rms velocities and the turbulence intensities are nearly equal as shown in Fig. 4.13 and Fig. 4.14. The lifted flame has a slightly higher turbulence intensity in the shear layer. In the flame zone, the attached and lifted intensities are nearly equal as shown in Fig. 4.14. It is generally accepted that the flame exhibits laminarization effects, lowering the turbulence intensities at the flame location. This, however, is not obvious from the conditionally sampled data at the flame base of a methane jet diffusion flame near the lift-off condition.

4.3.3 WRDC and UI Comparison

The literature review indicates that the lift-off velocity varies over a wide range, with several parameters affecting the lift-off process. Duplication of lift-off experiments at different test locations shows that the process can be facility independent. Figures 4.15 and 4.16 summarize the comparison of the mean axial and radial velocity profiles

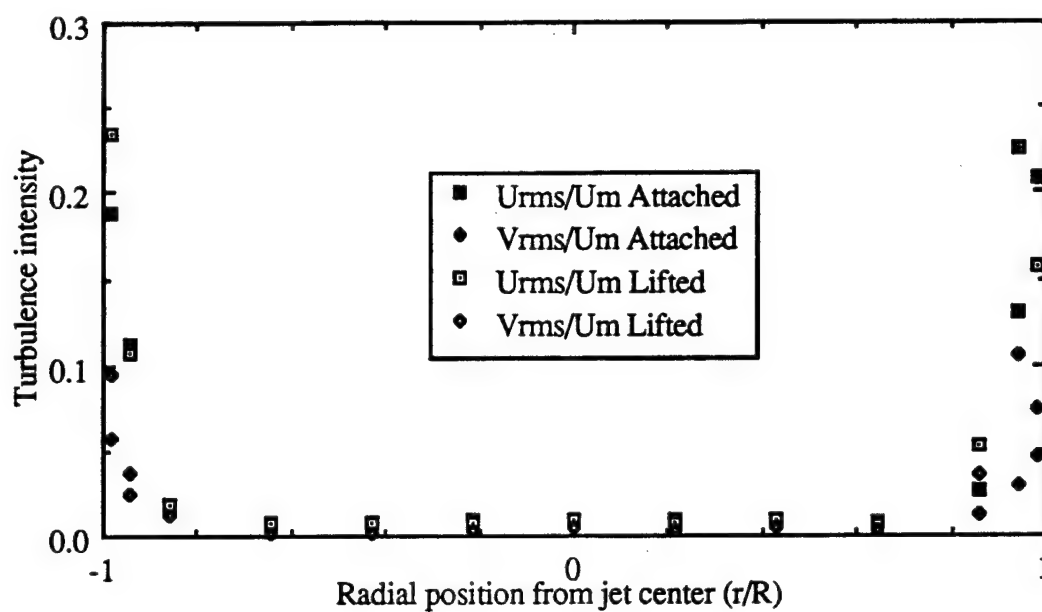


(a) Seeded jet fluid

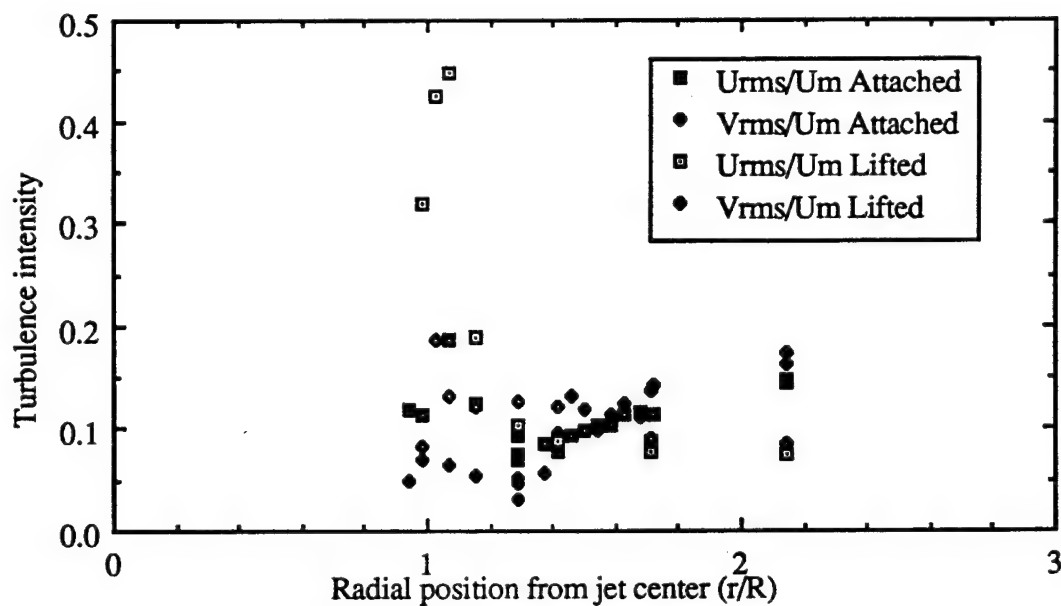


(b) Seeded annular air

Figure 4.13 RMS Profile in Lifted and Attached Methane Jet Diffusion Flames at $x/d = 0.4$



(a) Seeded jet fluid



(b) Seeded annular air

Figure 4.14 Turbulence Intensity Profile in Attached and Lifted Methane Jet Diffusion Flames at $x/d = 0.4$

conducted at WRDC and UI. Since different diameter nozzles were used (5.08 mm at WRDC, and 4.67 mm at UI) the radial distance is nondimensionalized relative to its respective inner radius. The flame was attached to the burner exit and the annulus was set at Condition B for the data presented in this section.

The axial velocity at the lift-off which is determined at WRDC is greater than that determined at UI. The axial velocity profiles, however, are similar. A discrepancy is observed in the mean radial velocity profile near the burner rim concerning the seeded jet data. Near $r/R = 1$ the UI mean radial velocity jet data goes toward its maximum, while the WRDC stays close to zero, cf. Fig. 4.16. A possible explanation for this result is that the measurement volume of the LDA system at WRDC was closer to the nozzle exit than the system used at UI, 0.9 mm compared to 1.8 mm from the nozzle exit. Thus, the jet at the downstream location had more time to develop, responding to the entrained annular air. The discrepancies observed may be due to the change in measurement volume locations. The maximum radial velocity is at the same location for both burners, and the magnitudes are within 5 percent, e.g. cf. Fig. 4.16. The design of the combustor at UI was to minimize the rms velocities in the annulus region. The rms velocities for the UI combustor in the outer annulus ($r/R > 2$) were approximately 0.02 m/s, the velocities of the WRDC combustor were about 0.07 m/s. The rms velocity profiles are shown in Fig. 4.17 and Fig. 4.18.

4.3.4 Annular Effects

The premixed flame model is analyzed by the axial velocity measurements. The axial velocity measurements represent the unburnt mixture velocity prior to the flame zone. The

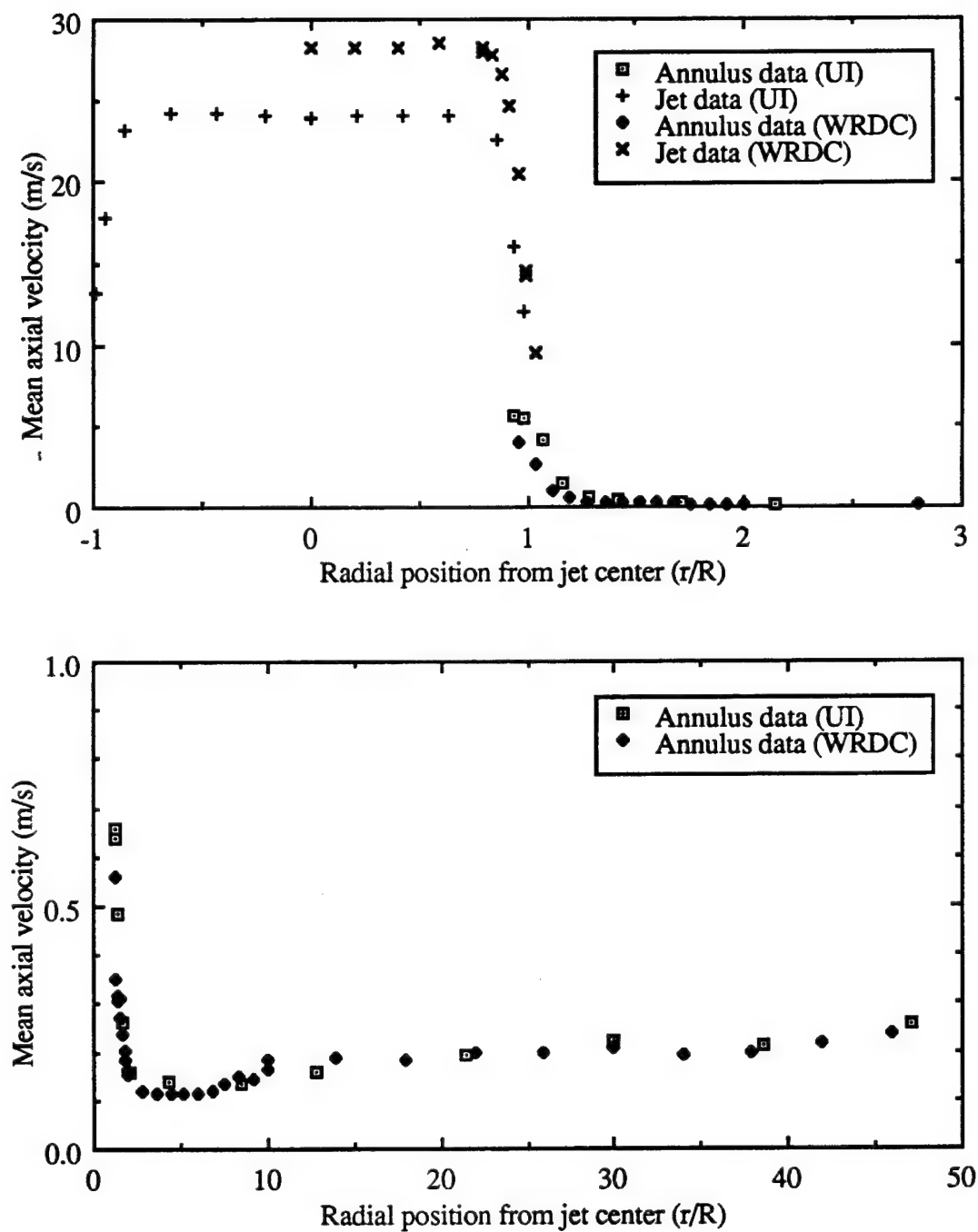


Figure 4.15 Mean Axial Velocity Profile in WRDC and UI Attached Methane Jet Diffusion Flames

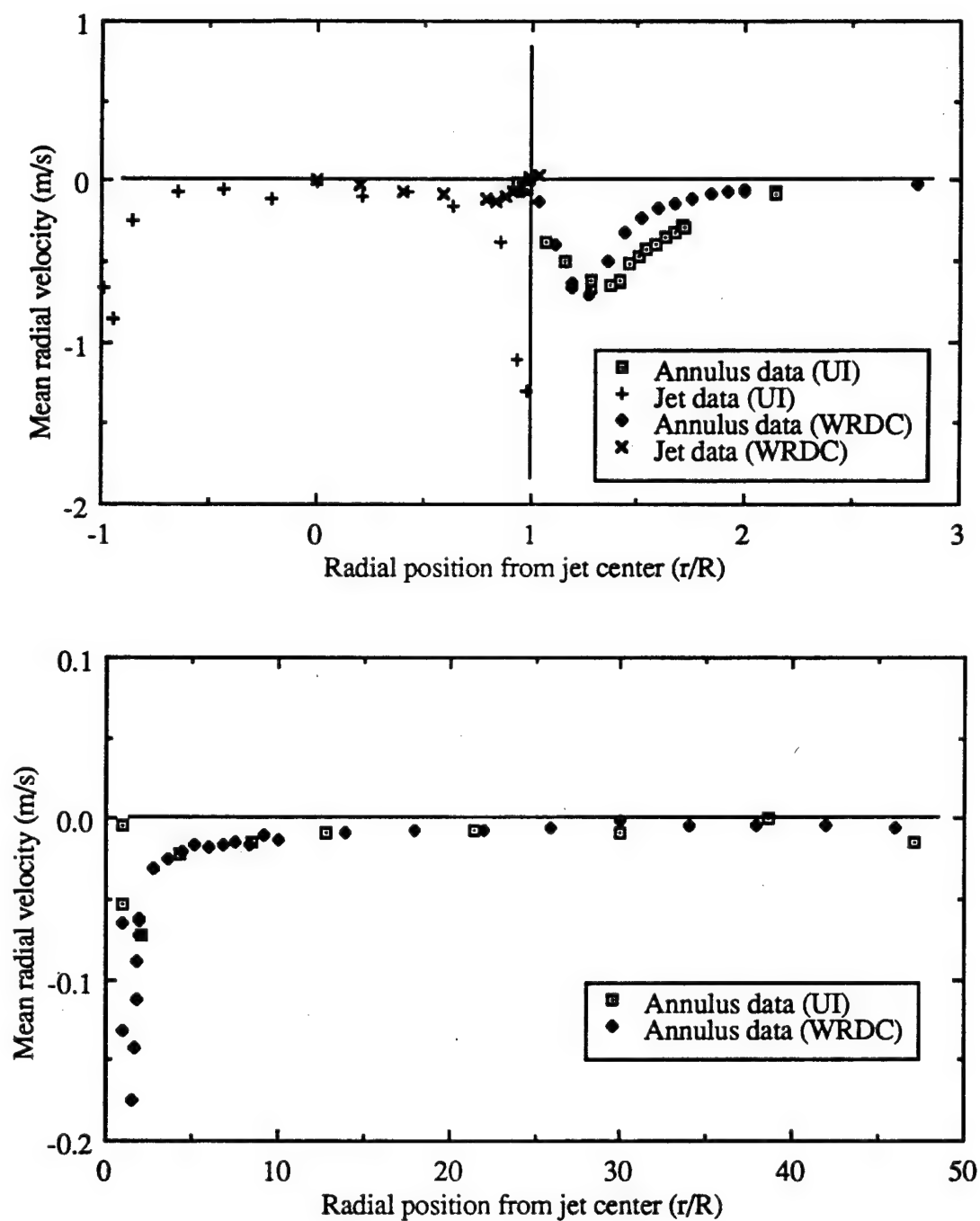


Figure 4.16 Mean Radial Velocity Profile in WRDC and UI Attached Methane Jet Diffusion Flames

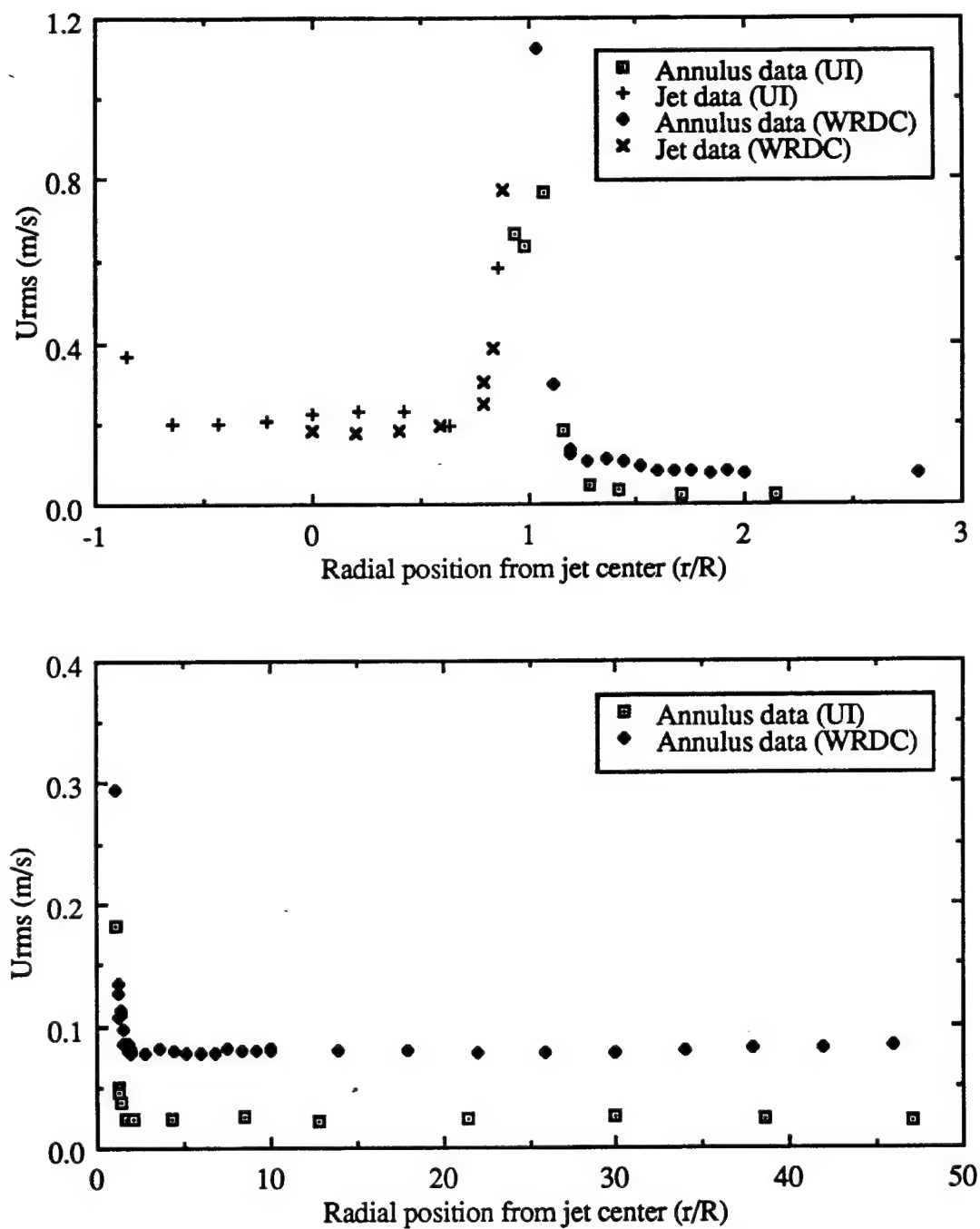


Figure 4.17 Axial Velocity Fluctuation Profile in WRDC and UI Attached Methane Jet Diffusion Flames

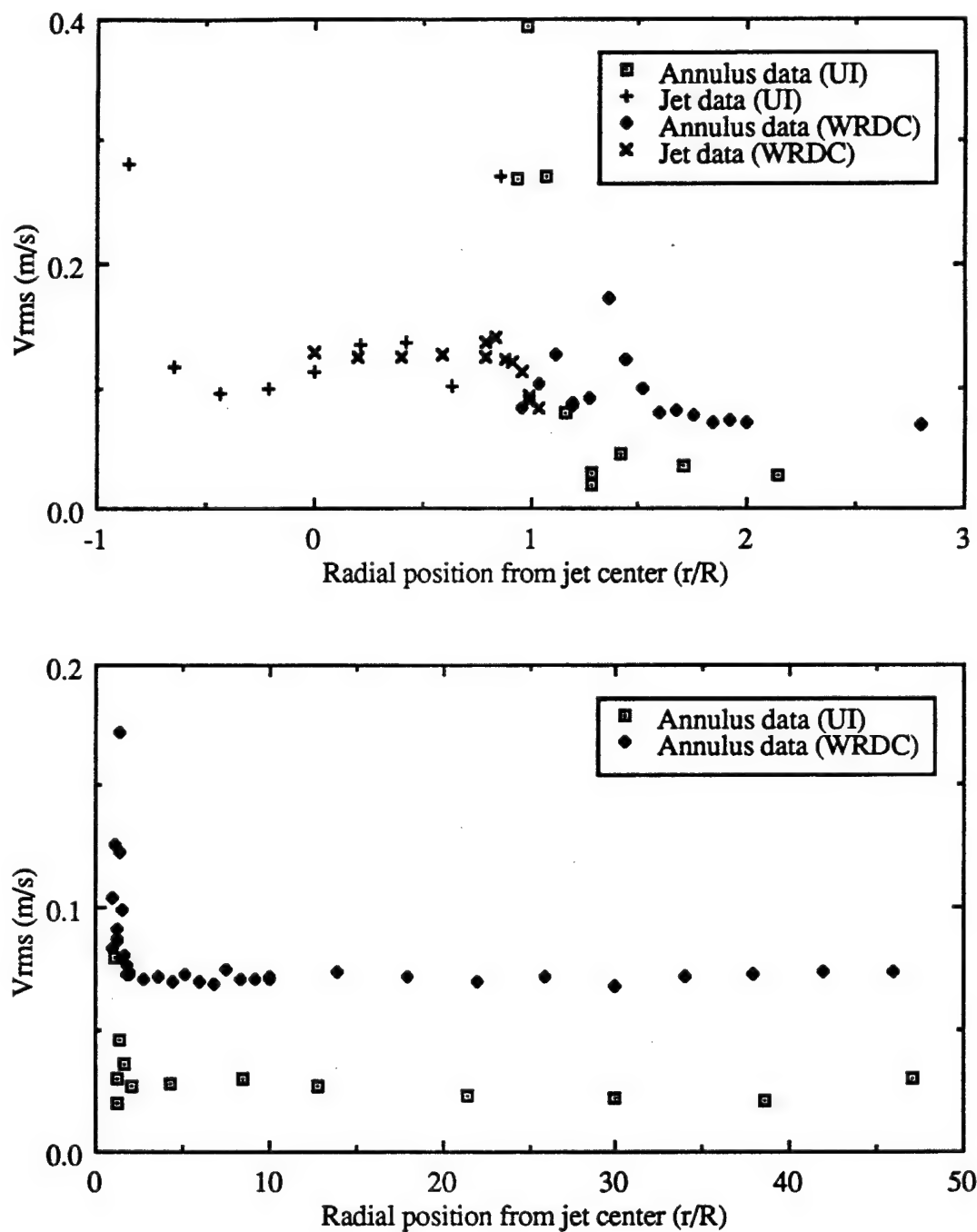


Figure 4.18 Radial Velocity Fluctuation Profile in WRDC and UI Attached Methane Jet Diffusion Flames

premixed flame theory predicts that the axial velocities measured underneath the flame base are nearly the same for all three annular flow conditions.

For the annulus data taken at WRDC as shown in Fig. 4.19, the LDA measurement volume was positioned less than 1 mm above the nozzle exit. The base of the methane jet diffusion flame near lift-off is at approximately 1.5 mm above the burner exit. Therefore, at the radial position of the flame location ($1.3 < r/R < 1.8$), the velocity data represent the velocity of the unburnt mixture prior to the flame zone. Dimensional units are used to quantify the actual velocities near the flame zone. A tapered nozzle was used for all conditions presented in this section.

The annulus data at $1 \leq r/R \leq 2$ represent the velocity of the annular air near the flame zone. Figure 4.19 shows the mean axial and radial velocities near the lift-off for all annular conditions. Condition C has the greatest local mean axial velocities at all radial locations for $1 \leq r/R \leq 2$, while Condition A has the lowest. This corresponds to the flow rates of each condition, Condition C the highest, Condition A the lowest. The mean axial velocities vary 100 percent in the flame zone near lift-off.

The mean axial velocity near the lift-off exceeding the flame speed has been identified to as a cause for the lift-off of hydrogen jet diffusion flames (Takahashi et al., 1984). For the methane jet diffusion flame studied, following the same reasoning, the lift-off would occur when the mean axial velocity at the flame base reached a specific lift-off velocity. Since pure methane was studied, the mean axial velocity at the flame base at each annular condition would be nearly the same. Since the (hot) flame zone was not measured at WRDC, an estimate is derived from the hot zone locations taken at UI. The analysis presented in Section 4.3.5 shows that a good approximation of the flame zone for the different annular conditions would be $1.3 \leq r/R \leq 1.5$. Comparing the estimated flame location ($1.3 \leq r/R \leq 1.5$) with the mean axial velocity profiles, it is seen that the mean axial

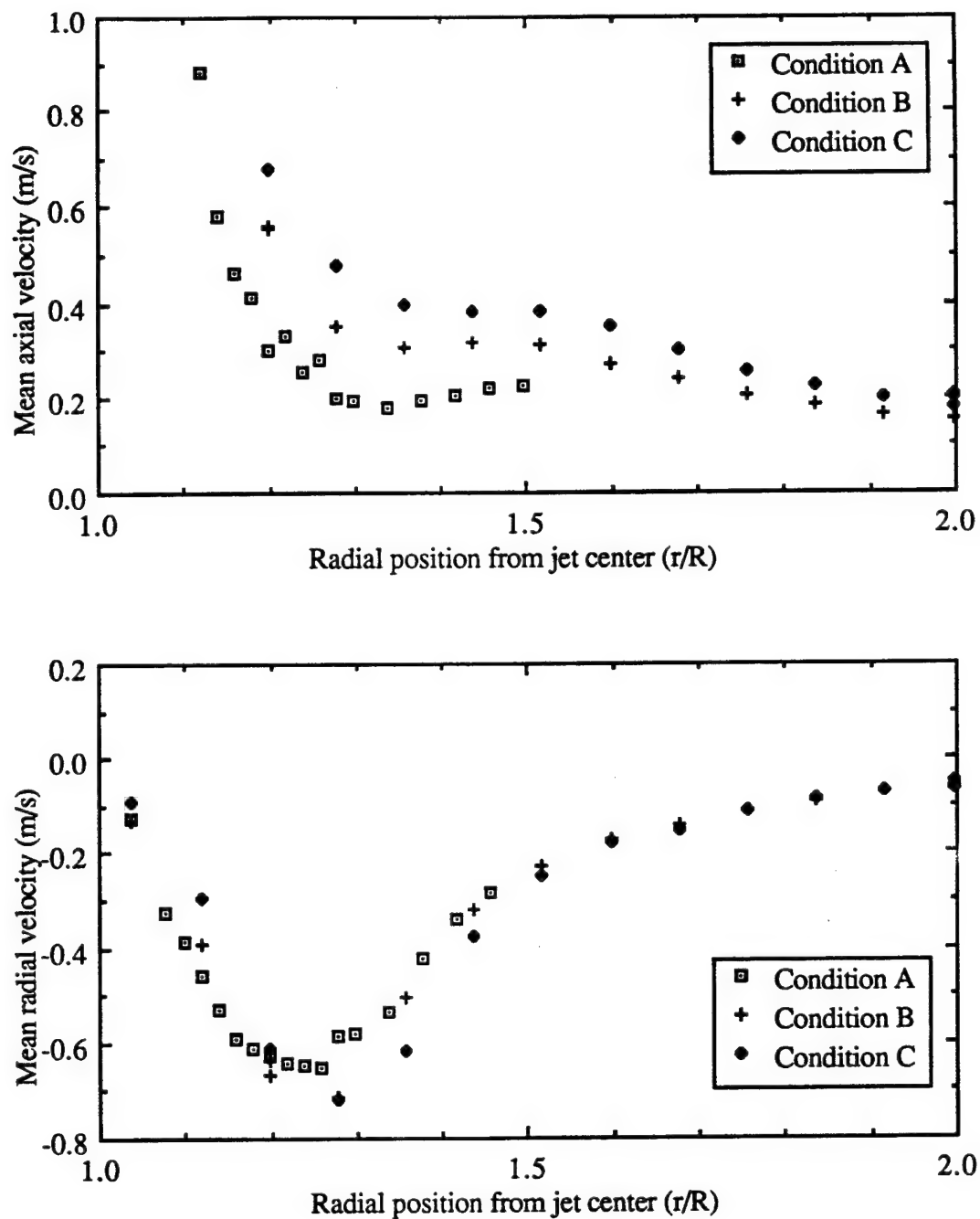


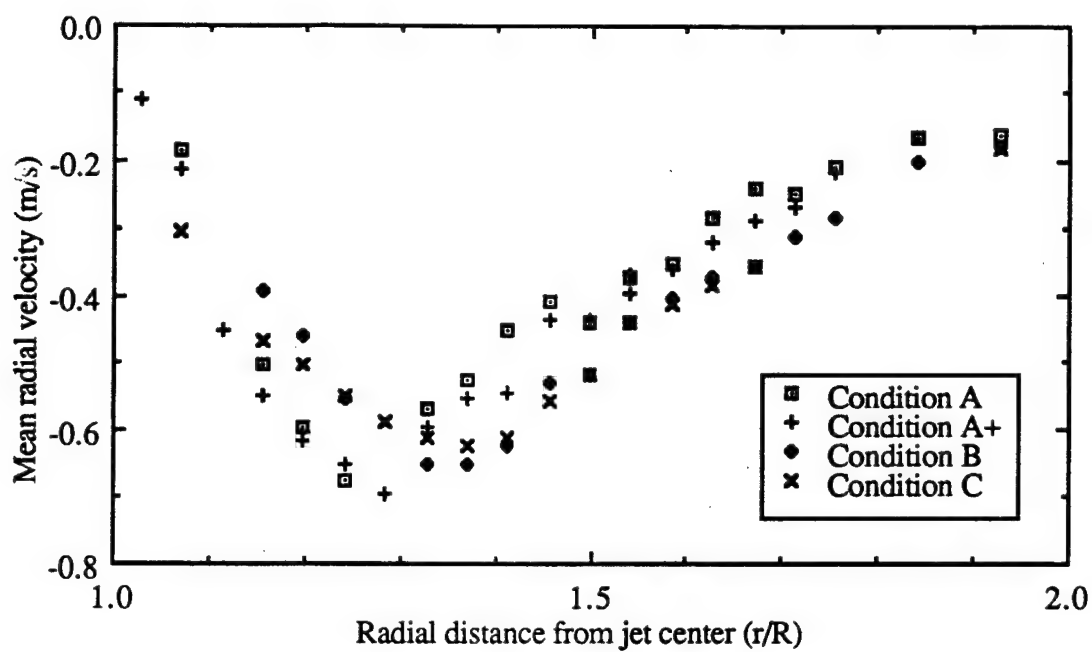
Figure 4.19 Mean Velocity Profiles of Annular Conditions

velocities are not nearly the same but vary as much as 100% between Conditions A and C. Therefore, the convective velocity of the unburnt mixture prior to the flame zone is not a good parameter to use in predicting the lift-off of methane jet diffusion flames, suggesting the failure of the premixed flame theory in the present study.

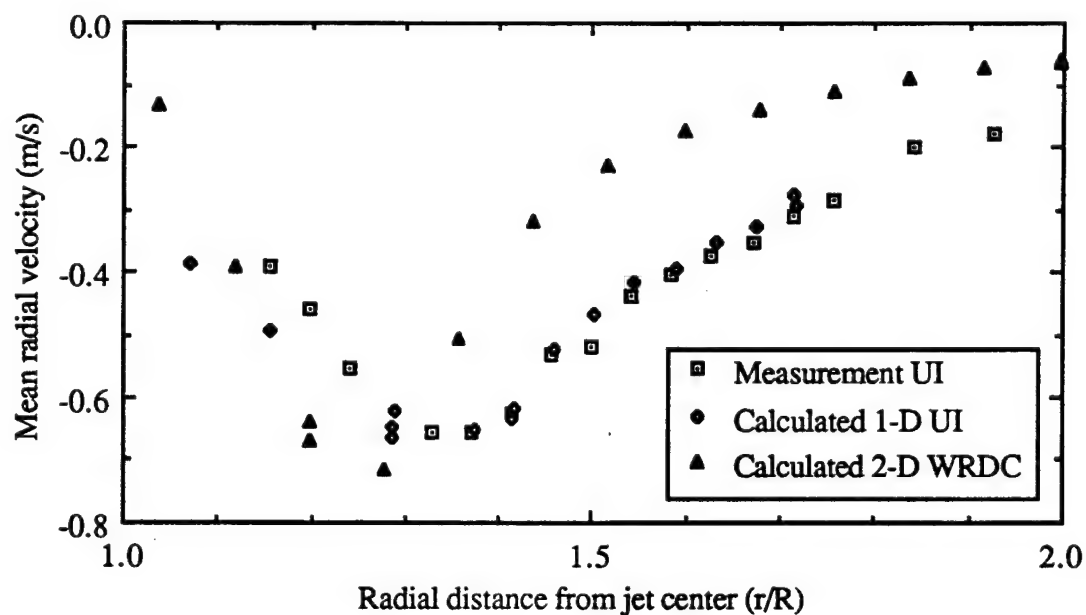
The radial velocity profiles at each annular flow condition are qualitatively similar in the flame region. The maximum inward radial velocities moved away from the jet center as the annular flow rate is increased as shown in Fig 4.19 and Fig 4.20 (WRDC and UI). For the conditions tested, the movement is approximately 0.1 mm (or 0.04 R) for each condition. The radial movement in the maximum inward radial velocity may be due to the change in lift-off velocities for annulus Conditions A through C. At the low annulus velocity, the lift-off velocity is high (approximately 30.4 m/s) and the time for diffusion of fuel to the flame zone is minimal. However, at the high annular flow rate the lift-off velocity is lower (approximately 19.5 m/s) giving more time for the fuel to diffuse radially outward.

The radial profiles including conditions A, B, and C recorded at UI are presented in Fig. 4.20(a). Condition A⁺ represents velocity measurements at 2.2 mm above the nozzle exit ($x/d = 0.47$), 0.4 mm above the standard axial location. Condition A⁺ was taken to ensure that the radial profile be taken across the flame zone, Table 4.1 shows a gap of 1.7 mm at Condition A. The radial velocity profiles of Conditions A and A⁺ were nearly identical.

The LDA data for direct radial velocity component measurements at UI are shown in Fig. 4.20(a). A comparison of direct measurement (UI), three position calculation (1-D UI), and rotation of coordinates of the two-channel measurements (2-D WRDC) are shown in Fig. 4.20(b). The mean radial velocity is determined by the three position calculation (Equation 2.11) at the UI (1-D UI) and by the rotation of coordinates (Equation 2.2) at



(a) Annular Conditions at UI



(b) Annular Condition B at UI and WRDC

Figure 4.20 Radial Velocity Profiles of Annular Conditions

WRDC (2-D WRDC). The direct measurement and the three position radial calculation (1-D) are consistent over the regions examined.

The laminar flamelet model which utilizes the straining rate (dV/dr) across the flame as the extinction mechanism can be evaluated since the measurements are taken across the flame zone at UI. The straining rates across the flame should be the same for different annular flow conditions when pure methane is used. The hot (flame) zone was recorded for each of the conditions listed in Table 4.1. The straining rate is calculated by a linear fit of the mean radial velocity over the hot (flame) zone. The straining rates for Conditions A through C and their respective radial ranges are listed in Table 4.3.

Table 4.3 Straining Rates at Annular Conditions A, B, and C

Condition	Exit Velocity (m/s)	Straining rate (1/s)	Range of data points (mm) (r/R)	
A	26.70	400 ± 31	2.9 - 3.8	1.25 - 1.67
A+	26.70	431 ± 30	3.0 - 3.9	1.29 - 1.67
B	23.30	454 ± 42	3.1 - 3.9	1.33 - 1.67
C	19.05	436 ± 47	3.3 - 3.9	1.41 - 1.67

The magnitude of the straining rates vary from 400 to 454 1/s for conditions A to C. The uncertainty is typically ± 35 1/s which is greater than the range of the straining rates. The straining rates fluctuate 12% over the conditions tested. The straining rates are consistent within experimental error for the annular conditions tested. The consistency of the straining rates, therefore, supports the laminar flamelet model in describing the lift-off process.

4.3.5 Diluent Effects

LDA measurements underneath the base of the flame ($x/d = 0.2$) for the annulus Conditions A, B, and C did not support the premixed flame model as discussed in Section 4.3.4. The straining rates were obtained for diluted methane jet diffusion flames prior to lift-off. The LDA measurements were taken at $x/d = 0.4$ or 1.8 mm above the burner exit. To evaluate the diluent effects extinction data for diluted methane counter-flow diffusion flames were examined (Ishizuka and Tsuji, 1981) and compared to the methane jet diffusion flame data taken in the present study.

LDA data were taken for argon or helium diluted methane jet diffusion flames near lift-off. The data are summarized in Figures 4.21 and 4.22 for argon diluted experiments and Figures 4.23 and 4.24 for helium diluted results. The conditions (0 through 2) are listed in Table 4.2, the annulus flow rate was held constant at Condition B. Dimensional units were used to quantify the straining rates and to compare actual velocities in the flame zone.

The axial profiles of each condition were nearly identical in the flame zone. Figures 4.21 and 4.22 compare the mean axial velocity distribution of argon and helium mixtures to that of the pure methane flame, respectively. The axial velocities are within five percent at each radial location from 1.4 to 1.8 r/R at all conditions tested. The flame zone is also positioned in this range for the dilutions tested.

The mean axial velocity profiles between the different dilution conditions is not consistent with the premixed flame model. The premixed model states that the local convective reactant mixture exceeds the local flame speed at lift-off. The flame speed is determined empirically using fully premixed reactants in a turbulent free shear flow

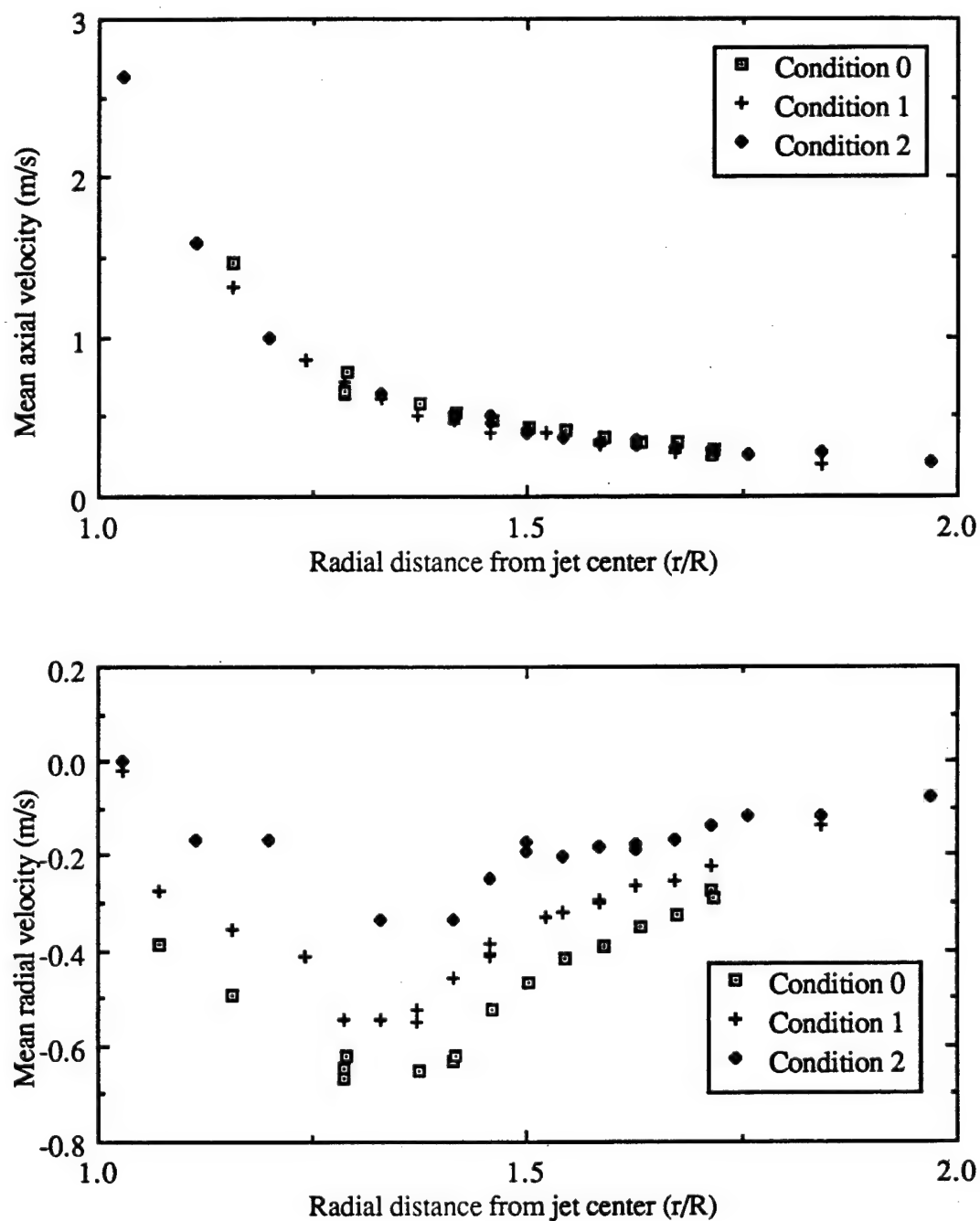


Figure 4.21 Mean Velocity Profiles in Methane/Argon Jet Diffusion Flames

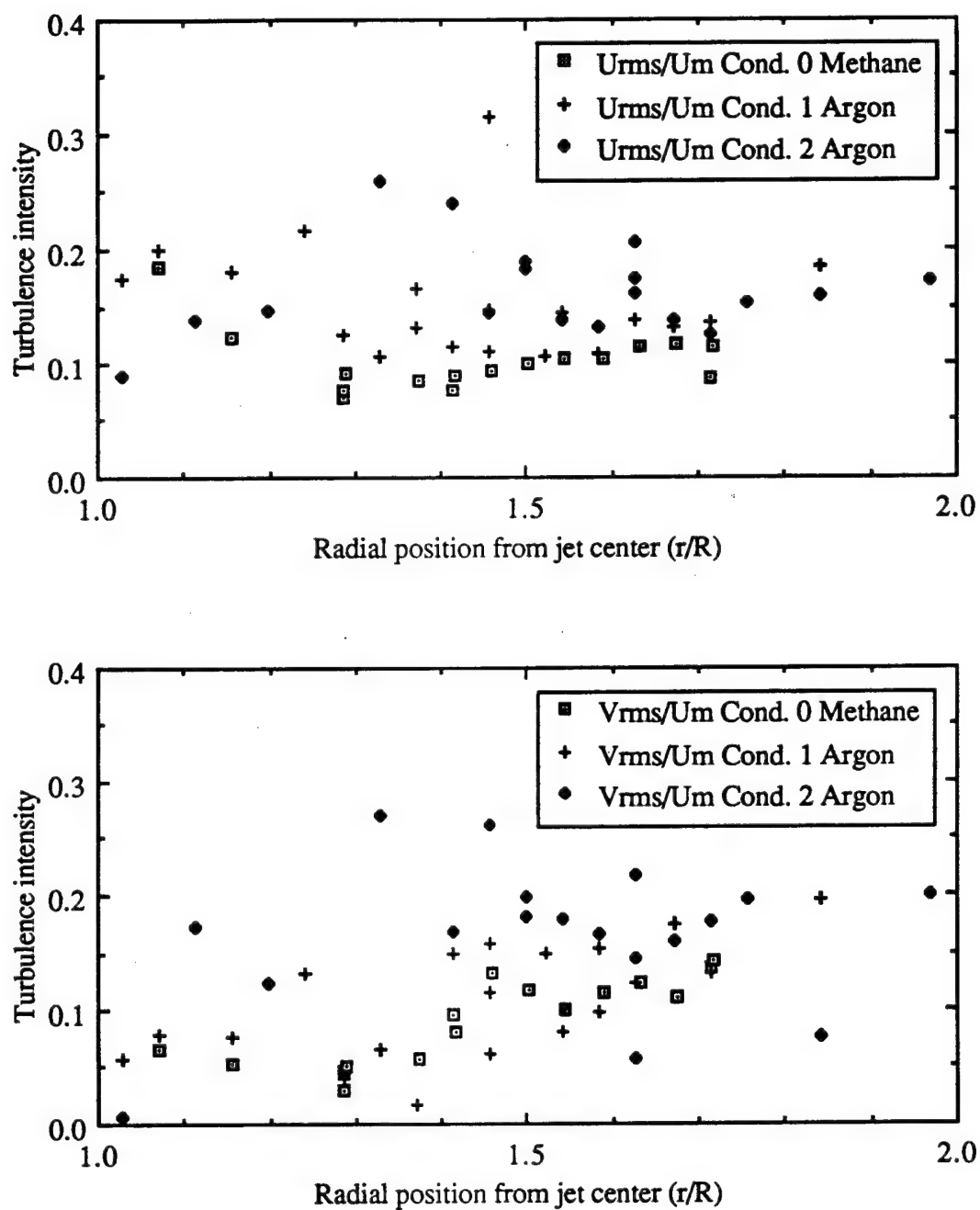


Figure 4.22 Velocity Fluctuation Profiles in Methane/Argon Jet Diffusion Flames

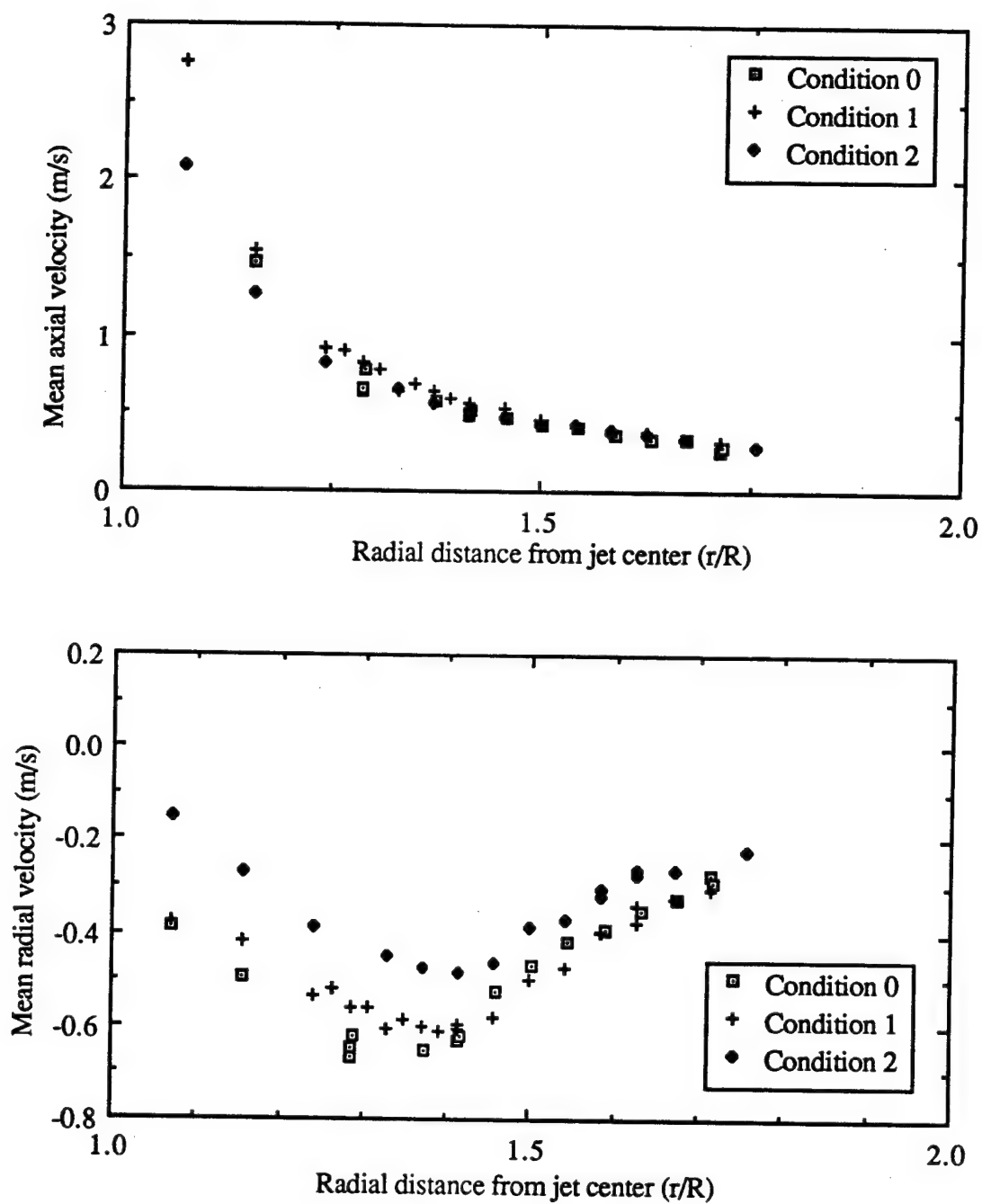


Figure 4.23 Mean Velocity Profiles in Methane/Helium Jet Diffusion Flames

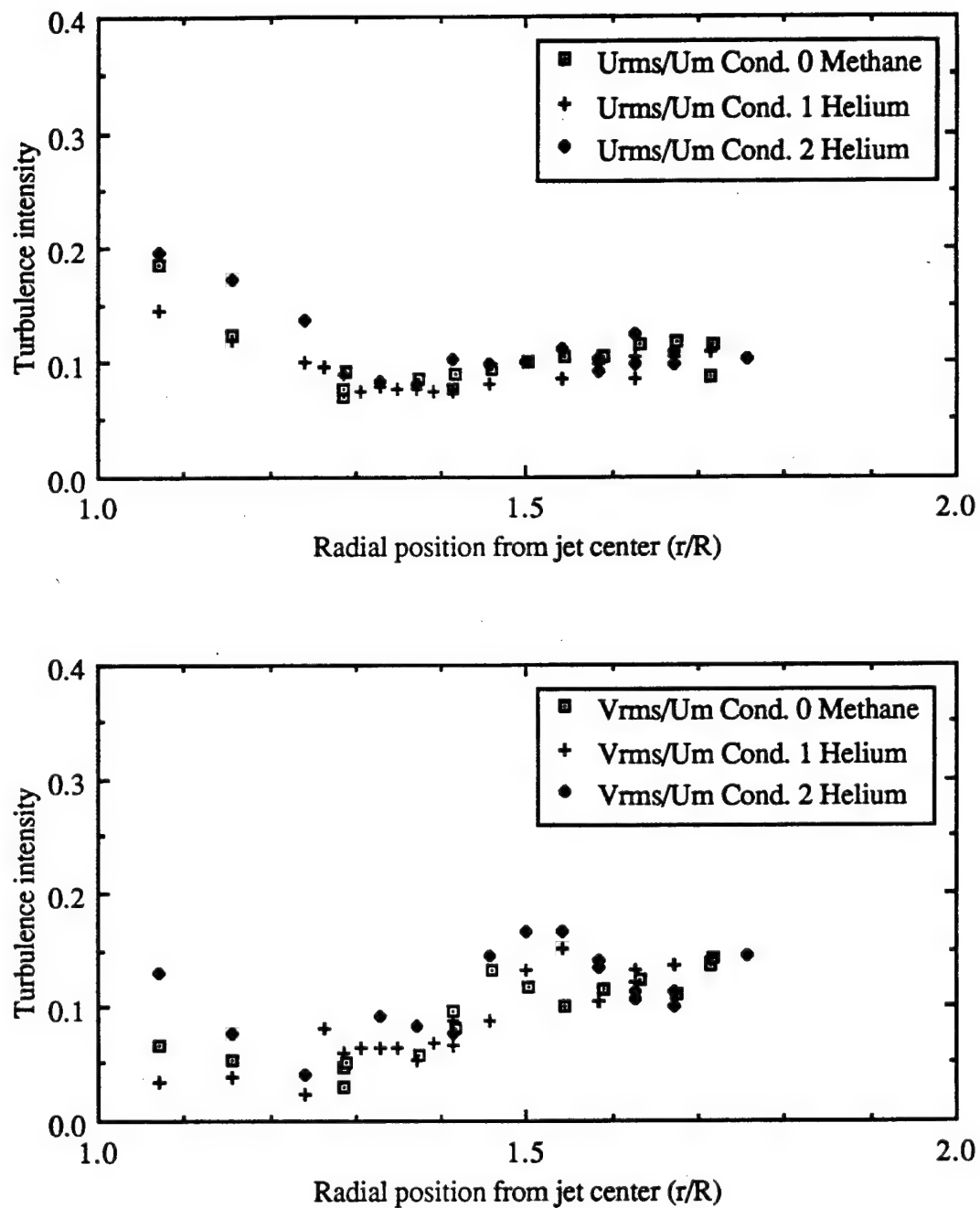


Figure 4.24 Velocity Fluctuation Profiles in Methane/Helium Jet Diffusion Flames

environment. The local flame speed is proportional to the product of the turbulence intensity and the laminar flame speed. The turbulence intensities in the flame zone are nearly constant for the dilutions used (Figures 4.21 and 4.23). The laminar premixed flame speed is reduced due to the addition of inerts (Clingman et al., 1953). Therefore, the turbulent flame speed should decrease with increasing dilutions. Since the axial velocity is nearly constant over the dilutions tested, the laminar flame speed model does not appear to be the primary mechanism in the lift-off conditions examined.

The mean radial profiles are similar at all conditions tested. The maximum mean radial velocity moves radially outward as the dilution is increased. Again, this may be due to the lower lift-off velocities at higher dilutions which increase the time for the diffusion of fuel to expand radially outward. The flame zone shows the same trend, meaning the mean radial profile is an indication of the position of the flame zone.

The straining rate is calculated for the different dilutions by a linear best-fit of the mean radial velocity over the flame zone. The range of data points used in the calculation varied according to the flame zone location as shown in Figure 4.25. A line representing the linear best-fit for the methane-helium mixture at Condition 2 is shown in Figure 4.25. The minimum r/R value was selected at the point near the maximum velocity which correlates to the inside of the hot zone. The maximum r/R location was selected at the location closest to the outside of the hot zone. Table 4.4 summarizes the straining rates obtained from Figure 4.25 for each condition. The uncertainty range of the straining rates in Tables 4.3 and 4.4 are between 17 and 47 $1/s$ as calculated in Appendix E.

The straining rate decreases as the dilution increases for all cases. The straining rates of pure methane jet diffusion flames at near lift-off is greater than the straining rates derived from the counter-flow diffusion flame experiments (350 $1/s$) of Ishizuka and Tsuji (1981).

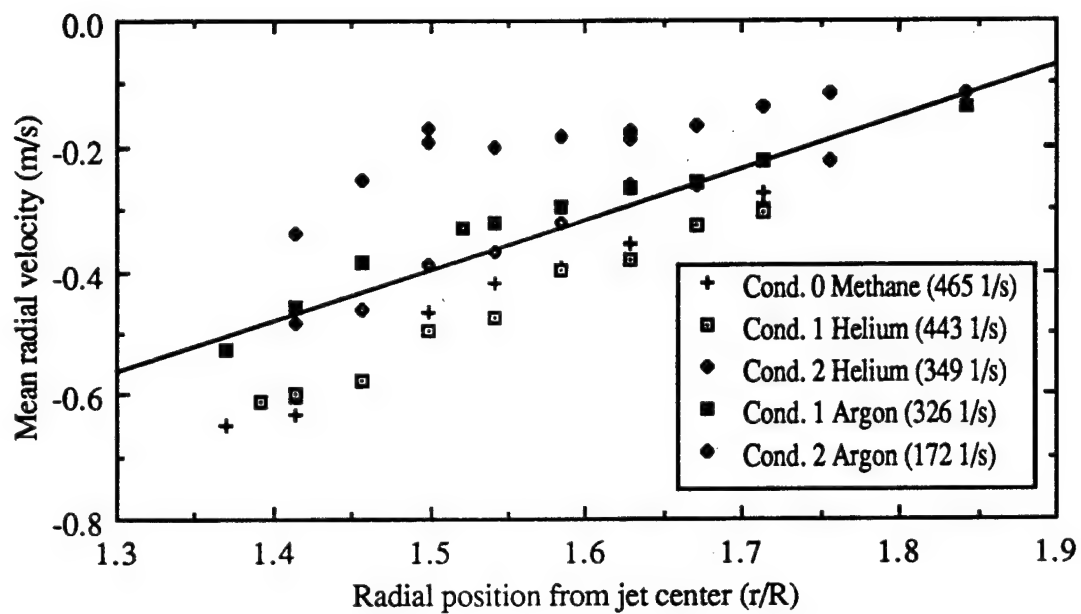


Figure 4.25 Straining Rates in Diluted Methane Jet Diffusion Flames

Table 4.4 Straining Rates at Diluted Conditions

Fuel/Inert	Cond.	Straining rate (1/s)	Range of data points (mm) (r/R)	
Methane	0	465 ± 35	3.2 - 4.0	1.37 - 1.71
Methane/Argon	1	326 ± 17	3.2 - 4.3	1.37 - 1.84
Methane/Argon	2	172 ± 21	3.3 - 4.3	1.41 - 1.84
Methane/Helium	1	443 ± 38	3.25 - 4.0	1.39 - 1.71
Methane/Helium	2	349 ± 32	3.3 - 4.1	1.41 - 1.76

The straining rate in a methane jet diffusion flame of the present study is within two percent of the straining rate determined by the TFP method (460 1/s) of Chen and Goss (1989).

Methane-argon at Condition 1 and methane-helium at Condition 2 are similar with respect to the jet exit velocity, 15.7 m/s and 14.3 m/s, respectively. The radial location of the flame is greater for the helium dilution than the argon dilution by 0.2 mm. The axial velocity magnitudes are nearly equal at each radial location in the hot (flame) zone. Since the methane-helium dilution has a greater radial distance than the argon dilution, the axial velocity of helium is lower than that of the argon. However, the laminar flame speed of helium mixtures is 30% greater than argon mixtures at stoichiometry (Clingman et al., 1953). The straining rates at these two conditions are nearly equal, which agrees with the observations of Ishizuka and Tsuji (1981).

A comparison of diluted counter-flow diffusion flame of Ishizuka and Tsuji (1981) with the present results is summarized in Fig. 4.26. The comparison is based on the normalized straining rate with 350 1/s for argon and helium diluted counter-flow diffusion flames (Ishizuka and Tsuji, 1981) and 465 1/s for jet diffusion flames of the present study.

The counter-flow diffusion flame experiments examined the extinction conditions of methane diffusion flames diluted by argon or helium gases. The results of Ishizuka and Tsuji (1981) found that helium has a more destabilizing effect than that of argon. The present stability curves and straining rates are in qualitative agreement with Ishizuka and Tsuji (1981).

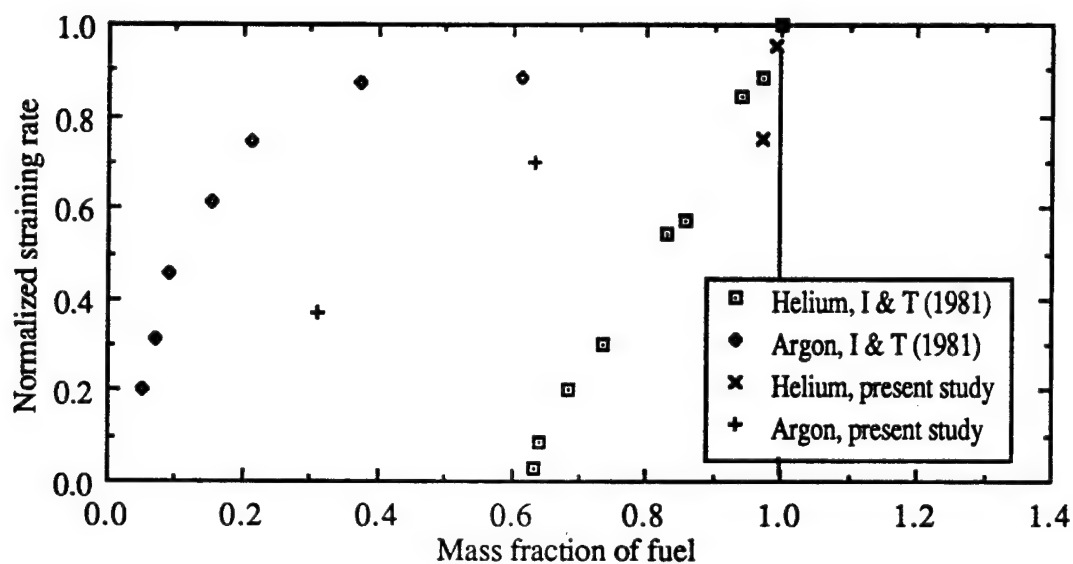


Figure 4.26 Comparison of Extinction Straining Rate for Methane Counter-Flow Diffusion Flames with Lift-Off Straining Rate for Methane Jet Diffusion Flames (I&T, 1981, Denotes Ishizuka and Tsuji, 1981)

CHAPTER V

SUMMARY AND CONCLUSIONS

The objective of this research was to investigate the near field, lift-off phenomena of methane and propane jet diffusion flames. The investigation consists of characterizing the flow field near the burner exit before and after the lift-off of methane jet diffusion flames. Cold jet data were obtained to compare with the axial and radial velocity profiles of attached and lifted methane jet diffusion flames near the nozzle exit. Velocity characterization was performed by laser Doppler anemometry (LDA), and the hot (flame) zone by a thin filament (15 μm SiC fiber). Annulus, diluted fuel, and external nozzle geometry effects were studied. Three dilution gases are considered, argon, helium, and nitrogen. The results were compared to existing theories on the lift-off of jet diffusion flames, i.e. the premixed flame theory and laminar flame model.

Stability curves were established for methane and propane jet diffusion flames at different annular flows, fuel mixture compositions, and external burner geometries. The stability curves define the condition for stabilized and lifted jet diffusion flames from which detailed LDA measurement conditions are determined. The stability curves showed the sensitivity of the initial conditions on the lift-off phenomena.

Diluting the methane and propane jet diffusion flames with argon, nitrogen and helium reduces the lift-off velocity, thus decreasing the stability of jet diffusion flames. The most destabilizing additive was helium, the least was argon. The previous study of Takahashi et al. (1984), however, observed opposite results for diluted hydrogen jet diffusion flames,

namely, helium having the least destabilizing effects and argon having the most destabilizing effects.

The most significant difference between an attached flame and a lifted flame or a cold jet is in the radial velocity. The maximum radial velocity of a cold jet or lifted flame is near the shear layer of the jet. The attached flame, however, has a maximum radial velocity outside the shear layer in the annular region. The maximum velocity coincides with the interior of the flame zone for all the dilutions tested. As the flame zone moves radially outward with increasing dilutions, the maximum mean radial velocity moves outward at the same rate.

The premixed flame theory was assessed by the local mean axial velocity prior to the flame zone. The LDA data at different annular flow rates revealed the mean axial velocity varied by 100%, and at diluted conditions the velocity was constant. These observations suggest that the premixed flame theory is not the appropriate model in determining the lift-off velocity of methane jet diffusion flames.

The local straining rate across the flame was approximated by that calculated from the mean radial velocity profile. The calculated straining rates at near lift-off conditions are in agreement with Chen and Goss (1989) for pure methane jet diffusion flames, and quantitatively agrees with the straining rates obtained by Ishizuka and Tsuji (1981) for the extinction condition of counter-flow diffusion flames. These results suggest that the laminar flamelet model is more accurate than the premixed flame theory in predicting the lift-off of methane jet diffusion flames examined. However, more experiments are needed to test the generality of this observation. The straining rate calculated by the radial velocity profile show promise of setting a criterion for the lift-off of jet diffusion flames.

The present study observed that an external contraction of the nozzle near the exit enhances the stability of jet diffusion flames, especially at higher annular velocities. Further work on the external geometry effects seems warranted. Further research is also

required in the characterization of the lift-off phenomena, to generalize the straining rate observation. Numerical calculation of the near field of a combusting jet is desired, when a numerical model can predict the straining rates and flame zone location, a sufficient condition for lift-off may be established.

REFERENCES

Abdel-Gayed, R., Bradley, D., and Lawes, M., (1987). Turbulent Burning Velocities: a General Correlation in Terms of Straining Rates. Proc. R. Soc. Lond. Series A, Vol. 414, pp. 389-413

Andrews, G., Bradley, D., and Lwakabamba, S., (1975). Turbulence and Turbulent Flame Propagation - A Critical Appraisal. Combustion and Flame. Vol. 24, pp. 285-304.

Annushkin, Y., and Sverdlov, E., (1979). Stability of Submerged Diffusion Flames in Subsonic and Underexpanded Supersonic Gas-Fuel Streams. Combustion, Explosions and Shock Waves. Vol. 14, No. 5, pp. 597-605.

Bates, C.J., and Hughes T.D.R., (1977). The Effect of Both Sample size and Sampling Rate on the Statistical Fluid Flow Parameters in a High Reynolds Number, Low Turbulence Intensity Flow. Proceeding of the Fifth Biennial Symposium on Turbulence. University of Missouri, Rolla, pp. 125-131.

Chen, T.H., and Goss L.P., (1989). Flame Lifting and Flame/Flow Interactions of Jet Diffusion Flames. AIAA paper No. 89-0156.

Clingman, W., Brokaw, R., and Pease, R., (1953). Burning Velocities of Methane with Nitrogen-Oxygen, Argon-Oxygen, and Helium-Oxygen Mixtures. Fourth Symposium (International) on Combustion. pp. 310-313.

Dahm, D., and Dibble, R., (1988). Combustion Stability Limits of Coflowing Turbulent Jet Diffusion Flames. AIAA paper No. 88-0538.

Donnerhack, S., and Peters, N., (1984). Stabilization Heights in Lifted Methane-Air Jet Diffusion Flames Diluted with Nitrogen. Combustion Science and Technology. Vol. 41, pp. 101-108.

Eickhoff, H., Lenze, B., and Lueckel, W., (1984). Experimental Investigation on the Stabilization Mechanism of Jet Diffusion Flames. Twentieth Symposium (International) on Combustion. pp. 311-318.

- Gibson, Carl, (1968). Fine Structure of Scalar Fields Mixed by Turbulence. II. Spectral Theory. The Physics of Fluids. Vol. 11, No. 11, pp. 2316-2327.
- Gollahalli, S., (1977). Effects of Diluents on the Flame Structure and Radiation of Propane Jet Flames in a Concentric Stream. Combustion Science and Technology. Vol. 15, pp.147-160.
- Gollahalli, S., Savas, O., Huang, R., and Rodriquez Azara, J., (1986). Structure of Attached and Lifted Gas Jet Flames in Hysteresis Region. Twenty-first Symposium (International) on Combustion. pp. 1463-1471.
- Horch, K., (1978). Zur Stabilität von Freistrah-Diffusionsflammen. Ph.D. Thesis. Universität Karlsruhe, FRG.
- Ishizuka, S., and Tsuji, H., (1981). An Experimental Study of Effect of Inert Gases on Extinction of Laminar Diffusion Flames. Eighteenth Symposium (International) on Combustion. pp. 695-703.
- Kalghatgi, G., (1981). Blow-Out Stability of Gaseous Jet Diffusion Flames. Part I: In Still Air. Combustion Science and Technology. Vol. 26, pp. 233-239.
- Kalghatgi, G., (1984). Lift-off heights and Visible Lengths of Vertical Turbulent Jet Diffusion Flames in Still Air. Combustion Science and Technology. Vol. 41, pp. 17-29.
- Karim, G., Wierzba, I., and Hanna, M., (1984). The Blowout Limit of a Jet Diffusion Flame in a Coflowing Stream of Lean Gaseous Fuel-Air Mixtures. Combustion and Flame. Vol. 51. pp. 283-288.
- McCaffrey, B., and Evans, D., (1986). Very Large Methane Jet Diffusion Flames. Twenty-first Symposium (International) on Combustion. pp. 25-31.
- McLaughlin, D., and Tiederman W., (1974) Biasing Correction for Individual Realization of Laser Anemometer Measurements in Turbulent Flows. The Physics of Fluids. Vol. 16, No. 12. pp. 2082-2088.
- Park, C.J., (1987). An Investigation of Particle-Laden Flows in a Simulated Dump Combustor. Ph.D. Thesis, The University of Iowa, Iowa City, Iowa.

Peters, N., and Williams, F., (1983). Liftoff Characteristics of Turbulent Jet Diffusion Flames. AIAA Journal, Vol. 21, No. 3, pp. 423-429.

Pitts, W., (1988). Assessment of Theories for the Behavior and Blowout of Lifted Turbulent Jet Diffusion Flames. Twenty-Second Symposium (International) on Combustion. pp. 809-816.

Seaba, J., and Chen, L.-D., (1989). An Investigation of Inverse Diffusion Flame. Spring Technical Meeting Central States Section. The Combustion Institute, Dearborn Michigan.

Seaba, J., Chen, L.-D., Goss L., and Roquemore W. (1990). Effects of Fuel Diluents on Lift-off of Jet Diffusion Flames. Spring Technical Meeting Central States Section. The Combustion Institute, Cincinnati Ohio.

Shekarchi, S., Savas, O., and Gollahalli, S., (1988). Structure of a Split Gas Flame. Combustion and Flame. Vol. 73, pp. 221-232.

Smith, K., and Gouldin, F., (1979). Turbulence effects on Flame Speed and Flame Structure. AIAA Journal. Vol. 17, No. 11, pp. 1243-1250.

Sønju, O., and Hustad, J., (1984). An Experimental Study of Turbulent Jet Diffusion Flames. Dynamics of Flames and Reactive Systems. pp. 320-339.

Takahashi, F., Mizomoto, M., and Ikai, S., (1980). Stability of Hydrogen Jet Diffusion Flames. Hydrogen Energy and Progress. pp. 1156-1176

Takahashi, F., Mizomoto, M., Ikai, S., and Futaki, N., (1984). Lifting Mechanism of Free Jet Diffusion Flames. Twentieth Symposium (International) on Combustion. pp. 295-302.

Takahashi, F., Mizomoto, M., Ikai, S., and Tsuruyama, K., (1990). Stability Limits of Hydrogen/Air Coflow Jet Diffusion Flames. AIAA paper No. 90-0034.

Takahashi, F., Schmoll W., and Vangsness, M., (1990). Effects of Swirl on the Stability and Turbulent Structure of Jet Diffusion Flames. AIAA paper No. 90-0036.

Takahashi, F., and Schmoll W., (1990). Lifting Criteria of Jet Diffusion Flames. Twenty-Third Symposium (International) on Combustion.

Takeno, T., and Kontani, Y., (1975). An Experimental Study on the Stability of Jet Diffusion Flame. Acta Astronautica. Vol. 2, pp. 999-1008.

Vanquickenborne, L., and van Tiggelen, A., (1966). The Stabilization Mechanism of Lifted Diffusion Flames. Combustion and Flame. Vol. 10, pp. 59-69.

Vranos, A., Taback, E., and Shipman, W., (1968). An Experimental Study of the Stability of Hydrogen-Air Diffusion Flames. Combustion and Flame. Vol. 12, pp. 253-260.

Williams, F., A., (1975) Turbulent Mixing in Non-Reactive and Reactive Flows, Plenum, pp. 189-208.

Williams, F., A., (1985) Combustion Theory, Second Edition, Benjamin Cummings, Menlo Park, CA.

Wohl, K., Knapp, N., and Gazley, C., (1949). Third Symposium (International) on Combustion, Flame, and Explosion Phenomena. p. 3.

Zsak, T., Perlee, C., and Chigier, N., (1984). Hysteresis in the liftoff and Reattachment of Hydrocarbon Flames. Fall Sectional Meeting of The Combustion Institute, Clearwater Florida.

APPENDIX A

MEASURING VOLUMES

The measuring volume(s) is created by two or three coherent laser beams intersecting each other. The boundary of the measuring volume is defined as the region having an intensity of e^{-2} times of that of the beam at the centerline. The measuring volume was ellipsoidal in shape and had an interference fringe pattern. The dimensions of the measuring volume can be calculated from the following equations:

Major axis of the measuring volume

$$l_m = d e^{-2} / \sin \theta = 4.29 \text{ mm (WRDC)}$$

$$= 1.36 \text{ mm (UI)}$$

Minor axis of the measuring volume

$$d_m = d e^{-2} / \cos \theta = 0.2099 \text{ mm (WRDC)}$$

$$= 0.1316 \text{ mm (UI)}$$

Fringe spacing

$$d_f = \lambda / (2 \sin \theta) = 5.266 \text{ } \mu\text{m (WRDC)}$$

$$= 2.6767 \text{ } \mu\text{m (UI)}$$

Number of fringes in the measuring volume

$$N_f = d_m / d_f = 40 \text{ (WRDC)}$$

$$= 50 \text{ (UI)}$$

Waist diameter of the laser beam

$$d_{e-2} = 4 \lambda f / \pi D_{e-2} = 0.2096 \text{ mm (WRDC)}$$

$$= 0.1310 \text{ mm (UI)}$$

where λ (514.5 nm) is the laser wavelength, k (2.80° WRDC, 5.515° UI) is the half angle between incident light beams, f (400 mm WRDC, 250 mm UI) is the focal length of the sending optics, and D_{e-2} and d_{e-2} are the entering and waist diameters of the laser beam, respectively.

APPENDIX B

EQUIPMENT LIST FOR LDA AT WRDC

1. Mirror
Dia. 2 inches
Manufacture: NRC
2. Beam splitter
Manufacture: TSI
3. Bragg cell
Manufacture: InterAction Corp.
Model: AOM-405
Serial No. 1841
- 3A. Bragg cell
Manufacture: InterAction Corp.
Model: AOM-355
Serial No. 5682
4. Bragg cell driver
Manufacture: InterAction Corp.
Model: ME 35R
Serial No. 2844
- 4A. Bragg cell driver
Manufacture: InterAction Corp.
Model: ME 40R

Serial No. 2097

5. Beam polarizer
Manufacturer: TSI
6. Beam steering lenses
Manufacturer: TSI
7. Aperture plate
8. Lens
 $f = 40$ cm. 3" dia.
Manufacturer: Oriel
9. Concave Mirror
 $f = 40$ cm. 4" x 6"
10. Lens
 $f = 10$ cm. 3" dia.
11. Prism, separates components by polarity.
12. Fiber optic cable and holder
Manufacturer: TSI

APPENDIX C

AVERAGED TIME QUANTITY DERIVATIONS

In turbulent flow situations the individual realizations of laser anemometry are biased. The biasing occurs because a larger than average number of particles pass through the measurement volume during periods when the velocity is faster than the mean. This is known as the high velocity bias analyzed by McLaughlin and Tiederman (1974). To compensate for the high velocity biasing using a frequency shifter the following definitions are used to calculate the mean and rms velocity fluctuations.

$$\bar{U} = \frac{\sum_{j=1}^N U_j \Delta t_j}{\sum_{j=1}^N \Delta t_j} \quad (C.1)$$

where U_j is the measured velocity, N is the number of samples taken, and Δt_j is the time the particle is in the measurement volume for velocity measurement. The Δt_j is calculated as follows:

$$\Delta t_j = \frac{N_b}{f_s + f_d} \quad (C.2)$$

N_b is the number of cycles per burst, f_s is the frequency shift, and f_d is the Doppler frequency produced by the particle. The frequency shift is in the opposite direction of the mean flow. The Doppler frequency is related to the particle velocity (U_j) by the equation,

$$f_d = \frac{U_j}{d_f}. \quad (C.3)$$

The variable d_f is the fringe spacing in the measurement volume, defined in Appendix A.

Combining Eqs. (C.2) and (C.3), one obtains

$$\Delta t_j = \frac{N_b d_f}{d_f f_s + U_j} \quad (C.4)$$

Substituting Eq. (C.4) into Eq. (C.1), and let $c = d_f f_s$, the mean velocity is calculated by:

$$\bar{U} = \frac{\sum_{j=1}^N \frac{U_j}{U_j + c}}{\sum_{j=1}^N \frac{1}{U_j + c}}. \quad (C.5)$$

Similarly, the rms velocity is calculated by

$$U_{rms}^2 = \frac{\sum_{j=1}^N (U_j - \bar{U})^2 \Delta t_j}{\sum_{j=1}^N \Delta t_j}. \quad (C.6)$$

Substituting Eq. (C.4) into Eq. (C.6), one obtains

$$U_{\text{rms}}^2 = \frac{\sum_{j=1}^N \frac{(U_j - \bar{U})^2}{U_j + c}}{\sum_{j=1}^N \frac{1}{U_j + c}}. \quad (\text{C.7})$$

APPENDIX D

CALCULATIONS FOR THREE POSITION ORIENTATION VELOCITY
MEASUREMENTS

Three orientations were measured (U^+ , U^- , and U) in order to characterize the flow field for the one channel LDA system. Figure 2.8 shows the vector orientation. The calculation of \bar{V} and V_{rms} are derived as follows:

$$\bar{U} = \bar{U}^+ \sin \theta + \bar{U}^- \cos \theta \quad (D.1)$$

$$\bar{V} = \bar{U}^+ \cos \theta - \bar{U}^- \sin \theta. \quad (D.2)$$

By definition, $\overline{U_j'^2} = U_{rms}^2$, and similarly for the other rms velocities.

$$U_{rms}^2 = \overline{U_{rms}^{+2}} \sin^2 \theta + \overline{U_{rms}^{-2}} \cos^2 \theta + 2 \overline{U_j^{+'} U_j^{-'}} \sin \theta \cos \theta \quad (D.3)$$

$$V_{rms}^2 = \overline{U_{rms}^{+2}} \cos^2 \theta + \overline{U_{rms}^{-2}} \sin^2 \theta - 2 \overline{U_j^{+'} U_j^{-'}} \sin \theta \cos \theta. \quad (D.4)$$

Adding Eqs. (D.3), (D.4), one obtains

$$U_{rms}^2 + V_{rms}^2 = U_{rms}^{+2} + U_{rms}^{-2}$$

Rearranging:

$$V_{rms}^2 = U_{rms}^{+2} + U_{rms}^{-2} - U_{rms}^2 \quad (D.5)$$

the terms on the RHS of Eq. (D.5) are measured, and V_{rms} can be calculated by Eq. (D.5).

Rearranging (D.3), one obtains

$$\overline{U_j^+ U_j^-} = \frac{U_{rms}^2 - U_{rms}^{+2} \sin^2 \theta - U_{rms}^{-2} \cos^2 \theta}{2 \sin \theta \cos \theta} \quad (D.6)$$

The definition of Reynolds stress is

$$\overline{U_j' V_j'} = \overline{(U_j - \bar{U}) (V_j - \bar{V})}$$

which can be reduced to the following equation

$$\overline{U_j' V_j'} = (\bar{U_j^{+2}} - \bar{U_j^{-2}}) \sin \theta \cos \theta + \bar{U_j^{+2}} - \bar{U_j^{-2}} (\cos^2 \theta - \sin^2 \theta). \quad (D.7)$$

Substituting Eq. (D.6) and the definition of rms into Eq. (D.7) the Reynolds stress equation becomes:

$$\begin{aligned} \overline{U_j' V_j'} = & (U_{rms}^{+2} - U_{rms}^{-2}) \sin \theta \cos \theta \\ & + \left(\frac{\cos^2 \theta - \sin^2 \theta}{2 \sin \theta \cos \theta} \right) (U_{rms}^2 - U_{rms}^{+2} \sin^2 \theta - U_{rms}^{-2} \cos^2 \theta). \end{aligned} \quad (D.8)$$

The Fortran code to compute the velocities are summarized in the following.


```

c
c Data reduction program for LDV measurements at U of I.
c Programmer J.P. Seaba, J.P. Jaeger Date June 3, 1990
c
Double Precision U(10000), fd(10000), dm(10000), e(10000)
Double Precision df, Um, Urms, fs, UmPOS, UmNEG, delta
Double Precision UrmsPO, UrmsNE, SumPOS, SumNEG, Theta
Double Precision Re, Umcalc, Vmcalc, Vrms, Error1, Error2
Double Precision N, alpha, Um2, Urms2, OurSIN, OurCOS, z
Double Precision Umcomp, Vmcomp, ReCOMP, UmPcom, UmNcom
Double Precision UrmPco, UrmNco
Real radial, radpos(99)
Integer Isize, Jsize, Num, jj, Test
Character*32 Date, Line2, Line3, Filep, Filef
Character*16 Filea, Filec, Filev
Character*2 Ext2(99), Ext3, Ext4, Ext8
Character*4 Ext5, Ext6, Ext7

c
c Initialize I/O
c
Date = 'None'
Line2 = 'None'
Line3 = 'None'
Ext3 = 'p.'
Ext4 = 'm.'
Ext5 = 'm.p.'
Ext6 = 'com.'
Ext7 = 'ens.'
Ext8 = 'v.'

c
Data Ext2 /1 '1' '2' '3' '4' '5' '6' '7' '8' '
1 '9' '10' '11' '12' '13' '14' '15' '16' '17' '18' '
1 '19' '20' '21' '22' '23' '24' '25' '26' '27' '28' '29' '
1 '30' '31' '32' '33' '34' '35' '36' '37' '38' '39' '40' '
1 '41' '42' '43' '44' '45' '46' '47' '48' '49' '50' '51' '
1 '52' '53' '54' '55' '56' '57' '58' '59' '60' '61' '62' '
1 '63' '64' '65' '66' '67' '68' '69' '70' '71' '72' '73' '
1 '74' '75' '76' '77' '78' '79' '80' '81' '82' '83' '84' '
1 '85' '86' '87' '88' '89' '90' '91' '92' '93' '94' '95' '
1 '96' '97' '98' '99' /

c
Data radpos / 99*0.0 /

c
Print*, 'Start of LDV data processing program'
Print*, "

c
c Define parameters
c
Iscr = 9
fs = 10E6
N = 32

```

```

df    = 2.6767E-6
delta = 0.017453*0.2
Theta = 45 * ( 0.017453 )

```

c

```

Print*, 'Enter the filename you wish to call the processed data:'
Read(Iscr,*) Filef
Print*, "
Print*, 'Enter three lines of date and test conditions:'
Read(Iscr,*) Date
Read(Iscr,*) Line2
Read(Iscr,*) Line3
Print*, "
Print*, 'Number of data points in mantissa and exponent file'
Read(Iscr,*) Jsize

```

c

```

Filep = Ext7//Filef
Open(35, File = Filep )
Write(35,65) Date
Write(35,65) Line2
Write(35,65) Line3
Write(35,62)
Write(35) 'Ensemble Translated Data:'
Write(35,62)
Write(35) ' Radial U_mean V_mean U_rms V_rms
1 U_mean Reynolds File U_mean'
Write(35,62)
Write(35) ' Distance (calc) (calc)
1 (calc) Stress Number Error'
Write(35,62)
Write(35) ' (mm) (m/s) (m/s) (m/s) (m/s)
1(m/s) (m^2/s^2) %'
Write(35,62)
Write(35) '_____

```

```

1_____

```

```

Write(35,62)

```

c

```

Filep = Ext5//Filef
Open(36, File = Filep )
Write(36,65) Date
Write(36,65) Line2
Write(36,65) Line3
Write(36,62)
Write(36) ' Radial Mean RMS Comp Mean Comp RMS
1File Orientation'
Write(36,62)
Write(36) ' Distance Velocity Velocity Velocity Velocity
1 Number'
Write(36,62)
Write(36) ' (mm) (m/s) (m/s) (m/s) (m/s)'
Write(36,62)

```

```

Write(36) '_____
1_____
Write(36,62)
c
Filep = Ext6//Filef
Open(37, File = Filep )
Write(37,65) Date
Write(37,65) Line2
Write(37,65) Line3
Write(37,62)
Write(37) 'Compensated Translated Data:'
Write(37,62)
Write(37) ' Radial U_mean V_mean U_rms V_rms
1 U_mean Reynolds File U_mean'
Write(37,62)
Write(37) ' Distance (calc) (calc)
1 (calc) Stress Number Error'
Write(37,62)
Write(37) ' (mm) (m/s) (m/s) (m/s) (m/s)
1(m/s) (m^2/s^2) %'
Write(37,62)
Write(37) '_____
1_____
Write(37,62)
c
Print*, 'Name of file with mantissa and exponent'
Read(Iscr,*) Filev
c
Print*, 'What file number do you want to begin with?'
Read(Iscr,*) jj
c
Print*, 'How many files do you wish to process? '
Read(Iscr,*) Num
Num1 = Num + jj - 1
c
Print*, 'Is the radial position going to be constant?'
Print*, 'Enter "0" for Yes, "1" for No'
Read(Iscr,*) Test
If (Test .EQ. 0) Then
Print*, 'Enter the constant radial distance, in mm'
Read(Iscr,*) radial
Else
Do 90 i = jj, Num1
Write(Iscr,80) Filev,i
Read(Iscr,*) radpos(i)
90 Continue
80 Format ('Enter the radial position, in mm, for ',a5,I2)
c
Endif

```

```

c      Print*, 'Processing...'
      Print*, "
c
      Filea = Filev
      Filea = Ext2(jj)//Ext3//Filea
      Do 500 j = jj, Num1
        Do 600 m = 1,3
          Isize = Jsize
          Open(20, file = Filea)
c
c      Initialize arrays
c
      Do 5 i = 1, Isize
        U(i) = 0.0
        fd(i) = 0.0
        dm(i) = 0.0
        e(i) = 0.0
5      Continue
c
      Do 75 i = 1, Isize
        Read(20,100) dm(i), e(i)
75      Continue
c
c      Convert mantissa and exponent to frequency and velocity data
c
      Do 10 i = 1, Isize
        fd(i) = ((N*1E9)/(dm(i)*2**(e(i)-2))) - fs
        U(i) = df*fd(i)
10      Continue
c
      Call Stat ( U, Isize, fs, df, Um, Urms,Um2,Urms2 )
      Call Filter ( U, Isize, Um2, Urms2 )
      Call Stat ( U, Isize, fs, df, Um, Urms,Um2,Urms2 )
c
      Filea = Filev
      If ( m .EQ. 1 ) Then
        Filea = Ext2(j)//Ext4//Filea
        If ( Test .EQ. 0 ) Then
          Write(36,61) radial,Um,Urms,Um2,Urms2,j,Ext3
        Else
          Write(36,61) radpos(j),Um,Urms,Um2,Urms2,j,Ext3
        Endif
        UmPOS = Um
        UrmsPO = Urms
        UmPcom = Um2
        UrmPco = Urms2
c
      Elseif ( m .EQ. 2 ) Then
        Filea = Ext2(j)//Ext8//Filea
        If ( Test .EQ. 0 ) Then

```

```

        Write(36,61) radial,Um,Urms,Um2,Urms2,j,Ext4
    Else
        Write(36,61) radpos(j),Um,Urms,Um2,Urms2,j,Ext4
    Endif
    UmNEG = Um
    UrmsNE = Urms
    UmNcom = Um2
    UrmNco = Urms2
c
    Else
        Filea = Ext2(j+1)//Ext3//Filea
c
    Endif
c
    Close(20)
600    Continue
c
c*****
c
    alpha = Theta + delta
c
    Call Trig ( OurSIN, OurCOS, alpha )
    Umcalc = UmPOS*OurSIN + UmNEG*OurCOS
    Vmcalc = UmPOS*OurCOS - UmNEG*OurSIN
    Umcomp = UmPcom*OurSIN + UmNcom*OurCos
    Vmcomp = UmPcom*OurCOS - UmNcom*OurSIN
c
c    Calculate Reynolds stress
c
    Re = (UrmsPO**2-UrmsNe**2)*OurSIN*OurCOS +
1      (OurCOS**2-OurSIN**2)/(2*OurSIN*OurCOS) *
1      (Urms**2-UrmsPO**2*OurSIN**2-UrmsNE**2*OurCOS**2)
c
    ReCOMP = (UrmPco**2-UrmNco**2)*OurSIN*OurCOS +
1      (OurCOS**2-OurSIN**2)/(2*OurSIN*OurCOS) *
1      (Urms2**2-UrmPco**2*OurSIN**2-UrmNco**2*OurCOS**2)
c
    Vrms = Sqrt(Abs(UrmsPO**2 + UrmsNE**2 - Urms**2))
    Vrms2 = Sqrt(Abs(UrmPco**2 + UrmNco**2 - Urms2**2))
c
    Error1 = Abs(100*(Umcalc - Um)/ Um)
    Error2 = Abs(100*(Umcomp - Um)/Um)
c
    If ( Test .EQ. 0 ) Then
1      Write(35,60) radial,Um,Vmcalc,Urms,Vrms,
        Umcalc,Re,j,Error1
1      Write(37,60) radial,Um2,Vmcomp,Urms2,Vrms2,
        Umcomp,ReCOMP,j,Error2
    Else
1      Write(35,60) radpos(j),Um,Vmcalc,Urms,Vrms,
        Umcalc,Re,j,Error1

```

```

        Write(37,60) radpos(j),Um2,Vmcomp,Urms2,Vrms2,
1      Umcomp,ReCOMP,j>Error2
      Endif
c
c*****
c
500  Continue
c
61  Format ( 1x,f6.2,4x,f6.3,3x,f6.3,5x,f6.3,4x,f6.3,6x,I3,7x,
1    a3)
60  Format (f6.2,2x,f7.3,1x,f7.3,3x,f6.3,3x,f6.3,3x
1    f6.3,1x,f8.5,2x,I3,1x,f7.2)
100 Format (f10.2,6x,f10.2)
62  Format (/)
65  Format ( 2x,a32 )
      Close(35)
      Close(36)
      Close(37)
      Print*, "
      Print*, 'Program has successfully processed
1 the file(s), hit return'
      Pause
      Stop
      End
c
c*****
c
      Subroutine Trig( OurSIN, OurCOS, z )
c
      Double Precision z, OurSIN, OurCOS
c
      OurSIN = z - (z**3)/6 + (z**5)/120 - (z**7)/5040
1      + (z**9)/362880 - (z**11)/39916800 +
1      (z**13)/6227020800 - (z**15)/1.3076743680E12
1      + (z**17)/3.5568742810E14
c
      OurCOS = 1 - (z**2)/2 + (z**4)/24 - (z**6)/720
1      + (z**8)/40320 - (z**10)/3628800 +
1      (z**12)/479001600 - (z**14)/87178291200
1      +(z**16)/2.0922789888E13
c
      Return
      End
c
c*****
c
      Subroutine stat(vel,npts,fs,df,avg,stn,avg2,stn2)

      Double Precision vel(10000), sum2, avg2, stn2,fs,df
      Double Precision sum, sum1, avg, stn, Umax, Umin,c
      Double Precision sum3, sum4

```

```

Integer i, npts, ncount
sum = 0.
sum1 = 0.
sum2 = 0.
sum3 = 0.
sum4 = 0.
ncount = 0.
c = fs*df

Do 11 i = 1,npts
    sum = sum + vel(i)
    sum2 = sum2 + vel(i)/(c + vel(i))
    sum3 = sum3 + 1.0/(c + vel(i))
11 Continue

avg = sum/npts
avg2 = sum2/sum3
c
Do 12 i = 1, npts
    sum1 = sum1 + (vel(i)-avg)**2
    sum4 = sum4 + (vel(i)-avg2)**2/(c + vel(i))
c
12 Continue
c
stn = sqrt( sum1 / (npts-1) )
stn2 = sqrt(sum4/sum3)
c
return
end
c
c*****c
Subroutine Filter(U,Nsize,Um,rms)

Double Precision U(10000), UH, UL, rms, Um
Integer Nsize, Jsize
Jsize = 1
UH = Um + 2 * rms
UL = Um - 2 * rms
Do 10 i = 1,Nsize
    If ( U(i).GE. UL .AND. U(i).LE. UH ) Then
        U(Jsize) = U(i)
        Jsize = Jsize + 1
    Else
    Endif
10 Continue

Nsize = Jsize - 1
Return
End

```

APPENDIX E

ERROR ANALYSIS

Error by finite volume

Error is produced in the rms velocity measurement when a velocity gradient is present. This is due to the finite measurement volume of the LDA system. Given that the rms velocity is zero in an ideal flow, the affects of the mean velocity gradient is calculated.

$$U_j = \bar{U} \pm \frac{d\bar{U}}{dr} \delta_j d_m \quad (\delta \leq 1/2) \quad (E.1)$$

The product $\delta_j d_m$ represents the location of the velocity measurement in the control volume, where $\delta = 1/2$ is at the control volume edge and $\delta = 0$ is at the center. The control volume minor axis is given by d_m .

The definition of U_{rms} is,

$$U_{rms} = \left[\frac{\sum_{j=1}^N (U_j - \bar{U})^2}{N} \right]^{1/2} \quad (E.2)$$

Substituting Eq. (E.1) into Eq. (E.2), one obtains

$$U_{rms} = \frac{d\bar{U}}{dr} \bar{\delta} d_m \quad (E.3)$$

For even seeding throughout the measurement volume, $\bar{\delta} = 1/4$. The minor axis is 0.1316 mm and 0.2099 mm for the UI and WRDC LDA systems, respectively. The error is,

$$U_{\text{rms,error}} = 3.290 \times 10^{-5} \frac{d\bar{U}}{dr} \quad [\text{m/s}] \quad (\text{UI})$$

$$U_{\text{rms,error}} = 5.248 \times 10^{-5} \frac{d\bar{U}}{dr} \quad [\text{m/s}] \quad (\text{WRDC})$$

where $\frac{d\bar{U}}{dr}$ is in 1/s.

Error by LDA Resolution of TSI Counter

The measured frequency (f_m) from the PMT is composed of the Doppler frequency (f_d) and the frequency shift (f_s). The frequency shift is in the opposite direction of the mean flow. The equations relating the measured frequency to the percent error of the velocity measurement are as follows:

$$f_m = f_d + f_s \quad (\text{E.4})$$

$$f_d = \frac{N_b \times 10^9}{D_m \times 2^{n-2}} \quad (\text{E.5})$$

Combining Eqs. (E.4) and (E.5), one obtains

$$f_d = \frac{N_b \times 10^9}{D_m \times 2^{n-2}} - f_s \quad (\text{E.6})$$

For a LDA system, the velocity is calculated by

$$U = d_f f_d \quad (\text{E.7})$$

where d_f is the fringe spacing as defined in Appendix A. Combining Eq. (E.6) and Eq. (E.7), one obtains

$$U = df \left(\frac{N_b \times 10^9}{D_m \times 2^{n-2}} - f_s \right) \quad (E.8)$$

To calculate the percent error of the velocity produced by the TSI counter resolution, the following equations are used:

$$\% \text{ error} = \frac{U_1 - U_2}{U_1} \times 100 \quad (E.9)$$

where U_1 and U_2 is the velocity difference due to the counter which is an increment of D_m . Combining Eq. (E.8) into Eq. (E.9) and assuming the same exponent (n) and cycles per burst (N_b) for U_1 and U_2 , the equation reduces to the following:

$$\% \text{ error} = 1 - \frac{D_{m1}}{D_{m2}} \quad (E.10)$$

D_m will vary between 2048 and 4095 for an exponent value (n). This excludes when $n = 0$ where the mantissa (D_m) may go to 1, but this range is usually not used as in the case of this study. A D_m of 2047 at $n = 0$ corresponds to a velocity of 140 m/s, and 300 m/s for the experiments conducted at UI and WRDC, respectively. The maximum velocity error due to the counter resolution is at 2048 and 2049. The maximum velocity error of the component normal to the fringes is shown to be 0.05%, as calculated by Eq. (E.10).

The uncertainty of the frequency of the TSI counter was checked with a counter (HP Model 3312A) and signal generator (HP Model 5326A). The signal generator was set to 10 MHz according to the counter. Five thousand samples were taken with an rms value of 10^{-8} .

Repeatability in the hot (flame) zone

Measurements in the hot (flame) zone, $1.2 \leq r/R \leq 1.8$, were repeated using the sample size 3000. The velocities recorded were within 1% at all locations in the flame zone. Repositioning of the measurement volume and changing of experimental conditions to the same condition and placement increased the error to $\pm 3\%$ (points taken 1 or more days apart). Therefore, the uncertainty and error used for the measured velocities in the hot (flame) zone is $\pm 3\%$.

Error due to rotation of measured axis (radial component)

The mean radial component is calculated by,

$$\bar{V} = \bar{U}^+ \cos\theta - \bar{U}^- \sin\theta. \quad (\text{E.11})$$

The angle θ used in the present study is 45 degrees. Assuming $\pm 3\%$ is the error for each of the measured components, then from Eq. (E.11) the resolution for the mean radial velocity is

$$\bar{V}_{\text{resolution}} = \frac{\pm\sqrt{2}}{2} 0.03(\bar{U}^+ + \bar{U}^-). \quad (\text{E.12})$$

The error is calculated by,

$$\bar{V}_{\text{error}} = \frac{\bar{V}_{\text{resolution}}}{\bar{V}_{\text{calculated}}} \quad (\text{E.13})$$

The resolution and error are of interest in the hot (flame) zone, so an uncertainty may be calculated for the straining rates. The LDV data show that at the outer flame zone the sum

of the measured velocity components ($\bar{U}^+ + \bar{U}^-$) is 0.3 m/s, with a radial velocity of 0.074 m/s ($r/R = 1.8$). The maximum radial velocity location shows a measured velocity sum of 0.6 m/s with a maximum radial velocity of 0.4 m/s ($\bar{V}_{\text{calculated}}$) for the methane-argon Condition 2. The resolution at the outer hot (flame) zone location is calculated from Eq. (E.12); thus

$$\bar{V}_{\text{resolution}} = \pm 0.0064 \text{ m/s} \quad (\text{E.14})$$

which corresponds to an error of

$$\bar{V}_{\text{error}} = \pm 8.6 \%. \quad (\text{E.15})$$

At the maximum radial velocity location, the resolution and error are

$$\bar{V}_{\text{resolution}} = 0.0127 \text{ m/s}, \quad (\text{E.16})$$

$$\bar{V}_{\text{error}} = \pm 3.2\%. \quad (\text{E.17})$$

Uncertainty of Straining Rate Across Flame Zone

The uncertainty of the straining rate calculation is determined from the error at each end point of the linear equation representing the set of data points. The end points are calculated from the linear best fit equation and the error at each of the radial locations are included. Point 1 represents the maximum radial velocity location and point 2 the outer flame zone. The errors at locations 1 and 2 are given by Eqs. (E.14) and (E.16) for the methane-argon Condition 2 dilution.

The uncertainty of the straining rate (SR_{error}) is calculated by

$$SR_{\text{error}} = \frac{C1}{\frac{\bar{V}(r_2) - \bar{V}(r_1)}{r_2 - r_1}}$$

where $C1 = \pm \frac{\bar{V}(r_2) - \bar{V}(r_1)}{r_2 - r_1} .$

$$\frac{(\bar{V}(r_2) + \bar{V}_{\text{error}}(r_2) \bar{V}(r_2)) - (\bar{V}(r_1) - \bar{V}_{\text{error}}(r_1) \bar{V}(r_1))}{r_2 - r_1} . \quad (\text{E.18})$$

Equation (E.17) reduces to:

$$SR_{\text{error}} = \pm \frac{\bar{V}_{\text{error}}(r_2) \bar{V}(r_2) - \bar{V}_{\text{error}}(r_1) \bar{V}(r_1)}{\bar{V}(r_2) - \bar{V}(r_1)} . \quad (\text{E.19})$$

The errors of each condition were calculated as defined by Eqs. (E.12) and (E.13).

The calculation of the uncertainty of each straining rate was calculated as defined by Eq. (E.19).

APPENDIX F

LDA DATA

Methane Jet Data at Condition A (WRDC)

r/R	Radial Position (mm)	U_m (m/s)	U_{rms} (m/s)	V_m (m/s)	V_{rms} (m/s)
0.000	0.000	33.385	0.197	0.012	0.147
0.120	0.300	33.431	0.224	-0.019	0.147
0.240	0.600	33.474	0.210	-0.049	0.156
0.359	0.900	33.478	0.229	-0.109	0.159
0.479	1.200	33.599	0.226	-0.151	0.172
0.599	1.500	33.709	0.232	-0.177	0.162
0.719	1.800	33.739	0.230	-0.175	0.165
0.838	2.100	33.037	0.445	-0.177	0.160
0.958	2.400	23.825	3.778	-0.072	0.123
0.798	2.000	33.609	0.278	-0.184	0.149
0.838	2.100	33.220	0.412	-0.173	0.149
0.878	2.200	32.252	0.789	-0.167	0.147
0.918	2.300	29.112	2.061	-0.127	0.134
0.958	2.400	22.705	4.034	-0.058	0.114
0.998	2.500	17.335	2.712	-0.016	0.104

Methane Annulus Data at Condition A (WRDC)

r/R	Radial Position (mm)	U_m (m/s)	U_{rms} (m/s)	V_m (m/s)	V_{rms} (m/s)
1.277	3.200	0.197	0.117	-0.586	0.157
1.238	3.100	0.254	0.119	-0.649	0.134
1.198	3.000	0.299	0.126	-0.621	0.143
1.158	2.900	0.464	0.149	-0.589	0.115
1.118	2.800	0.887	0.295	-0.460	0.139
1.078	2.700	1.393	0.556	-0.323	0.149
1.038	2.600	4.077	1.456	-0.127	0.134
0.998	2.500	5.373	1.098	-0.052	0.139
0.958	2.400	4.802	1.509	-0.076	0.172
2.076	5.200	0.089	0.134	-0.092	0.117
2.874	7.200	0.044	0.107	-0.057	0.095
3.673	9.200	0.030	0.083	-0.034	0.074
4.471	11.200	0.021	0.081	-0.026	0.072

Methane Annulus Data Condition A (WRDC) Continued.

<u>r/R</u>	<u>Radial Position (mm)</u>	<u>U_m (m/s)</u>	<u>U_{rms} (m/s)</u>	<u>V_m (m/s)</u>	<u>V_{rms} (m/s)</u>
5.269	13.200	0.017	0.081	-0.014	0.072
6.068	15.200	0.010	0.079	-0.016	0.072
6.866	17.200	0.015	0.082	-0.024	0.072
7.665	19.200	0.009	0.079	-0.011	0.071
11.657	29.200	0.007	0.081	-0.010	0.073
15.649	39.200	0.011	0.085	-0.006	0.075
19.641	49.200	0.029	0.102	-0.019	0.092
23.633	59.200	0.058	0.089	-0.024	0.076
27.625	69.200	0.095	0.088	-0.031	0.079
31.617	79.200	0.134	0.082	-0.031	0.073
35.609	89.200	0.163	0.085	-0.026	0.074
39.601	99.200	0.192	0.086	-0.034	0.078
43.593	109.200	0.183	0.083	-0.035	0.076
-1.916	-4.800	0.072	0.088	0.093	0.078
-1.876	-4.700	0.073	0.086	0.095	0.076
-1.836	-4.600	0.075	0.089	0.101	0.076
-1.796	-4.500	0.083	0.088	0.113	0.076
-1.756	-4.400	0.086	0.089	0.116	0.078
-1.717	-4.300	0.089	0.089	0.131	0.076
-1.677	-4.200	0.087	0.093	0.137	0.080
-1.637	-4.100	0.085	0.089	0.160	0.079
-1.597	-4.000	0.092	0.091	0.177	0.076
-1.557	-3.900	0.097	0.090	0.185	0.079
-1.517	-3.800	0.096	0.090	0.219	0.082
-1.477	-3.700	0.095	0.093	0.255	0.086
-1.437	-3.600	0.099	0.095	0.283	0.091
-1.397	-3.500	0.111	0.092	0.356	0.100
-1.357	-3.400	0.138	0.092	0.425	0.102
-1.317	-3.300	0.164	0.093	0.463	0.113
-1.277	-3.200	0.196	0.093	0.515	0.113
-1.238	-3.100	0.240	0.096	0.523	0.108
-1.198	-3.000	0.296	0.109	0.540	0.108
-1.158	-2.900	0.368	0.121	0.544	0.107
-1.118	-2.800	0.590	0.190	0.416	0.125
-1.078	-2.700	1.192	0.407	0.242	0.140
-1.038	-2.600	2.064	0.850	0.129	0.139
-0.998	-2.500	4.828	1.235	0.008	0.126
-0.958	-2.400	5.658	1.211	0.056	0.107
9.800	24.550	0.103	0.087	-0.018	0.078
10.599	26.550	0.083	0.082	-0.028	0.072
11.397	28.550	0.056	0.087	-0.026	0.077
12.196	30.550	0.049	0.081	-0.024	0.075
12.994	32.550	0.048	0.085	-0.028	0.076
13.792	34.550	0.047	0.087	-0.023	0.077
14.591	36.550	0.053	0.085	-0.028	0.076
15.389	38.550	0.068	0.085	-0.038	0.074

Methane Annulus Data Condition A (WRDC) Continued.

<u>r/R</u>	<u>Radial Position (mm)</u>	<u>Um (m/s)</u>	<u>Urms (m/s)</u>	<u>Vm (m/s)</u>	<u>Vrms (m/s)</u>
16.188	40.550	0.048	0.087	-0.026	0.076
16.986	42.550	0.071	0.085	-0.034	0.077
17.784	44.550	0.060	0.086	-0.027	0.075
1.098	2.750	1.006	0.285	-0.384	0.179
1.138	2.850	0.585	0.205	-0.530	0.178
1.178	2.950	0.414	0.191	-0.609	0.183
1.218	3.050	0.332	0.196	-0.642	0.194
1.257	3.150	0.283	0.207	-0.648	0.203
1.297	3.250	0.197	0.192	-0.576	0.220
1.337	3.350	0.179	0.195	-0.532	0.215
1.377	3.450	0.194	0.188	-0.422	0.191
1.417	3.550	0.205	0.173	-0.337	0.166
1.457	3.650	0.219	0.162	-0.284	0.155
1.497	3.750	0.228	0.160	-0.245	0.147

Methane Jet Data at Condition B (WRDC)

<u>r/R</u>	<u>Radial Position (mm)</u>	<u>Um (m/s)</u>	<u>Urms (m/s)</u>	<u>Vm (m/s)</u>	<u>Vrms (m/s)</u>
0.000	0.000	28.184	0.181	0.007	0.128
0.200	0.500	28.199	0.181	-0.030	0.124
0.399	1.000	28.257	0.185	-0.067	0.125
0.599	1.500	28.458	0.198	-0.080	0.127
0.798	2.000	27.975	0.305	-0.119	0.136
0.998	2.500	14.492	2.879	0.013	0.093
0.798	2.000	28.246	0.248	-0.115	0.125
0.838	2.100	27.812	0.387	-0.128	0.141
0.878	2.200	26.649	0.767	-0.099	0.123
0.918	2.300	24.631	1.544	-0.067	0.121
0.958	2.400	20.627	2.851	-0.034	0.113
0.998	2.500	14.819	3.298	0.011	0.090
1.038	2.600	9.638	1.700	0.029	0.083

Methane Annulus Data at Condition B (WRDC)

r/R	Radial Position (mm)	U_m (m/s)	U_{rms} (m/s)	V_m (m/s)	V_{rms} (m/s)
9.980	25.000	0.161	0.080	-0.013	0.071
9.182	23.000	0.143	0.079	-0.009	0.070
8.383	21.000	0.149	0.079	-0.016	0.071
7.585	19.000	0.135	0.082	-0.014	0.074
6.786	17.000	0.118	0.077	-0.016	0.068
5.988	15.000	0.114	0.078	-0.017	0.069
5.190	13.000	0.114	0.077	-0.016	0.072
4.391	11.000	0.114	0.080	-0.020	0.070
3.593	9.000	0.114	0.080	-0.025	0.071
2.794	7.000	0.117	0.077	-0.031	0.070
1.996	5.000	0.152	0.078	-0.062	0.072
1.198	3.000	0.558	0.136	-0.667	0.087
1.996	5.000	0.152	0.079	-0.063	0.072
1.916	4.800	0.166	0.082	-0.072	0.073
1.836	4.600	0.185	0.078	-0.088	0.072
1.756	4.400	0.204	0.086	-0.112	0.077
1.677	4.200	0.239	0.085	-0.142	0.080
1.597	4.000	0.272	0.085	-0.174	0.079
1.517	3.800	0.310	0.097	-0.230	0.099
1.437	3.600	0.319	0.108	-0.321	0.122
1.357	3.400	0.307	0.114	-0.505	0.172
1.277	3.200	0.350	0.106	-0.713	0.091
1.198	3.000	0.560	0.128	-0.638	0.086
1.118	2.800	1.070	0.295	-0.392	0.126
1.038	2.600	2.782	1.136	-0.132	0.104
0.958	2.400	4.047	1.322	-0.064	0.083
9.980	25.000	0.185	0.081	-0.012	0.071
13.972	35.000	0.190	0.079	-0.008	0.073
17.964	45.000	0.185	0.079	-0.006	0.071
21.956	55.000	0.197	0.077	-0.007	0.069
25.948	65.000	0.200	0.077	-0.005	0.072
29.940	75.000	0.210	0.077	-0.002	0.068
33.932	85.000	0.195	0.079	-0.004	0.071
37.924	95.000	0.198	0.081	-0.004	0.072
41.916	105.000	0.216	0.082	-0.004	0.073
45.908	115.000	0.240	0.083	-0.006	0.074

Methane Jet Data at Condition C (WRDC)

<u>r/R</u>	<u>Radial Position (mm)</u>	<u>Um (m/s)</u>	<u>Urms (m/s)</u>	<u>Vm (m/s)</u>	<u>Vrms (m/s)</u>
0.000	0.000	24.324	0.142	0.019	0.089
0.200	0.500	24.321	0.151	-0.019	0.097
0.399	1.000	24.368	0.159	-0.048	0.098
0.599	1.500	24.506	0.166	-0.073	0.105
0.798	2.000	24.210	0.229	-0.082	0.111
0.998	2.500	13.200	2.635	0.021	0.091
0.798	2.000	24.372	0.238	-0.087	0.115
0.838	2.100	23.966	0.355	-0.078	0.111
0.878	2.200	23.270	0.572	-0.077	0.110
0.918	2.300	21.459	1.189	-0.064	0.108
0.958	2.400	18.454	2.205	-0.030	0.100
0.998	2.500	13.234	2.595	0.026	0.092
1.038	2.600	9.231	1.630	0.054	0.088

Methane Annulus Data at Condition C (WRDC)

<u>r/R</u>	<u>Radial Position (mm)</u>	<u>Um (m/s)</u>	<u>Urms (m/s)</u>	<u>Vm (m/s)</u>	<u>Vrms (m/s)</u>
1.996	5.000	0.203	0.086	-0.065	0.079
5.988	15.000	0.300	0.087	-0.019	0.077
9.980	25.000	0.302	0.088	-0.014	0.078
13.972	35.000	0.303	0.088	-0.013	0.080
17.964	45.000	0.325	0.087	-0.009	0.080
21.956	55.000	0.354	0.089	-0.005	0.079
25.948	65.000	0.368	0.088	-0.004	0.079
29.940	75.000	0.340	0.086	-0.007	0.077
33.932	85.000	0.285	0.087	-0.004	0.076
37.924	95.000	0.292	0.087	-0.004	0.077
41.916	105.000	0.357	0.089	-0.006	0.080
45.908	115.000	0.391	0.088	-0.001	0.079
1.996	5.000	0.181	0.082	-0.048	0.073
1.916	4.800	0.199	0.081	-0.068	0.071
1.836	4.600	0.225	0.082	-0.085	0.073
1.756	4.400	0.257	0.086	-0.109	0.079
1.677	4.200	0.301	0.088	-0.152	0.082
1.597	4.000	0.350	0.094	-0.177	0.091
1.517	3.800	0.381	0.108	-0.249	0.117
1.437	3.600	0.384	0.120	-0.376	0.142
1.357	3.400	0.398	0.121	-0.614	0.169
1.277	3.200	0.482	0.100	-0.717	0.081
1.198	3.000	0.680	0.136	-0.612	0.091

Methane Annulus Data Condition C (WRDC) Continued.

r/R	Radial Position (mm)	U_m (m/s)	U_{rms} (m/s)	V_m (m/s)	V_{rms} (m/s)
1.118	2.800	1.444	0.332	-0.296	0.126
1.038	2.600	2.987	0.956	-0.092	0.104
0.958	2.400	3.717	0.955	-0.036	0.092
9.980	25.000	0.303	0.085	-0.010	0.075
9.182	23.000	0.315	0.078	-0.013	0.072
8.383	21.000	0.324	0.084	-0.017	0.077
7.585	19.000	0.347	0.085	-0.054	0.075
8.383	21.000	0.321	0.082	-0.013	0.076
7.585	19.000	0.322	0.085	-0.016	0.075
6.786	17.000	0.318	0.083	-0.018	0.075
5.988	15.000	0.298	0.086	-0.020	0.075
5.190	13.000	0.269	0.087	-0.020	0.076
4.391	11.000	0.236	0.084	-0.022	0.076
3.593	9.000	0.202	0.085	-0.025	0.075
2.794	7.000	0.174	0.084	-0.026	0.076
1.996	5.000	0.199	0.084	-0.059	0.075

Lifted Methane Jet Data at Condition B (WRDC)

r/R	Radial Position (mm)	U_m (m/s)	U_{rms} (m/s)	V_m (m/s)	V_{rms} (m/s)
0.000	0.000	30.447	0.190	0.087	0.133
0.200	0.500	30.440	0.174	0.014	0.136
0.399	1.000	30.454	0.179	-0.066	0.156
0.599	1.500	30.623	0.192	-0.083	0.160
0.798	2.000	30.401	0.231	-0.113	0.134
0.998	2.500	15.256	3.562	0.009	0.099
0.798	2.000	30.500	0.231	-0.111	0.137
0.838	2.100	30.228	0.334	-0.110	0.131
0.878	2.200	29.512	0.577	-0.108	0.134
0.918	2.300	26.963	1.611	-0.072	0.132
0.958	2.400	23.394	2.879	-0.031	0.124
0.998	2.500	14.939	3.485	0.003	0.094
1.038	2.600	10.621	2.071	0.010	0.094

Lifted Methane Annulus Data at Condition B (WRDC)

<u>r/R</u>	<u>Radial Position (mm)</u>	<u>Um (m/s)</u>	<u>Urms (m/s)</u>	<u>Vm (m/s)</u>	<u>Vrms (m/s)</u>
9.980	25.000	0.211	0.078	-0.043	0.068
9.182	23.000	0.216	0.078	-0.044	0.070
8.383	21.000	0.221	0.081	-0.047	0.071
7.585	19.000	0.224	0.078	-0.050	0.069
6.786	17.000	0.231	0.079	-0.059	0.070
5.988	15.000	0.234	0.080	-0.064	0.070
5.190	13.000	0.251	0.079	-0.069	0.072
4.391	11.000	0.255	0.084	-0.079	0.073
3.593	9.000	0.287	0.080	-0.087	0.068
2.794	7.000	0.311	0.083	-0.097	0.072
1.996	5.000	0.341	0.084	-0.103	0.076
1.198	3.000	0.297	0.083	-0.152	0.072

Argon Annulus Data (UI)

<u>Radial Position (mm)</u>	<u>r/R</u>	<u>Um (m/s)</u>	<u>Vm (m/s)</u>	<u>Urms (m/s)</u>	<u>Vrms (m/s)</u>
2.900	1.242	0.423	-0.231	0.128	0.054
5.900	2.527	0.277	-0.097	0.023	0.030
10.400	4.454	0.248	-0.079	0.029	0.037
20.400	8.737	0.225	-0.058	0.026	0.026
30.400	13.019	0.211	-0.045	0.029	0.024
50.400	21.585	0.223	-0.022	0.026	0.027
70.400	30.150	0.222	-0.005	0.027	0.022
90.400	38.715	0.217	-0.010	0.027	0.024
110.400	47.281	0.243	-0.012	0.025	0.035
2.400	1.028	3.701	-0.384	1.062	0.141

Argon Jet Data (UI)

Radial Position (mm)	r/R	U_m (m/s)	V_m (m/s)	U_{rms} (m/s)	V_{rms} (m/s)
0.400	0.171	19.874	0.003	0.201	0.072
0.900	0.385	19.889	0.042	0.217	0.059
1.400	0.600	19.865	-0.022	0.183	0.089
1.900	0.814	19.067	-0.218	0.530	0.369
2.300	0.985	8.390	-0.280	1.557	0.972
2.300	0.985	10.455	-0.607	2.497	1.127
2.100	0.899	16.737	-0.672	1.328	0.543
-0.100	-0.043	19.897	-0.030	0.198	0.064
-0.600	-0.257	19.895	0.007	0.197	0.089
-1.100	-0.471	19.873	0.002	0.193	0.068
-1.600	-0.685	19.791	0.093	0.199	0.076
-2.100	-0.899	17.600	0.280	1.075	0.684
-2.300	-0.985	7.819	1.066	1.201	0.155
0.900	0.385	19.967	0.066	0.193	0.102

Methane/Argon Annulus Data Condition 1 (UI)

r/R	Radial Position (mm)	U_m (m/s)	V_m (m/s)	U_{rms} (m/s)	V_{rms} (m/s)
2.141	5.000	0.173	-0.079	0.029	0.036
1.713	4.000	0.287	-0.222	0.039	0.038
1.670	3.900	0.280	-0.255	0.037	0.049
1.627	3.800	0.338	-0.265	0.047	0.042
1.585	3.700	0.347	-0.296	0.038	0.053
1.542	3.600	0.372	-0.319	0.054	0.030
1.520	3.550	0.391	-0.329	0.042	0.058
1.456	3.400	0.458	-0.385	0.051	0.072
1.413	3.300	0.472	-0.457	0.054	0.070
1.370	3.200	0.506	-0.525	0.084	0.009
1.842	4.300	0.200	-0.138	0.037	0.039
42.912	100.200	0.208	0.003	0.023	0.028
21.499	50.200	0.215	-0.011	0.024	0.026
8.651	20.200	0.176	-0.017	0.023	0.024
4.368	10.200	0.146	-0.026	0.022	0.029
1.456	3.400	0.404	-0.414	0.059	0.046
1.071	2.500	3.205	-0.277	0.642	0.249
1.242	2.900	0.859	-0.411	0.187	0.114
0.985	2.300	3.956	-0.080	0.556	0.256
1.028	2.400	3.662	-0.019	0.641	0.208
1.156	2.700	1.319	-0.354	0.239	0.101
1.370	3.200	0.503	-0.551	0.066	0.009

Methane/Argon Annulus Data at Condition 1 Continued

r/R	Radial Position (mm)	U_m (m/s)	V_m (m/s)	U_{rms} (m/s)	V_{rms} (m/s)
1.456	3.400	0.403	-0.407	0.127	0.025
1.585	3.700	0.319	-0.299	0.042	0.031
1.328	3.100	0.614	-0.544	0.065	0.040
1.285	3.000	0.724	-0.546	0.091	0.029

Methane/Argon Annulus Data at Condition 2 (UI)

r/R	Radial Position (mm)	U_m (m/s)	V_m (m/s)	U_{rms} (m/s)	V_{rms} (m/s)
0.985	2.300	2.599	-0.082	0.277	0.064
42.955	100.300	0.225	0.005	0.030	0.041
21.542	50.300	0.215	-0.007	0.030	0.040
8.694	20.300	0.170	-0.011	0.031	0.037
4.411	10.300	0.150	-0.024	0.032	0.036
2.270	5.300	0.157	-0.040	0.028	0.038
1.842	4.300	0.271	-0.117	0.043	0.021
1.627	3.800	0.350	-0.180	0.061	0.051
1.328	3.100	0.642	-0.336	0.167	0.174
1.413	3.300	0.520	-0.337	0.125	0.087
1.499	3.500	0.404	-0.172	0.074	0.073
1.028	2.400	2.636	0.003	0.236	0.017
1.113	2.600	1.591	-0.166	0.219	0.275
1.199	2.800	0.989	-0.167	0.145	0.122
1.627	3.800	0.349	-0.189	0.072	0.020
1.970	4.600	0.216	-0.074	0.037	0.043
1.756	4.100	0.267	-0.115	0.041	0.052
1.713	4.000	0.288	-0.135	0.036	0.051
1.670	3.900	0.302	-0.165	0.042	0.048
1.627	3.800	0.328	-0.175	0.053	0.071
1.585	3.700	0.336	-0.183	0.044	0.056
1.542	3.600	0.371	-0.202	0.051	0.066
1.499	3.500	0.411	-0.193	0.078	0.081
1.456	3.400	0.504	-0.251	0.073	0.132

Methane Jet Data at Condition 0 (UI)

r/R	Radial Position (mm)	U_m (m/s)	V_m (m/s)	U_{rms} (m/s)	V_{rms} (m/s)
0.000	0.000	23.935	-0.017	0.224	0.112
0.214	0.500	24.010	-0.094	0.229	0.134
0.428	1.000	24.131	-0.063	0.230	0.137
0.642	1.500	24.030	-0.152	0.199	0.101
0.857	2.000	22.630	-0.385	0.582	0.272
0.985	2.300	11.966	-1.297	2.483	0.886
0.942	2.200	16.036	-1.107	2.104	0.476
-0.214	-0.500	24.123	0.115	0.209	0.100
-0.428	-1.000	24.142	0.048	0.202	0.095
-0.642	-1.500	24.150	0.069	0.202	0.117
-0.857	-2.000	23.192	0.253	0.370	0.281
-0.942	-2.200	17.833	0.854	2.000	0.671
-0.985	-2.300	13.235	0.668	2.496	0.760

Methane Annulus Data at Condition 0 (UI)

r/R	Radial Position (mm)	U_m (m/s)	V_m (m/s)	U_{rms} (m/s)	V_{rms} (m/s)
2.146	5.000	0.185	-0.079	0.027	0.030
1.717	4.000	0.295	-0.292	0.034	0.042
1.674	3.900	0.333	-0.327	0.039	0.037
1.631	3.800	0.339	-0.353	0.039	0.042
1.588	3.700	0.374	-0.394	0.039	0.043
1.545	3.600	0.414	-0.419	0.043	0.041
1.502	3.500	0.424	-0.467	0.042	0.050
1.459	3.400	0.470	-0.522	0.044	0.062
1.416	3.300	0.526	-0.619	0.047	0.042
1.373	3.200	0.577	-0.651	0.049	0.033
1.288	3.000	0.782	-0.623	0.072	0.040
1.285	3.000	0.658	-0.665	0.050	0.020
8.565	20.000	0.133	-0.014	0.025	0.030
12.848	30.000	0.156	-0.009	0.022	0.027
21.413	50.000	0.195	-0.007	0.023	0.023
29.979	70.000	0.222	-0.009	0.026	0.022
38.544	90.000	0.212	0.000	0.024	0.021
47.109	110.000	0.259	-0.015	0.022	0.030
2.141	5.000	0.156	-0.072	0.023	0.027
1.285	3.000	0.639	-0.647	0.045	0.030
4.283	10.000	0.137	-0.022	0.024	0.028
1.071	2.500	4.138	-0.386	0.769	0.272
0.985	2.300	5.555	-0.053	0.635	0.395

Methane Annulus Data at Condition 0 (UI) Continued.

<u>r/R</u>	<u>Radial Position (mm)</u>	<u>Um (m/s)</u>	<u>Vm (m/s)</u>	<u>Urms (m/s)</u>	<u>Vrms (m/s)</u>
0.942	2.200	5.572	-0.004	0.666	0.270
1.156	2.700	1.473	-0.495	0.183	0.079
1.413	3.300	0.484	-0.633	0.037	0.046
1.713	4.000	0.264	-0.275	0.023	0.036

Lifted Methane Jet Data at Condition 0 (UI)

<u>r/R</u>	<u>Radial Position (mm)</u>	<u>Um (m/s)</u>	<u>Vm (m/s)</u>	<u>Urms (m/s)</u>	<u>Vrms (m/s)</u>
0.000	0.000	23.996	-0.011	0.214	0.103
0.214	0.500	24.114	-0.055	0.200	0.069
0.428	1.000	24.099	-0.035	0.208	0.102
0.642	1.500	24.096	-0.004	0.166	0.071
0.857	2.000	21.319	-0.662	1.137	0.760
0.985	2.300	8.254	-0.526	1.302	0.385
0.942	2.200	13.422	-1.398	3.017	1.420
-0.214	-0.500	24.126	0.031	0.204	0.066
-0.428	-1.000	24.097	0.145	0.197	0.046
-0.642	-1.500	24.123	0.201	0.175	0.051
-0.857	-2.000	23.147	0.337	0.446	0.274
-0.942	-2.200	19.319	0.414	2.077	0.494
-0.985	-2.300	11.759	1.752	2.757	1.118

Lifted Methane Annulus Data at Condition 0 (UI)

<u>r/R</u>	<u>Radial Position (mm)</u>	<u>Um (m/s)</u>	<u>Vm (m/s)</u>	<u>Urms (m/s)</u>	<u>Vrms (m/s)</u>
0.985	2.300	3.936	-0.439	1.252	0.326
1.028	2.400	2.868	-0.677	1.216	0.535
1.071	2.500	1.005	-0.293	0.450	0.134
1.156	2.700	0.306	-0.164	0.058	0.037
1.285	3.000	0.254	-0.147	0.026	0.032
1.413	3.300	0.264	-0.145	0.023	0.032
1.713	4.000	0.283	-0.121	0.022	0.026
2.141	5.000	0.291	-0.115	0.022	0.025
12.848	30.000	0.189	-0.042	0.022	0.024
21.413	50.000	0.205	-0.019	0.022	0.024
29.979	70.000	0.214	-0.006	0.023	0.024
38.544	90.000	0.224	0.000	0.023	0.022
47.109	110.000	0.229	-0.003	0.023	0.027
4.283	10.000	0.243	-0.097	0.023	0.028
8.565	20.000	0.197	-0.059	0.024	0.028

Methane/Helium Annulus Data at Condition 1 (UI)

<u>r/R</u>	<u>Radial Position (mm)</u>	<u>Um (m/s)</u>	<u>Vm (m/s)</u>	<u>Urms (m/s)</u>	<u>Vrms (m/s)</u>
42.698	99.700	0.228	0.005	0.030	0.035
21.285	49.700	0.216	-0.011	0.033	0.033
8.437	19.700	0.173	-0.016	0.031	0.037
4.154	9.700	0.150	-0.031	0.031	0.036
2.013	4.700	0.237	-0.115	0.034	0.036
1.585	3.700	0.392	-0.398	0.038	0.041
1.499	3.500	0.463	-0.497	0.046	0.061
1.413	3.300	0.533	-0.597	0.040	0.046
1.328	3.100	0.649	-0.604	0.051	0.042
1.242	2.900	0.912	-0.534	0.092	0.021
1.156	2.700	1.546	-0.415	0.183	0.059
1.071	2.500	2.761	-0.378	0.398	0.092
0.985	2.300	5.295	-0.002	0.514	0.223
1.627	3.800	0.362	-0.343	0.038	0.044
1.263	2.950	0.900	-0.519	0.086	0.072
1.285	3.000	0.831	-0.559	0.075	0.050
1.306	3.050	0.773	-0.559	0.058	0.049
1.349	3.150	0.682	-0.587	0.052	0.044
1.370	3.200	0.640	-0.603	0.049	0.034
1.392	3.250	0.594	-0.613	0.044	0.041
1.413	3.300	0.568	-0.605	0.044	0.037

Methane/Helium Annulus Data at Condition 1 (UI) Continued

<u>r/R</u>	<u>Radial Position (mm)</u>	<u>Um (m/s)</u>	<u>Vm (m/s)</u>	<u>Urms (m/s)</u>	<u>Vrms (m/s)</u>
1.456	3.400	0.529	-0.579	0.043	0.046
1.542	3.600	0.435	-0.475	0.037	0.066
1.627	3.800	0.388	-0.379	0.033	0.051
1.670	3.900	0.339	-0.326	0.035	0.046
1.713	4.000	0.329	-0.303	0.036	0.047

Methane/Helium Annulus Data at Condition 2 (UI)

<u>r/R</u>	<u>Radial Position (mm)</u>	<u>Um (m/s)</u>	<u>Vm (m/s)</u>	<u>Urms (m/s)</u>	<u>Vrms (m/s)</u>
42.698	99.700	0.228	0.005	0.030	0.035
21.285	49.700	0.216	-0.011	0.033	0.033
8.437	19.700	0.173	-0.016	0.031	0.037
4.154	9.700	0.150	-0.031	0.031	0.036
2.013	4.700	0.237	-0.115	0.034	0.036
1.585	3.700	0.392	-0.398	0.038	0.041
1.499	3.500	0.463	-0.497	0.046	0.061
1.413	3.300	0.533	-0.597	0.040	0.046
1.328	3.100	0.649	-0.604	0.051	0.042
1.242	2.900	0.912	-0.534	0.092	0.021
1.156	2.700	1.546	-0.415	0.183	0.059
1.071	2.500	2.761	-0.378	0.398	0.092
0.985	2.300	5.295	-0.002	0.514	0.223
1.627	3.800	0.362	-0.343	0.038	0.044
1.263	2.950	0.900	-0.519	0.086	0.072
1.285	3.000	0.831	-0.559	0.075	0.050
1.306	3.050	0.773	-0.559	0.058	0.049
1.349	3.150	0.682	-0.587	0.052	0.044
1.370	3.200	0.640	-0.603	0.049	0.034
1.392	3.250	0.594	-0.613	0.044	0.041
1.413	3.300	0.568	-0.605	0.044	0.037
1.456	3.400	0.529	-0.579	0.043	0.046
1.542	3.600	0.435	-0.475	0.037	0.066
1.627	3.800	0.388	-0.379	0.033	0.051
1.670	3.900	0.339	-0.326	0.035	0.046
1.713	4.000	0.329	-0.303	0.036	0.047

Methane/Helium Jet Data at Condition 1 (UI)

<u>r/R</u>	<u>Radial Position (mm)</u>	<u>Um (m/s)</u>	<u>Vm (m/s)</u>	<u>Urms (m/s)</u>	<u>Vrms (m/s)</u>
0.000	0.000	21.507	-0.052	0.234	0.084
0.343	0.800	21.510	-0.090	0.195	0.134
0.771	1.800	21.087	-0.182	0.237	0.052
0.985	2.300	11.467	-1.259	2.195	1.120
1.006	2.350	8.161	-0.518	1.182	0.548
0.942	2.200	15.644	-1.041	1.648	0.530
-0.514	-1.200	21.487	0.025	0.178	0.133
-0.942	-2.200	15.712	0.759	1.659	0.769
-0.985	-2.300	11.486	1.105	1.879	0.403
-1.028	-2.400	8.039	0.500	0.998	0.076

Methane/Argon Jet Data at Condition 1 (UI)

<u>r/R</u>	<u>Radial Position (mm)</u>	<u>Um (m/s)</u>	<u>Vm (m/s)</u>	<u>Urms (m/s)</u>	<u>Vrms (m/s)</u>
0.128	0.300	17.206	0.005	0.174	0.089
0.343	0.800	17.154	-0.016	0.175	0.064
0.557	1.300	17.147	-0.070	0.156	0.098
0.771	1.800	16.458	-0.202	0.560	0.271
0.985	2.300	7.009	-0.253	1.312	0.657
0.942	2.200	10.557	-0.547	1.940	0.407
0.857	2.000	14.884	-0.598	1.199	0.732

Methane/Argon Jet Data at Condition 2 (UI)

<u>r/R</u>	<u>Radial Position (mm)</u>	<u>Um (m/s)</u>	<u>Vm (m/s)</u>	<u>Urms (m/s)</u>	<u>Vrms (m/s)</u>
-0.728	-1.700	9.630	0.083	0.381	0.161
-0.300	-0.700	10.621	0.045	0.095	0.025
0.128	0.300	10.641	0.008	0.101	0.014
0.557	1.300	10.576	-0.059	0.092	0.032
0.771	1.800	10.310	-0.106	0.147	0.119
0.985	2.300	7.007	-0.333	0.970	0.277
1.071	2.500	4.158	-0.094	0.666	0.289
1.028	2.400	5.287	-0.236	1.003	0.411
-0.814	-1.900	8.214	0.139	0.777	0.240
-0.857	-2.000	6.645	0.179	1.020	0.295
-0.899	-2.100	5.509	0.262	1.000	0.167
-0.942	-2.200	4.093	0.222	0.646	0.279
1.071	2.500	4.389	-0.188	0.813	0.406

Methane Annulus Data at Condition C (UI)

r/R	Radial Position (mm)	U_m (m/s)	U_{rms} (m/s)	V_m (m/s)	V_{rms} (m/s)
4.069	9.500	-----	-----	-0.052	0.022
1.927	4.500	-----	-----	-0.182	0.031
1.585	3.700	-----	-----	-0.413	0.030
1.542	3.600	-----	-----	-0.438	0.049
1.499	3.500	-----	-----	-0.517	0.047
1.456	3.400	-----	-----	-0.559	0.038
1.413	3.300	-----	-----	-0.612	0.036
1.370	3.200	-----	-----	-0.627	0.034
1.328	3.100	-----	-----	-0.613	0.035
1.285	3.000	-----	-----	-0.591	0.036
1.242	2.900	-----	-----	-0.551	0.034
1.199	2.800	-----	-----	-0.504	0.038
1.156	2.700	-----	-----	-0.467	0.044
1.071	2.500	-----	-----	-0.303	0.063
1.627	3.800	-----	-----	-0.383	0.037
1.670	3.900	-----	-----	-0.357	0.036

Methane Annulus Data at Condition A+ (UI)

r/R	Radial Position (mm)	U_m (m/s)	U_{rms} (m/s)	V_m (m/s)	V_{rms} (m/s)
1.756	4.100	-----	-----	-0.217	0.047
1.542	3.600	-----	-----	-0.369	0.053
1.499	3.500	-----	-----	-0.435	0.053
1.456	3.400	-----	-----	-0.437	0.056
1.413	3.300	-----	-----	-0.546	0.085
1.370	3.200	-----	-----	-0.555	0.098
1.328	3.100	-----	-----	-0.600	0.093
1.285	3.000	-----	-----	-0.696	0.039
1.242	2.900	-----	-----	-0.654	0.046
1.199	2.800	-----	-----	-0.618	0.048
1.156	2.700	-----	-----	-0.552	0.050
1.113	2.600	-----	-----	-0.451	0.069
1.071	2.500	-----	-----	-0.215	0.091
1.028	2.400	-----	-----	-0.109	0.072
0.985	2.300	-----	-----	-0.059	0.051
0.899	2.100	-----	-----	-0.060	0.047
1.199	2.800	-----	-----	-0.607	0.051
1.585	3.700	-----	-----	-0.362	0.038
1.627	3.800	-----	-----	-0.321	0.041
1.670	3.900	-----	-----	-0.289	0.041
1.713	4.000	-----	-----	-0.269	0.040
1.542	3.600	-----	-----	-0.395	0.044

Methane Annulus Data at Condition A (UI)

<u>r/R</u>	Radial Position (mm)	U _m (m/s)	U _{rms} (m/s)	V _m (m/s)	V _{rms} (m/s)
1.927	4.500	-----	-----	-0.161	0.030
1.842	4.300	-----	-----	-0.167	0.038
1.756	4.100	-----	-----	-0.211	0.040
1.713	4.000	-----	-----	-0.251	0.043
1.670	3.900	-----	-----	-0.243	0.046
1.627	3.800	-----	-----	-0.286	0.051
1.585	3.700	-----	-----	-0.353	0.061
1.542	3.600	-----	-----	-0.372	0.054
1.499	3.500	-----	-----	-0.439	0.050
1.456	3.400	-----	-----	-0.406	0.060
1.413	3.300	-----	-----	-0.450	0.058
1.370	3.200	-----	-----	-0.526	0.089
1.328	3.100	-----	-----	-0.572	0.093
1.242	2.900	-----	-----	-0.676	0.048
1.199	2.800	-----	-----	-0.598	0.059
1.156	2.700	-----	-----	-0.504	0.064
1.071	2.500	-----	-----	-0.187	0.076

Methane Annulus Data at Condition B (UI)

<u>r/R</u>	Radial Position (mm)	U _m (m/s)	U _{rms} (m/s)	V _m (m/s)	V _{rms} (m/s)
1.927	4.500	-----	-----	-0.178	0.031
1.842	4.300	-----	-----	-0.202	0.027
1.756	4.100	-----	-----	-0.285	0.033
1.713	4.000	-----	-----	-0.311	0.030
1.670	3.900	-----	-----	-0.355	0.043
1.627	3.800	-----	-----	-0.373	0.034
1.585	3.700	-----	-----	-0.404	0.040
1.542	3.600	-----	-----	-0.440	0.035
1.499	3.500	-----	-----	-0.519	0.061
1.456	3.400	-----	-----	-0.530	0.050
1.413	3.300	-----	-----	-0.624	0.046
1.370	3.200	-----	-----	-0.655	0.031
1.328	3.100	-----	-----	-0.654	0.033
1.242	2.900	-----	-----	-0.555	0.037
1.199	2.800	-----	-----	-0.461	0.043
1.156	2.700	-----	-----	-0.393	0.055

Argon jet cond. B x/d=6 (UI)

Radial Position (mm)	r/R	U_m (m/s)	V_m (m/s)	U_{rms} (m/s)	V_{rms} (m/s)
0.000	0.000	16.357	0.176	2.550	2.104
2.000	0.857	11.037	0.700	3.168	2.749
4.000	1.713	6.079	0.762	2.688	2.106
6.000	2.570	2.658	0.392	1.952	1.624
7.500	3.212	0.996	0.202	1.218	1.396
-2.000	-0.857	16.305	-0.956	2.714	2.393
-4.000	-1.713	10.059	-1.084	3.225	2.747
-6.000	-2.570	5.209	-0.746	2.451	2.079
-7.500	-3.212	2.363	-0.289	1.730	1.490

APPENDIX G

STABILITY CURVE DATA

Contoured Nozzle (WRDC)
Methane/Nitrogen

Condition A		Condition B		Condition C	
Mass fraction	Lift-off velocity (m/s)	Mass fraction	Lift-off velocity (m/s)	Mass fraction	Lift-off velocity (m/s)
1.000	32.480	1.000	29.310	1.000	28.490
0.928	30.900	0.895	25.900	0.901	25.810
0.833	27.070	0.794	22.140	0.791	22.210
0.746	23.040	0.688	18.510	0.672	18.810
0.660	19.030	0.594	14.940	0.573	15.310
0.582	15.160	0.505	11.360	0.476	11.880
0.501	11.440	0.453	9.980	0.425	10.480
0.452	10.010	0.378	7.790	0.353	8.210
0.374	7.850	0.292	4.970	0.275	5.230
0.297	4.900	0.346	5.030	0.314	5.440
0.343	5.070	0.308	4.060	0.279	4.390
0.312	4.020	0.264	2.610	0.247	2.770
0.264	2.610				

Contoured Nozzle (WRDC)
Methane/Argon

Condition A		Condition B		Condition C	
Mass fraction	Lift-off velocity (m/s)	Mass fraction	Lift-off velocity (m/s)	Mass fraction	Lift-off velocity (m/s)
1.000	32.480	1.000	29.310	1.000	28.490
0.890	31.050	0.848	26.020	0.863	25.830
0.767	27.230	0.748	21.900	0.719	22.310
0.664	23.190	0.618	18.340	0.565	19.240
0.540	19.720	0.472	15.540	0.441	16.180
0.446	16.080	0.375	12.150	0.347	12.780
0.365	12.360	0.320	10.920	0.301	11.400
0.320	10.920	0.255	8.710	0.235	9.240
0.257	8.660	0.185	5.770	0.167	6.250
0.191	5.600	0.234	5.580	0.214	5.960

Continued

Condition A		Condition B		Condition C	
Mass fraction	Lift-off velocity (m/s)	Mass fraction	Lift-off velocity (m/s)	Mass fraction	Lift-off velocity (m/s)
0.237	5.530	0.207	4.510	0.190	4.800
0.210	4.460	0.164	3.050	0.153	3.240
0.167	3.020				

Contoured Nozzle (WRDC)
Methane/Helium

Condition A		Condition B		Condition C	
Mass fraction	Lift-off velocity (m/s)	Mass fraction	Lift-off velocity (m/s)	Mass fraction	Lift-off velocity (m/s)
1.000	32.480	1.000	29.310	1.000	28.490
0.988	31.010	0.991	25.150	0.988	25.470
0.980	26.220	0.979	20.950	0.975	21.230
0.972	21.540	0.966	16.780	0.959	17.220
0.961	17.090	0.948	13.080	0.940	13.500
0.948	13.080	0.932	9.410	0.919	9.850
0.935	9.320	0.915	8.120	0.902	8.470
0.916	8.070	0.897	5.860	0.879	6.220
0.897	5.860	0.863	3.410	0.834	3.740
0.858	3.460	0.879	3.750	0.868	3.890
0.887	3.650	0.876	2.780	0.847	3.060
0.866	2.870	0.853	1.700	0.800	2.010
0.845	1.750				

Tapered Nozzle (WRDC)
Methane/Argon

Condition A		Condition B		Condition C	
Mass fraction	Lift-off velocity (m/s)	Mass fraction	Lift-off velocity (m/s)	Mass fraction	Lift-off velocity (m/s)
1.000	31.390	1.000	23.700	1.000	19.480
0.740	26.260	0.740	18.840	0.909	17.170
0.570	21.490	0.524	14.750	0.613	13.560
0.439	16.340	0.318	9.400	0.362	8.620
0.293	9.940	0.255	7.460	0.278	7.000
0.242	7.730	0.218	5.040	0.229	4.850
0.213	5.130	0.225	3.610	0.237	3.480
0.218	3.710	0.176	1.940	0.178	1.790
0.174	1.960	0.148	0.990	0.157	0.970
0.142	0.940				

**Tapered Nozzle (WRDC)
Methane/Nitrogen**

Condition A		Condition B		Condition C	
Mass fraction	Lift-off velocity (m/s)	Mass fraction	Lift-off velocity (m/s)	Mass fraction	Lift-off velocity (m/s)
1.000	31.390	1.000	23.700	1.000	19.480
0.816	25.970	0.802	18.850	0.908	17.470
0.673	21.090	0.622	14.580	0.694	13.540
0.547	15.930	0.421	9.040	0.469	8.330
0.396	9.470	0.360	6.930	0.383	6.600
0.333	7.360	0.321	4.570	0.371	4.070
0.312	4.680	0.334	3.250	0.376	2.960
0.334	3.250	0.306	1.530	0.296	1.440
0.282	1.590	0.257	0.820	0.270	0.790
0.273	0.740				

**Tapered Nozzle (WRDC)
Methane/Helium**

Condition A		Condition B		Condition C	
Mass fraction	Lift-off velocity (m/s)	Mass fraction	Lift-off velocity (m/s)	Mass fraction	Lift-off velocity (m/s)
1.000	31.390	1.000	23.700	1.000	19.480
0.979	24.980	0.979	17.890	0.992	17.070
0.965	18.880	0.957	12.790	0.967	12.320
0.948	13.220	0.916	6.910	0.926	6.680
0.908	7.100	0.895	5.050	0.909	4.820
0.892	5.090	0.894	3.050	0.902	2.970
0.883	3.170	0.901	2.190	0.906	2.150
0.901	2.190	0.851	1.100	0.840	1.030
0.835	1.110	0.856	0.590	0.824	0.570
0.854	0.660				

Tapered Nozzle (WRDC)
Propane/Argon

Condition A		Condition B		Condition C	
Mass fraction	Lift-off velocity (m/s)	Mass fraction	Lift-off velocity (m/s)	Mass fraction	Lift-off velocity (m/s)
1.000	21.610	1.000	20.840	1.000	13.350
0.882	18.470	0.907	17.930	0.931	12.820
0.805	15.020	0.832	14.480	0.791	10.460
0.666	12.570	0.734	11.330	0.621	7.970
0.530	9.430	0.567	8.800	0.582	7.250
0.504	8.430	0.528	8.020	0.467	5.180
0.409	5.950	0.424	5.720	0.401	4.380
0.377	4.670	0.396	4.440	0.348	3.530
0.333	3.700	0.334	3.680	0.290	2.820
0.279	2.930	0.290	2.820	0.264	1.910
0.255	1.980	0.264	1.910	0.210	1.200
0.210	1.200	0.208	1.220		

Tapered Nozzle (WRDC)
Propane/Nitrogen

Condition A		Condition B		Condition C	
Mass fraction	Lift-off velocity (m/s)	Mass fraction	Lift-off velocity (m/s)	Mass fraction	Lift-off velocity (m/s)
1.000	21.610	1.000	20.840	1.000	13.350
0.942	17.680	0.944	17.600	0.866	10.060
0.861	14.860	0.903	13.860	0.736	7.470
0.775	11.800	0.818	10.920	0.703	6.740
0.680	8.310	0.710	7.840	0.599	4.710
0.668	7.210	0.683	7.010	0.541	3.870
0.575	4.960	0.591	4.790	0.485	3.080
0.510	4.160	0.528	3.980	0.432	2.340
0.472	3.190	0.477	3.150	0.411	1.530
0.397	2.580	0.414	2.460	0.365	0.880
0.411	1.530	0.404	1.560		
0.354	0.910	0.354	0.910		

**Tapered Nozzle (WRDC)
Propane/Helium**

Condition A		Condition B		Condition C	
Mass fraction	Lift-off velocity (m/s)	Mass fraction	Lift-off velocity (m/s)	Mass fraction	Lift-off velocity (m/s)
1.000	21.610	1.000	20.840	1.000	13.350
0.995	16.970	0.996	16.820	0.988	9.150
0.988	13.430	0.991	12.990	0.975	6.110
0.979	10.030	0.984	9.560	0.971	5.390
0.964	6.740	0.972	6.280	0.957	3.430
0.963	5.750	0.967	5.590	0.947	2.670
0.947	3.720	0.954	3.510	0.934	2.050
0.941	2.790	0.941	2.790	0.922	1.470
0.928	2.130	0.928	2.130	0.906	1.000
0.918	1.510	0.926	1.430	0.876	0.600
0.904	1.050	0.905	1.010		
0.879	0.610	0.869	0.620		

**Tapered Nozzle (UI)
Methane**

Lift-off velocities as a function of annular velocity

<u>Propane</u>		<u>Methane</u>	
Annulus velocity (m/s)	Fuel jet velocity (m/s)	Annulus velocity (m/s)	Fuel jet velocity (m/s)
0.000	14.820	0.000	20.770
0.037	17.140	0.021	21.020
0.075	19.070	0.026	22.790
0.113	17.830	0.031	23.560
0.150	17.140	0.039	24.590
0.225	14.340	0.049	29.410
0.300	12.940	0.073	30.820
		0.075	30.250
		0.113	28.040
		0.150	24.860
		0.225	21.020
		0.318	19.050